

Dublin City University

School of Physical Sciences

Characterisation and In-Situ Monitoring of Plasma Behaviour for Optimising Film Growth in Plasma-Enhanced Atomic Layer Deposition

Darragh O'Neill B.Sc.

Thesis submitted for the award of Doctor of Philosophy

December 2025

Supervised by Professor Deborah O'Connell, Professor Timo Gans &

Dr. Robert O'Connor

Declaration

I hereby certify that this material, which I now submit for assessment on the programme of study leading to the award of Ph.D. is entirely my own work, and that I have exercised reasonable care to ensure that the work is original and have conformed to the regulations on the use and declaration of Generative AI, and does not to the best of my knowledge breach any law of copyright, and has not been taken from the work of others save and to the extent that such work has been cited and acknowledged within the text of my work.

Signed: Darragh O'Neill (Darragh O'Neill, Candidate)

ID No.: 22260160

Date: 15/05/2026

Report of generative AI Tool Use (TOPIC)

Tools	ChatGPT, June - August 2025
Outputs	Structural suggestions to help improve overall thesis flow/organisation.
Prompts	While no recording of prompts were kept, they were generic and organisational in nature (examples below): • Suggest introduction sub-sections for work on plasma diagnostics in thin film processing. • What are common features to include in an experimental details section? • What are the benefits of splitting the discussion section from the experimental results? • What are the key points for a conclusion of a thesis?
Iterations	Iterations were limited to requesting alternative structural ideas/suggestions.
Critical Reflection	My usage of ChatGPT was minimal and only provided suggestions with structure in the writing process. This helped with the early stage writing process. However, modification to the structure was necessary, which I completed. Use of generative AI was performed before the regulations were implemented on September 1st, 2025.

Acknowledgements

Firstly, I would like to thank to my supervisors, Deborah O'Connell, Timo Gans, and Rob O'Connor, for their continuous support and encouragement over the years. Their expertise, guidance, and willingness to help (whether in navigating research challenges or fixing broken systems) have been invaluable. To Greg Hughes for sharing his passion and enthusiasm, and for the unforgettable Brookhaven trip. To Bert Ellingboe for his insightful advice and for the many constructive coffee chats.

To Pat Wogan, whose extensive knowledge of all thing's equipment-related has rescued me and the group from many difficult situations. To Joan Kelly for her support and for our regular meetings, which were always helpful and encouraging.

I want to thank everyone in the research group and in N117, whose company and support made the journey to and from DCU worthwhile every day.

Most importantly, I would like to thank my parents Pauline and William, my sister Aoife and my partner Emma for everything they have given me, and for their continued support, encouragement, and belief throughout my time at DCU.

I would like to acknowledge the Advanced Metallic Systems Centre for Doctoral Training (AMSCDT), I-Form, Science Foundation Ireland (SFI) and Intel for both their financial support and their wider contributions to my training and research development.

Table of Contents

Declaration i

Acknowledgements iii

Table of Figures vii

List of Abbreviations x

Contributing Publications xi

1 Introduction 1

1.1 Thin film technology 1

1.2 Atomic layer deposition 5

1.3 Low temperature plasmas 12

1.4 Motivation and Objectives 17

1.5 Thesis layout and Overview of results 19

1.6 References 23

2 Experimental Details 30

2.1 Overview 30

2.2 Instrumentation and Experimental Setup 32

2.3 Plasma Diagnostic Methods 35

2.3.1 Optical Emission Spectroscopy 35

2.2.2 Ion Flux Probe 46

2.3 Thin Film Deposition and Characterisation 52

2.3.1 Deposition system configuration 52

2.3.2 X-ray Photoelectron Spectroscopy (XPS) 55

2.4 References 65

3 Plasma optimisation and in-situ film characterisation of Co PE-ALD 69

3.1 Introduction 69

3.2 Experimental Details 72

3.3 Results 73

3.3.1 Pre-ALD Plasma diagnostics 73
3.3.2 In-situ Plasma diagnostics during PE-ALD process 81
3.3.3 Film Characterisation 83
3.4 Discussion 98
3.4.1 Influence of controllable parameters on process plasma 98
3.4.2 Impact of the ALD environment on plasma behaviour 99
3.4.3 Influence of plasma parameters on film properties 101
3.4.3 Correlation of plasma features with film properties 103
3.5 Conclusion 106
3.6 References 108
4 Plasma Characterisation of Remote ICP H_2/Ar Sources for PE-ALD 112
4.1 Introduction 112
4.2 Experimental Details 116
4.3 Results 118
4.3.1 Plasma stability 118
4.3.2 Plasma features vs parameters 119
4.4 Discussion 128
4.4.1 Impact of controlled parameters on electronic properties of the discharge 128
4.4.2 Impact of controlled parameters on reactive species generation and transport 132
4.5 Conclusion 138
4.6 References 140
5 Plasma monitoring and characterisation and in-situ film characterisation of Cu PE-ALD 143
5.1 Introduction 143
5.2 Experimental Details 146
5.3 Results 148
5.3.1 Plasma response to parameter variation 148

5.3.2 Film Characterisation 155
5.4 Discussion 169
5.4.1 Impact of ALD environment on plasma behaviour 169
5.4.2 Influence of plasma parameters on film properties 171
5.4.3 Correlation of plasma features with film properties 174
5.5 Conclusion 176
5.6 References 177
6 Impact study of unstable processing plasma of ZrN PE-ALD process with in-situ monitoring 181
6.1 Introduction 181
6.2 Experimental Details 183
6.3 Results 185
6.3.1 Plasma Stability 185
6.3.2 Film Characterisation 189
6.4 Discussion 198
6.5 Conclusion 202
6.6 References 203
7 Conclusion and Future work 207
7.1 Conclusion 207
7.2 Future Work 211

Table of Figures

Figure 1.1 - Number of publications with 'thin film' in the title per year obtained via Scopus. 2
Figure 1.2 - Schematic representation of steps in a typical ALD cycle[20]. 5
Figure 1.3 - (a) TEM image of Al_2O_3 and SiO_2 stack displaying the precise thickness control available with PE-ALD. (b) Thickness (nm) per cycle of SiO_2 films grown via PE-ALD with O_2 plasma[21]. 7
Figure 1.4 - Cross-sectional scanning electron microscope (SEM) images of (a) 300nm thick Al_2O_3 films and (b) 160 nm TiN films deposited on Si wafers with trench structures[23]. 8
Figure 1.5 - (a) Reaction-limited, (b) diffusion-limited and (c) recombination-limited[24]. 9
Figure 2.1 - Schematic of the state-of-the-art ALD/XPS cluster tool[7]. 32
Table 2.1 - Spectrometer specifications. 38
Figure 2.3 - Schematic of ALD chamber with labelled features and OES viewport. 39
Figure 2.4 - Operating principle of ion flux probe with negative collection bias. 49
Figure 2.5 - Basic schematic of ion flux probe electronic circuit. 50
Figure 2.6 - ALD system layout[7]. 52
Figure 2.7 - Automatic match unit schematic diagram[7]. 55
Figure 2.8 - XPS operational schematic[33]. 57
Figure 2.9 - Ag 3d peak with and without monochromator[35]. 58
Figure 3.1 - NH emission intensity contour plot for feed-gas flow (sccm) vs chamber pressure (mTorr) for a) 100 W, b) 200 W and c) 300 W ICP power. 74
Figure 3.2 - NH:H production ratio vs mean electron energy, with no loss (black) and full loss (red) of NH_2 intermediate radical. 77
Figure 3.3 - NH:Hα ratio contour plot for feed-gas flow (sccm) vs chamber pressure (mTorr) for a) 100W, b) 200W and c) 300W ICP power. 78
Figure 3.4 - NH:N_2 emission intensity ratio for ICP power vs feed gas flow for 30mTorr, 60 mTorr and 90 mTorr chamber pressure. 79
Table 3.1 - Experimental PE-ALD process plasma parameters. 81
Figure 3.5 - Bar charts) for a) NH emission and b) NH:Hα ratio for pre-ALD (red) and ALD (blue) processes with experimental process number from Table 3.1. 82
Figure 3.6 - Mean XPS survey composition of initial PE-ALD reference process with standard deviation represented by error bars. 84
Table 3.2 - PE-ALD process XPS elemental composition (%) and film thickness (nm). 85
Figure 3.7 - Fitted a) O 1s and b) C 1s high resolution XPS peaks for the reference process. 87
Figure 3.8 - Fitted a) N 1s and b) Co $2p_{3/2}$ high resolution XPS peaks for the reference process. 88
Figure 3.9 - Fitted Co $2p_{3/2}$ peaks for a) Optimised NH process and b) reference process. 91

Figure 3.10 - Survey XPS of the reference process (left) and the max NH:Ha ratio process (right), with regions of interest highlighted, both processes had a plasma power of 100 W. 92
Figure 3.11 - Survey XPS of the Optimised NH process (left) and the high pressure process (right), with regions of interest highlighted. 94
Figure 3.12 - C 1s fitted peaks for a) Optimised NH process and b) high pressure process. 95
Figure 3.13 - Fitted high resolution Co $2p_{3/2}$ peaks for a) Optimised NH process and b) low flow process. 96
Figure 3.14 - Linear correlation between NH:Hα measurements and film properties ((a)Co 2p composition (%) and (b) film thickness (nm)) 105
Figure 4.1 - Mean CV for Ha and Ar $2p_1$ emission lines, with error bar representing the standard deviation, for each plasma parameter investigated. 119
Figure 4.2 - Local mean electron energy (eV) vs ICP power (W). 120
Figure 4.3 - Degree of H_2 dissociation (%) vs ICP power (W). 121
Figure 4.4 - Ion flux (mV) vs ICP power (W). 122
Figure 4.5 - (a) Local mean electron energy (eV) (black) & ion flux (mV) (red) for variations in chamber pressure (mTorr). 123
Figure 4.6 - (a) Degree of H_2 dissociation (rH) (black) & atomic hydrogen density (nH) (red) for variations in chamber pressure (mTorr). 124
Figure 4.7 - (a) Local mean electron energy (eV) (black) & degree of dissociation (red) and b) ion flux (mV) for variations in total feed-gas flow (sccm). 125
Figure 4.8 - (a) Local mean electron energy (eV) (black) & degree of dissociation (red) and b) ion flux (mV) for variations in H_2 feed-gas content (%). 126
Figure 4.9 – Electron energy distribution functions (EEDFs) of a Druyvesteyn (blue) distribution and Maxwellian (orange) distribution. 131
Figure 5.1 - Mean CV of Hα emission (red) and Ar $2p_1$ (blue) emission with error bars representing the standard deviation for process parameters during PE-ALD. 149
Figure 5.2 - Time resolved OES of low flow PE-ALD process for Hα (red) and Ar $2p_1$ (blue) emission peak. 150
Figure 5.3 - Time resolved OES of low pressure PE-ALD process for Hα (red) and Ar $2p_1$ (blue) emission peak. 151
Figure 5.4 - 2nd and 19th ALD cycle time resolved OES spectra for a) Hα (red) and b) Ar $2p_1$ (blue) emission. 152
Figure 5.5 - Mean electron energy (eV) as a function of a) ICP Power (W), b) chamber pressure (mTorr) and c) feed-gas flow (sccm) PE-ALD processes. 153
Figure 5.6 - Degree of H_2 dissociation (%) as a function of a) ICP Power (W), b) chamber pressure (mTorr) and c) feed-gas flow (sccm) PE-ALD processes. 154
Figure 5.7 - Fitted XPS spectra of the Si 2p a) O_2 and c) H_2 plasma pre-treatment and the O 1s b) O_2 and d) H_2 plasma pre-treatment with $2p_{3/2}$ orbitals represented by solid lines and $2p_{1/2}$ represented by dashed lines. 155
Table 5.1 - XPS determined film composition and thickness for each investigated 20-cycle PE-ALD process. 157
Figure 5.8 - Cu 2p XPS spectra fitted according to Torres-Ochoa et al[17]. 158
Figure 5.9 - Wagner plot of Cu XPS data for ALD processes and reference Cu^{0-2+} states gathered from Biesinger et al[19]. 159

Figure 5.10- Pressure variations (10 mTorr (blue), 40 mTorr (red) and 70 mTorr (green)) influence on C 1s XPS spectra, with high binding energy area highlighted. 161
Figure 5.11 - O 1s fit for a) Reference PE-ALD process and b) H_2 plasma pre-treatment. 162
Figure 5.12 - a) Film thickness (Å) with estimated error from EAL calculation[13] and b) Cu 2p (%) per Å (black) and Cu 2p:C 1s ratio (red) vs ICP power (W). 163
Figure 5.13 - a) Film thickness (Å) with estimated error from EAL calculation[13] and b) Cu 2p (%) per Å (black) and Cu 2p:C 1s ratio (red) vs Pressure (mTorr). 165
Figure 5.14 - a) Film thickness (Å) with estimated error from EAL calculation[13] and b) Cu 2p (%) per Å (black) and Cu 2p:C 1s ratio (red) vs Flow (sccm). 166
Figure 5.15 - Fitted Si 2p XPS spectra of the 20 sccm PE-ALD process. 167
Figure 6.1 - Mean CV of Hα emission (red) and Ar $2p_1$ (blue) emission with error bars representing the standard deviation for process parameters and reference process during PE-ALD. 186
Figure 6.2 - Time resolved OES of a) Ref 1, b) Ref 2 and c) Ref 3 Hα and Ar $2p_1$ emission peaks. 187
Figure 6.3 - CV of Hα (left) and Ar $2p_1$ (right) emission peaks for variations in the power (blue) and pressure (green) process parameters. Low, medium and high are representing the parameter values of 100 W, 200 W and 300 W, respectively, for power and 10 mTorr, 30 mTorr and 60 mTorr, respectively, for pressure. 188
Table 6.1 - XPS survey elemental composition for repeated reference processes (1-3). 189
Figure 6.4 - Fitted O 1s (left), N 1s (middle) and Zr 3d (right) XPS spectra of a) Ref 1, b) Ref 2 and c) Ref 3 PE-ALD films. 190
Figure 6.5 - Bar chart of a) Si 2p (%), b) Zr 3d (%), c) Zr 3d:C 1s ratio and d) Zr 3d:N 1s ratio for power variation processes. 192
Figure 6.6 - Fitted O 1s (left), N 1s (middle) and Zr 3d (right) XPS spectra of a) 100 W, b) 200W and c) 300 W PE-ALD films. 193
Figure 6.7 - Bar chart of a) Si 2p (%), b) Zr 3d (%), c) Zr 3d:C 1s ratio and d) Zr 3d:N 1s ratio for pressure variation processes. 194
Figure 6.8 - Fitted O 1s (left), N 1s (middle) and Zr 3d (right) XPS spectra of a) 10 mTorr, b) 30 mTorr and c) 60 mTorr PE-ALD films. 196

List of Abbreviations

ALD	: Atomic Layer Deposition
AMU	: Automated Matching Unit
AR	: Aspect Ratio
BE	: Binding Energy
BEOL	: Back End of Line
CAE	: Constant Analyser Energy
CCD	: Charge Coupled Device
CCP	: Capacitively Coupled Plasma
CMOS	: Complementary Metal Oxide Semiconductor
CRR	: Constant Retardation Ratio
CVD	: Chemical Vapour Deposition
CV	: Coefficient of Variation
EAL	: Effective Attenuation Length
EEDF	: Electron Energy Distribution Function
ERA	: Energy Resolved Actinometry
FinFET	: Fin-type Field-Effect Transistor
FWHM	: Full Width Half Max
GAA	: Gate-All-Around
GPC	: Growth Per Cycle
HIPIMS	: High Power Impulse Magnetron Sputtering
ICP	: Inductively Coupled Plasma
IMFP	: Inelastic Mean Free Path
IPA	: Isopropanol
KE	: Kinetic Energy
LTPs	: Low Temperature Plasma
MFC	: Mass Flow Controller
MFP	: Mean Free Path
NIST	: National Institute of Standard and Technology
OES	: Optical Emission Spectroscopy
PE-ALD	: Plasma-Enhanced Atomic Layer Deposition
PLC	: Programmable Logic Controller
PVD	: Physical Vapour Deposition
RGA	: Residual Gas Analyser
RF	: Radio Frequency
RMSE	: Root Mean Squared Error
RSF	: Relative Sensitivity Factor
SCCM	: Standard Cubic Centimetre per Minute
SEM	: Scanning Electron Microscope
TEM	: Transition Electron Microscopy
UHV	: Ultra High Vacuum
VDF	: Vibrational Distribution Function
XPS	: X-Ray Photoelectron Spectroscopy

Contributing Publications

1. **Band Gap Engineering in TiO_x and TiO_x–Ni Thin Films by Plasma-Enhanced Atomic Layer Deposition: Structural and Optical Insights**
   J.A. Hernandez-Marquez, D. O'Neill, M. Snelgrove, A.I. Gonzalez-Jacquez, O. Solis-Canto, P. Tanabat, R. O'Connor, J.R. Farias-Mancilla, J.T. Elizalde-Galindo, P.G. Mani-Gonzalez, *MRS Commun.*, Accepted, Dec 2025.

2. **Deposition of High-Quality, Nanoscale SiO_2 Films and 3D Structures**
   P. Cannon, E. McGlynn, D. O'Neill, C. Darcy, E. Rouse, R. O'Connor, B. Freeland, B. O'Connell, J. Gaughran, *Appl. Mater. Today*, 2024, 38, 102175.

3. **Structure and Strain of CdS Nanofilms on Au (111) During Electrochemical Atomic Layer Deposition Growth**
   M. Snelgrove, A. Morris, D. O'Neill, F. Carlà, *Appl. Surf. Sci.*, 2024, 649, 159112.

4. **Deposition of Ultra-Thin SiO_2 Layers to Enable Core–Shell Nanostructure Architectures for Biosensing Applications (Conference Paper)**
   P. Cannon, E. McGlynn, D. O'Neill, B. O'Connell, B. Freeland, J. Gaughran, *IEEE NMDC*, 2023, 508–509.

5. **A Comprehensive Characterization of the Effect of Spatter Powder on IN939 Parts Fabricated by Laser Powder Bed Fusion**
   M.N. Doğu, A. Mussatto, M.A. Yalçın, S. Ozer, K. Davut, M.A. Obeidi, A. Kumar, S. Hudson, D. O'Neill, R. O'Connor, *Mater. Des.*, 2023, 235, 112406.

6. **Effect of Heat Treatment Time and Temperature on the Microstructure and Shape Memory Properties of Nitinol Wires**
   N. Agarwal, J.R. Murphy, T.S. Hashemi, T. Mossop, D. O'Neill, J. Power, A. Shayegh, D. Brabazon, *Materials*, 2023, 16, 6480.

7. **Plasma-Enhanced Atomic Layer Deposition of Nickel and Nickel Oxide on Silicon for Photoelectrochemical Applications**
   S. O'Donnell, D. O'Neill, K. Shiel, M. Snelgrove, F. Jose, C. McFeely, R. O'Connor, *J. Phys. D: Appl. Phys.*, 2023, 56, 415302.

8. **Growth Chemistry of Cobalt Nitride by Plasma Enhanced Atomic Layer Deposition**
   S. O'Donnell, M. Snelgrove, K. Shiel, C. Weiland, G. Hughes, J. Woicik, D. O'Neill, F. Jose, C. McFeely, R. O'Connor, *Mater. Res. Express*, 2022, 9, 106402.

Characterisation and In-Situ Monitoring of Plasma Behaviour for Optimising Film Growth in Plasma-Enhanced Atomic Layer Deposition

Darragh O'Neill

Abstract

Plasma-enhanced atomic layer deposition (PE-ALD) is a critical ultra-thin film deposition technique that enables precise control over thickness, composition and conformality. However, the behaviour of the plasma is highly sensitive to operating conditions. Changes in power, pressure, feed-gas composition or gas flow can significantly alter the properties of the discharge. As a result, plasma behaviour directly influences growth mechanisms and film properties, yet it is often treated as a fixed process parameter rather than a dynamic physical system, limiting optimisation, reproducibility and fundamental understanding.

This thesis investigates how plasma behaviour evolves both within and outside the ALD environment and demonstrates how plasma characterisation and in-situ diagnostics can improve the understanding, control and optimisation of PE-ALD. A combination of diagnostic methods are employed to study the plasma response and quantify key features.

Three metal and nitride PE-ALD systems (CoN, Cu and ZrN) are used to examine the influence of different precursors, plasma chemistries and reaction mechanisms on film growth. Plasma trends identified during pre-deposition characterisation guided the selection optimised process conditions and correlated with improved CoN growth behaviour. A quantitative study of H_2/Ar plasma established a baseline for interpreting plasma response, which was then applied during Cu PE-ALD to reveal how the ALD environment modifies plasma behaviour. This provided a deeper understanding of the plasma physics governing film properties. Finally, in-situ monitoring during ZrN PE-ALD exposed plasma instabilities that were not apparent in system logs but resulted in significant variations in film thickness, composition and bonding, leading to poor reproducibility across processes under identical parameter conditions.

Overall, this work demonstrates that plasma behaviour strongly influences PE-ALD outcomes and that combining pre-deposition characterisation, in-situ diagnostics and parameter optimisation provides a powerful framework for understanding, improving and stabilising PE-ALD processes, with the potential to enable closed-loop feedback control.

1 Introduction

1.1 Thin film technology

Thin films are widely used in a range of modern technologies including medical[1], aerospace[2], energy systems[3,4] and semiconductor manufacturing[5]. Their use comes from the ability to tailor material properties at the nanoscale which enables functionality that can differ substantially from bulk material[6]. As device dimensions continue to shrink along with new complex geometry designs which improve device performance and efficiency in many manufacturing fields[7], additional requirements are introduced for thin film deposition methods. Key performance criteria such as film uniformity, conformality, composition and defect density are increasingly important and determine the success or failure of deposition methods in advanced manufacturing.

In the semiconductor industry, thin films provide the foundation of interconnect materials, dielectric layers, diffusion barriers and other critical features[5,8]. To manufacture these complex circuits, multiple individual process steps are undertaken including patterning, etch and deposition. Transitions from planar to three-dimensional architecture such as fin-type field-effect transistors (FinFETs), gate-all-around (GAA) structures and other high-aspect ratio features further drive the requirement for precise manufacturing steps[9]. Beyond microelectronics factors such as corrosion resistance[10], hardness layers[11], thermal stability[12] and biocompatible surface layers[13] all require extreme control of surface chemistry and structure and their use cases span multiple industries. The demands of new technologies have driven significant research, as demonstrated by the number of publications with ‘thin film’ in the title, as seen in Figure 1.1.

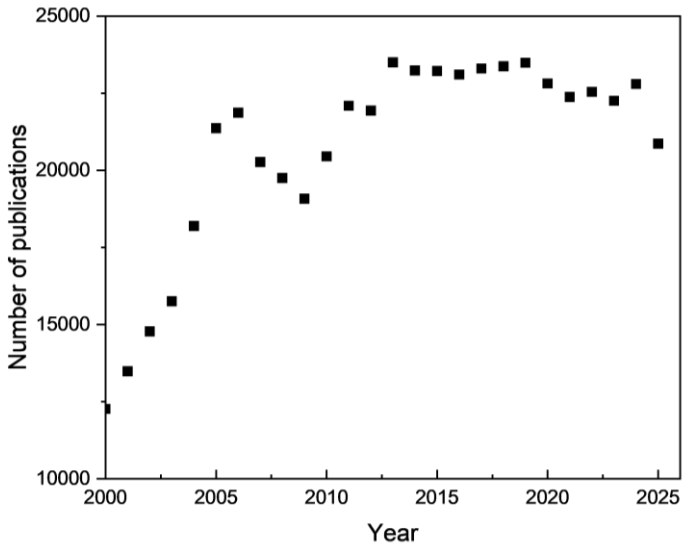


Figure 1.1 - Number of publications with 'thin film' in the title per year obtained via Scopus.

There is a wide range of deposition techniques available, each providing their own advantages and disadvantages. Physical vapour deposition (PVD) methods are some of the most widely used due to a high diversity of materials and composition control[14]. However, PVD methods can suffer from line-of-sight limitations, which can impact both step coverage in high-aspect ratio structures and film uniformity. Chemical vapour deposition (CVD) represents an alternative route that utilises gas-phase surface reactions for deposition. CVD can achieve uniform and conformal films over both large surface areas and complex structures, making it applicable for semiconductor manufacturing[15]. However, limitations in thickness control and high processing temperatures can restrict the use of this technique. Some cost-effective alternatives, including spin coating and inkjet printing, provide effective solutions for certain applications, but achieving uniform nanoscale films with strict control over composition and chemical structure can be challenging.

As device size decreases and structural complexity increases, the limitations of conventional PVD and CVD have become highlighted, particularly for applications that

require atomic-scale control, high-aspect-ratio conformality, and low-temperature processing. Atomic layer deposition (ALD) provides an ultra-thin, highly uniform, and conformal film with nanoscale thickness control, making it a potential solution to many of these challenges[16]. ALD's ability to produce a variety of film compositions makes it a desirable method in modern thin-film research and manufacturing.

Thermal ALD utilises elevated substrate temperatures to drive surface reactions, which has resulted in difficulties producing certain materials due to insufficient reactivity, often requiring significantly higher temperatures as a solution. Metals and metal nitrides are particularly affected by this issue[17]. Plasma-enhanced ALD (PE-ALD) addresses this by enhancing the thermally driven processes with the increased energy of plasma-generated species. The additional energy enables reaction pathways at lower deposition temperatures. While PE-ALD provides benefits, the introduction of the plasma significantly increases process complexity. This requires an understanding of plasma behaviour, its response to variations in processing parameters, and its influence over film properties. Previous studies in high power impulse magnetron sputtering (HIPIMS) have demonstrated extensive plasma diagnostics can provide detailed process understanding that enables identification of optimal operating conditions[18]. Additionally, real-time plasma diagnostics combined with physic-based modelling has been demonstrated as a non-invasive approach enabling real-time predictive control of PVD processes[19]. A similar approach can be applied to plasma-enhanced ALD (PE-ALD), where time-resolved plasma diagnostics combined with physics-based or data-driven models would enable process optimisation and predictive control.

In summary, thin film technology is foundational to a broad range of scientific and industrial applications. The demands on thin film deposition techniques continue to increase as stricter requirement are placed on the resulting films. ALD, specifically PE-

ALD, offers critical features that can meet these requirements through atomic-scale thickness control, excellent conformality, uniformity, and composition control. The following sections provide key background information on the fundamental principles of ALD and low temperature plasma.

1.2 Atomic layer deposition

Atomic layer deposition is a derivative of chemical vapour deposition which provides ultra-thin films for a wide range of applications. CVD utilises a consistent stream of reactive gases, called precursors, to continually deposit the desired material on exposed surfaces. ALD split the CVD reaction mechanism into two 'half-cycle' reaction processes to deposit the desired material. Each ALD 'half-cycle' exposes the substrate surface to a reactive medium in which self-limiting growth occurs. One ALD cycle consists of two 'half-cycle' reaction processes separated by purge steps performed sequentially, in which the desired material is grown in a self-limited process. It's this growth mechanism which allows ALD to provide its enhanced film thickness control along with its excellent conformality and uniformity. These properties of ALD have made the technique highly desirable in a large range of applications, particularly in the microelectronics industry and for surface coatings.

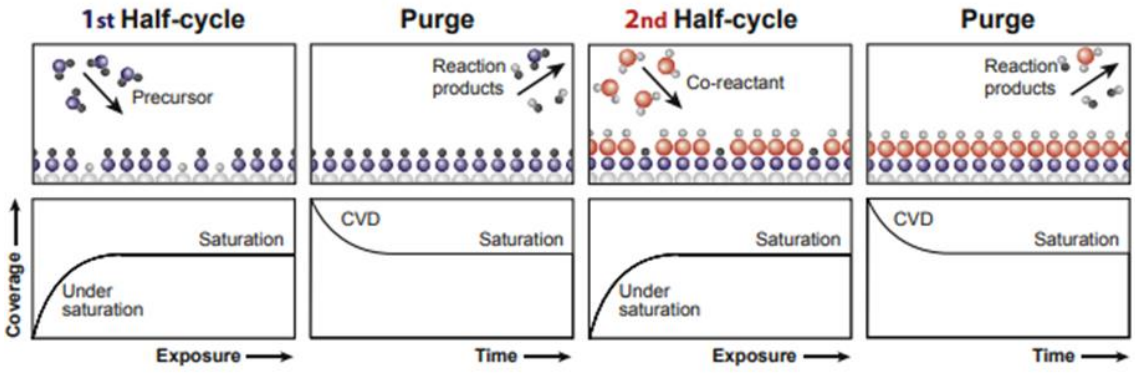


Figure 1.2 - Schematic representation of steps in a typical ALD cycle[20].

A typical ALD process, as seen in Figure 1.2, follows two half-cycle reactions as mentioned above. The first step exposes the substrate to a precursor which reacts with all

available active surface sites on the substrate in a self-limiting process. The formation of the film starts in this step. After saturation, all remaining precursor and reaction by-products are purged from the system. The second step exposes the substrate to a co-reactant. In this step the required ALD film is produced, and the surface is functionalised with active sites for further ALD cycles. After exposure to the co-reactant has occurred all remaining co-reactant and by-products are purged from the system.

In each step, the reactions are self-limiting - resulting from limited active surface sites - leading to a defined amount of material added to the substrate. Over a full ALD cycle, the thickness of material added is known as the growth per cycle (GPC). The self-limiting surface reactions are a key feature of ALD that separates it from other methods, ensuring its control over the film. In the first step the precursors chemisorb to all active surface sites, which are typically functional groups but can also be defects or dangling bonds. Once an entire monolayer of chemisorbed material has been achieved it acts as a passivation layer preventing further reactions. This process is then repeated with the co-reactant, and the desired layer is deposited. The surface reactions are typically driven thermally or by the elevated energy of plasma generated species. Insufficient exposure to the reactive medium leads to under-saturation, while inadequate purging can result in CVD-like deposition due to the simultaneous presence of precursor and co-reactant species within the chamber, as shown in Figure 1.2.

Key features which make ALD such a powerful and desirable technique are its precise thickness control, uniformity and conformality. Dingemans et al.[21] demonstrated the ability for precise control by stacking alternative layers of Al_2O_3 and SiO_2 grown by PE-ALD. The SiO_2 growth per cycle was measured by in-situ ellipsometry and compared with post deposition transmission electron microscopy (TEM) measurements.

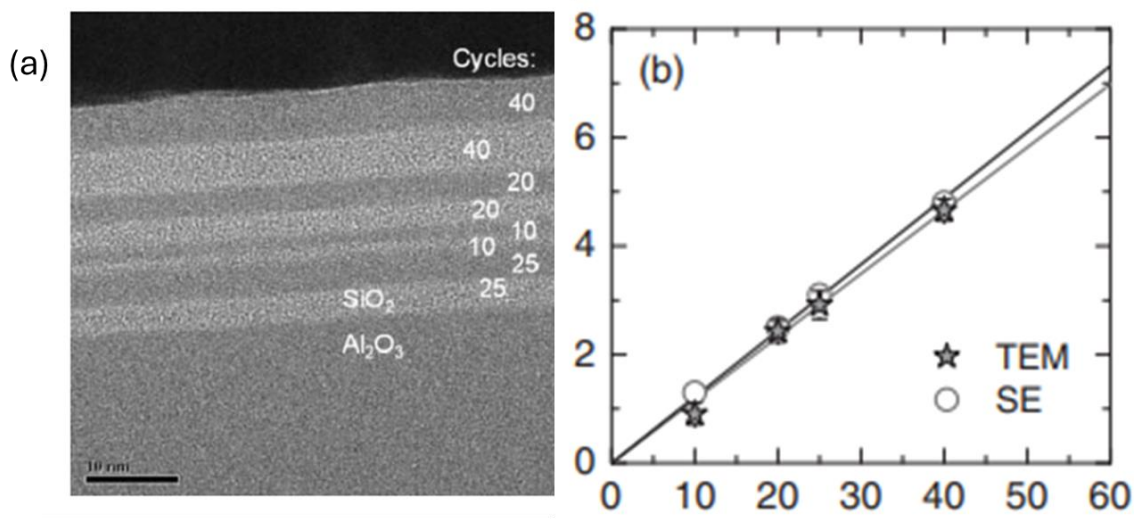


Figure 1.3 - (a) TEM image of Al_2O_3 and SiO_2 stack displaying the precise thickness control available with PE-ALD. (b) Thickness (nm) per cycle of SiO_2 films grown via PE-ALD with O_2 plasma[21].

Excellent agreement between the thickness values measured by both techniques confirmed the reliability of the GPC along with the precision in film thickness of the ALD process overall. A further investigation into the conformality of the process was also undertaken. SiO_2 was deposited on trench structures with an aspect ratio of 30. High conformatlity (~95%) was achieved, highlighting ALD's ability to control key film properties.

A study on growth uniformity was conducted by Fryauf et al[22] in which an aluminium oxide was successfully grown over a 0.9 m diameter substrate in a novel meter scale ALD system. Initial tests produced variations of approxiamtely 2.5 %. Optimised proceess achieved improve variations of only 1 % over the 0.9 m diameter. This result displays ALD's ability to achieve large area uniform coatings which is a desirable functions for certain industrial applications.

Perfect conformality of Al_2O_3 was achieved by Ritala et al[23] using thermal ALD. 160 nm TiN and 300 nm Al_2O_3 films were deposited on trench structures, see Figure 1.4 below. Less than a 0.7 % variation in film thickness was identified for the Al_2O_3 films emphasizing the process' precise nature.

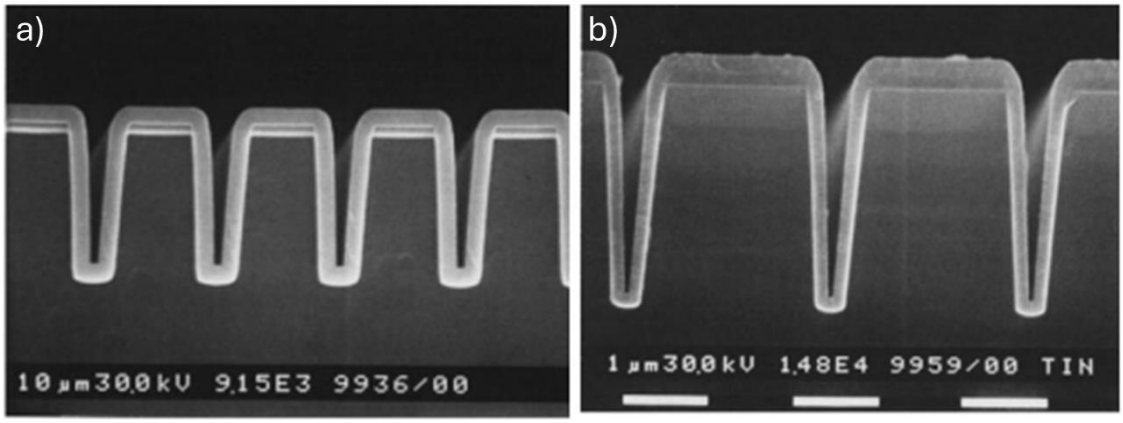


Figure 1.4 - Cross-sectional scanning electron microscope (SEM) images of (a) 300nm thick Al_2O_3 films and (b) 160 nm TiN films deposited on Si wafers with trench structures[23].

However, increased material deposition occurred on the flat top of the trench structure in the TiN depostion process. Limitations in conformality can occur on high-aspect ratios for ALD processes depending on the growth regime. Knoops et al[24] demonstrated different growth regime limitations along with discussion on the reasoning for the limitations. These are labelled reaction-limited, diffusion-limited and recombination-limited and their impact on film growth can be seen in Figure 1.5.

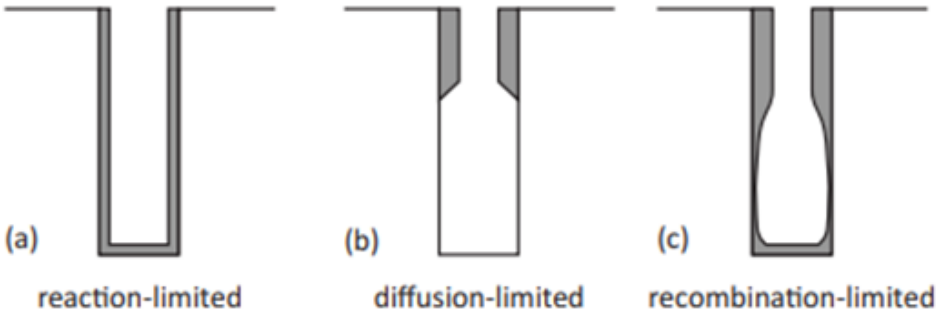


Figure 1.5 - (a) Reaction-limited, (b) diffusion-limited and (c) recombination-limited[24].

Reaction-limited regime is a result of growth until saturation, and is identified as a successful ALD process. Diffusion-limited occurs when growth slows due to insufficient diffusion of either the precursor or reactive species into high-aspect ratio (AR) features. Recombination-limited is identifed when a reduced growth rate occurs in high-AR features and required increased processing time until saturation.

Recombination-limited behaviour can occur due to recombination reactions between reactive plasma radicals, which reduces the number of species available to diffuse deeper into the feature. For example, oxygen radicals generated in the plasma may recombine according to $O + O \rightarrow O_2$, either in the gas phase or at the surface. This recombination reduces the concentration of reactive species available for surface reactions and therefore limits the penetration of the plasma species into high-AR structures.

Arts et al.[25,26] successfully deposited oxide films on high-AR structures (>800). It was shown that in the PE-ALD processes the reaction was recombination-limited. Increased plasma expousre time was required for complete staturation. The recombination probability of the plasma species directly relates to the peneration of the film into high-AR strctures. Low values, of the order of 10^{-5}, which was determined for TiO_2 and SiO_2, resulted in extremely deep penetration (AR > 800). A much shallower penetration of 40-

80 AR was achieved by recombintation probabilities in the range 10^{-3} - 10^{-1}. Overall, ALD has been shown to produce precise thin films with high uniformity over large surface areas and high conformality over complex high-AR structures.

Plasma-enhanced atomic layer deposition utilises the elevated energies of generated plasma species as the driving mechanism during the ALD co-reactant step. The increased energy allows for reactions with the chemisorbed precursor material. PE-ALD has demonstrated improved material properties such as film densification, improved ligand removal, reduced processing temperatures and both increased GPC and choice of precursors[27–32] when compared to thermal ALD.

Van Bui et al.[33] deposited AlN films via thermal and PE-ALD. In-situ ellipsometry was used to determine there was no initial nucleation delay with the PE-ALD process compared to a delay found with the thermal process. X-ray diffraction showed an increase in film crystallinity associated with the PE-ALD films which was concluded to be as a result of the increased energy provide by the plasma. Park et al.[34] observed improved TaN crystallinity with longer plasma exposure. Film density also increased from 3.6 gcm^{-3} to 7.9 gcm^{-3} from TaN films produced using thermal and PE-ALD, respectively. The proposed reason for the density increase was the impingement of hydrogen ions onto the surface supplying sufficient energy for atomic rearrangement of the TaN film.

Jiang et al.[35] investigated GaN produced PE-ALD films. The GaN films were found to have significant oxygen contamination. Increasing plasma power resulted in the production of more hydrogen radicals from the NH_3 plasma which interacted with the surface GaO to form GaH_3. This provided a secondardy reaction pathway for the formation of $Ga(NH_2)$ through the replacement of of H with NH species resulting in the growth of GaN. Zeng et al[36] grew AlN using A-B-C ALD process. This is a modification

of the traditional ALD two step process (A-B) to include an additional step at the end (C), consisting of A) TMA dose, B) H_2+N_2 plasma and C) Ar plasma. The addition of the Ar plasma step per cycle was suggestd to crack the TMA and elimate contaminants, resulting in high purity, crystalline films.

Vos et al[37] investigated different plasma feed-gas compositions for PE-ALD processing of $CoCp_2$ for cobalt nitride films. Results found that NH species were necessary for eliminating precursor ligands and improving film purity. The composition strongly affects the films incorporation of precursor ligands suggesting optimisation of PE-ALD processes depends on the plasma behaviour.

The increased energy available as a result of the reactive plasma species can also negatively impact the film. Zhao et al[31] observed film damage in In_2O_3 films as a result of ion bombardment after saturation occurred leading to degradation in the film. The ion induced damage was found to have little impact on the film before saturation. Reduction in ion induced film damage can be achieved through the use of a remote plasma source. Kim et al[38] investigated the substrate damage in both direct and remote ALD plasma set ups. The direct plasma had increased growth rate and polycrystalline structure but suffered induced plasma damage. The remote plasma minised substrate damage but also produced a completely amorphous structure, demonstrating the importance of ion impingment on the surface to reorder film structure.

Introducing reactive plasma species in ALD processing provides significant benefits but also directly links film properties to the plasma behaviour. Sensitivties in the plasma response can influence film properties. As such it is important to understand low temprature plasma used in PE-ALD processing.

1.3 Low temperature plasmas

Low temperature plasmas (LTPs) are partially ionised gases in which a strong thermal non-equilibrium exists between the electrons and the heavier species present[39]. In typical processing conditions the electrons have temperatures of several electron volts, where 1 eV corresponds to approximately 11600 K[40]. The neutral gas remains close to room temperature or is only heated to a few hundred Kelvin[41]. This thermal difference enables LTPs to generate a range of highly reactive species, as the elevated electron energies drive dissociation, excitation and ionisation processes[39,42]. The resulting chemically active environment provides a powerful means of initiating and sustaining surface reactions while maintaining low overall temperature. These characteristics have made low temperature plasmas desirable in multiple fields, including surface modification, microelectronics, biomedical and thin-film deposition techniques such as plasma-enhanced atomic layer deposition (PE-ALD)[43–45].

Plasmas used in PE-ALD are typically generated using 13.56 MHz radio frequency (RF) power in either capacitively coupled (CCP) or inductively coupled (ICP) configurations[46,47]. In CCP systems the discharge is sustained by the oscillating electric field established between two electrodes, which commonly results in relatively high sheath voltages and can lead to increased ion bombardment at the substrate surface[47,48]. A plasma sheath is a non-neutral boundary region that forms at the interface between a plasma and a material surface. Due to the significantly higher mobility of electrons compared to ions, electrons are lost to the surface more rapidly, resulting in the surface acquiring a negative potential relative to the quasi-neutral bulk plasma. This potential difference establishes an electric field across the sheath region. The potential drop that develops between the plasma bulk and the surface is defined as the sheath voltage. Ions entering the sheath are accelerated by this electric field towards the surface, and their

impact energy is largely determined by the magnitude of the sheath voltage. Consequently, higher sheath voltages result in increased ion bombardment energies at the substrate surface, which may promote surface activation and film densification, but can also induce damage in sensitive materials. ICP sources utilise an inductive coil to couple power into the gas, producing high-density plasmas with significantly lower sheath voltages[42]. This reduces ion energies while maintaining a high flux of reactive species. Many ALD systems employ remote plasma sources, where the plasma is generated upstream and reactive species are transported to the substrate through diffusion. During transport, energetic ions and electrons recombine or are quenched, reducing plasma induced damage while still providing chemically active species for surface reactions[40,42]. The choice of plasma configuration has an important influence on the resulting film properties, as differences in energy and species distribution directly affect processes such as film densification, crystallinity and overall processing.

Low temperature plasmas contain a mixture of electrons, ions and radicals which contribute differently to the overall plasma chemistry. Electrons play the primary role in sustaining the discharge and contribute to species generation through electron-impact processes such as ionisation, dissociation and excitation[39,42]. The production of these species is dependent on the gas composition and the electron-driven reactions. In PE-ALD, radicals often serve as the dominant species responsible for driving the desired chemical reaction mechanisms at the surface. Ions and electrons can also deliver additional energy to the growing film, which may promote densification or modify the developing crystal structure, but can equally lead to film damage if ion energies are excessive[31,38].

Control of the plasma during PE-ALD processing is essential, as its behaviour directly influences the resulting film properties. Previous work has demonstrated that increasing

power results in higher electron densities in low pressure ICP sources which reduces the mean electron energy[49,50]. ICP sources can undergo mode transitions from E-mode (CCP mode) to H-mode (ICP mode). In E-mode operation, the plasma is sustained primarily by capacitive coupling between the coil and the plasma, resulting in relatively low electron densities. As power increases the discharge transitions to H-mode, where power is coupled inductively through the oscillating magnetic field generated by the coil. This mode is characterised by a significant increase in electron density and more efficient plasma generation, as discussed by Abdel-Rahman[51]. The increased electron density provides additional species which improves overall dissociation rates[51]. Iordanova et al[52] demonstrated increasing pressure in the range of 7.5 mTorr to 45 mTorr resulted in a linear increase in dissociation in a H_2/Ar ICP discharge due to the increased H_2 density. Other work discussed the decrease in electron temperature with increasing pressure a direct result of increased collisions and lower mean free path[53]. Similar reductions were also observed in ion flux rate which was assigned to recombination collisions with increased pressure[54]. The influence of feed-gas flow has previously been shown to be composition dependent. Doh et al demonstrated that ion flux rate for atomic plasmas increased with higher flow while they decreased for molecular gas compositions[55]. Other work with low pressure ICP discharges concluded that increased flow reduces residence time within the source an can lower overall dissociation rates[56]. As previously mentioned, feed-gas composition influences the plasmas ion flux rates. However, additional work has demonstrated increased H_2 content in a H_2/Ar ICP discharge reduces the mean electron energy[57]. Smith et al.[58] demonstrated that in a H_2 plasma, spatial variations in gas temperature modify the vibrational distribution function (VDF). Such changes, through electron-vibration coupling, can indirectly influence electron energy within the discharge. Variations in input power, chamber pressure, feed-gas flow rate and gas

composition can significantly alter the plasma behaviour. Due to the critical nature of the plasma behaviour in PE-ALD processing, their influence must be understood.

However, beyond the response of the plasma to controlled input parameters there are additional factors which must be considered. Changes in the local environment due to reaction by-products during PE-ALD processing can also influence the plasmas response[59,60]. These additional species can result in collisional interactions with plasma species producing undesired effects. Due to the nature of ALD, deposition on reactor walls and even the ICP source can unintentionally occur, despite mitigation procedures. Such instances can modify power coupling and surface recombination rates changing the plasma behaviour, which can lead to gradual drifts in plasma behaviour reducing process reproducibility and effectiveness.

Due to the plasmas response being highly sensitive to processing parameters as discussed above along with potential chamber condition variations, plasma diagnostics play a crucial role in both understanding the immediate response of the plasma, and drifts over time. The use of invasive diagnostics is impractical in PE-ALD as such techniques can introduce contamination, modify chamber geometry, disturb gas flow and ultimately require extensive cleaning. For this reason, non-invasive diagnostic methods are essential for characterising the plasma during PE-ALD.

Several non-invasive approaches are currently employed, including impedance monitoring, residual gas analysis (RGA) and optical emission spectroscopy (OES). Each of these methods has limitations. Impedance monitoring provides only indirect information. RGA offers detailed gas-phase composition data but typically lacks temporal resolution. OES is widely used due to its simplicity, but it captures only optically active species. Many commercial ALD tools already incorporate OES ports for

endpoint detection. However, extracting quantitative plasma parameters from OES often requires significant modelling, such as collisional–radiative models.

Despite these challenges, in-situ, non-invasive diagnostics remain essential for the progressive understanding and optimisation of PE-ALD. Real-time measurements could allow for the identification of instabilities or drift from optimal conditions. A clear understanding of the plasma behaviours is therefore essential for ensuring reproducibility, understanding growth mechanics and optimising PE-ALD processes.

1.4 Motivation and Objectives

Plasma-enhanced ALD relies on plasma generated reactive species to drive surface reactions. This enables growth for films that are typically difficult to reduce in thermal ALD, such as metals, along with improved film properties such as crystalline structure, increased growth rate and density. However, it also means that the outcome of a PE-ALD process depends directly on the behaviour of the plasma. Variations in power, feed-gas composition, feed-gas flow or chamber pressure can alter key plasma features such as the mean electron energy, the electron energy distribution function, dissociation rates and the transport of reactive species. These changes can strongly influence growth mechanisms and result in variations in thickness, composition and bonding. As a result, understanding how the plasma responds to its controllable parameters is essential for reliable PE-ALD processing.

Despite widespread application of plasma-enhanced ALD, most studies treat the plasma as a fixed process condition rather than a dynamic physical system. Plasma parameters such as electron energy, dissociation fraction, and ion flux are rarely measured during deposition, and the influence of ALD chemistry on plasma behaviour is typically assumed rather than quantified. Consequently, correlations between process parameters and film properties lack a physical basis, limiting predictability and reproducibility. This thesis addresses this gap by using quantitative diagnostics to directly relate plasma physics to PE-ALD growth behaviour.

Furthermore, a pre-ALD plasma study can give a controlled view of how the plasma responds to changes in operating conditions, but this behaviour does not always carry over into the ALD environment. Reaction by-products can alter excitation behaviour, quench species and modify the plasma in ways that are not reflected in pre-ALD

measurements. Because of this, in-situ plasma monitoring during deposition becomes important for identifying how the plasma behaves during processing and for detecting changes or instabilities that would not appear in system logs.

The motivation for this work is to develop a clearer understanding of the relationship between processing parameters, plasma behaviour and film properties.

This thesis investigates, both qualitatively and quantitatively, how the plasma responds to changes in operating conditions and how these changes influence film growth. The work combines pre-ALD characterisation with non-invasive plasma diagnostics and in-situ film characterisation to determine the relationships involved. An additional motivation is to demonstrate that instabilities in plasma behaviour can directly impact film quality and in-situ plasma diagnostics and monitoring can reveal failure mechanisms in the process which might not be identified without such monitoring.

1.5 Thesis layout and Overview of results

This thesis is structured to progressively develop an understanding of the plasma behaviour and demonstrate its influence during plasma-enhanced atomic layer deposition processes. The work begins with a study utilising basic optical emission spectroscopy measurements in a pre-ALD and PE-ALD process to identify relationships between process parameters, plasma features and film properties. Following this, a detailed pre-ALD parametric study is performed with more advanced plasma diagnostics which provide quantitative information. The insights from this study are then applied to a PE-ALD process, allowing for a more comprehensive insight to be gained on the relationships between controlled parameters, plasma behaviour and film properties. The final study performed in this thesis examines an experimental set in which plasma instability led to non-reproducible processing, highlighting the importance of stable plasma conditions and reinforcing the need for pre-ALD investigation for such a condition.

The materials examined in this work were selected to enable an investigation of PE-ALD processes across different plasma environments, precursor chemistries and reaction mechanisms, while focusing on metallic and semi-metallic films. CoN was selected as the initial case study as previous PE-ALD work demonstrated the production of both conductive mixed phase cobalt nitride and high impurity CoN, due to considerable precursor ligand incorporation. These results present an opportunity for the influence of NH_3 based plasma chemistry on the transition metal nitride to be explored[61–63]. Copper was then investigated as a metal which utilises hydrogen-based reduction in PE-ALD, allowing for a contrast in both plasma environment and reaction mechanisms[64]. Finally, ZrN was selected as a conductive metal nitride deposited using a mixed N_2/H_2 plasma, allowing for the investigation into the plasma behaviour and its influence on film

growth[65]. Together, these materials provide a range of plasma environments and precursor chemistries, allowing for a general investigation into the plasma influence and response. As highlighted by Jussila et al[66] and Hagen et al[67], oxide ALD is well established and therefore not considered here, while the less developed understanding of PE-ALD metal and nitride growth offers an opportunity to explore plasma mechanisms and help close this research gap.

Chapter 3 focuses on the influence of controllable parameters during the PE-ALD of cobalt nitride using Bis(cyclopentadienyl)cobalt(II) and NH_3 plasma. A pre-ALD plasma study was used to select operating conditions based on the behaviour of key NH and H emission lines measured using non-invasive OES measurements. These conditions were used during the deposition processes and in-situ OES revealed that the presence of the ALD environment modified the plasma response through the quenching of emission lines. However, the relative trends observed in the pre-ALD study were preserved. Film characterisation showed that plasma conditions strongly influenced film growth, composition and bonding. A process based on the optimised NH emission intensity during the pre-ALD study produced the highest cobalt incorporation and significantly improved film thickness when compared to a reference process. Additional processes were performed, and it was identified that high chamber pressure suppressed growth and high feed-gas flow produced the thickest film. OES measurements of the NH:Hα ratio was linked with growth mechanisms such as thickness and cobalt content. This chapter demonstrated that a pre-ALD parametric study can guide process optimisation. However, a lack of quantitative plasma diagnostics data limited the insight into the plasma behaviour.

Chapter 4 provides a detailed study on how operating parameters influence the behaviour of a low-pressure H_2/Ar ICP plasma by using a combination of both invasive, ion flux

probe, and non-invasive, OES and energy resolved actinometry (ERA), plasma diagnostics techniques. Plasma features such as mean electron energy, degree of H_2 dissociation and ion flux at the substrate level were analysed and provided an insight into the influence of ICP power, chamber pressure and both feed-gas flow and composition. Power was found the be the dominant factor influencing the degree of H_2 dissociation with feed-gas flow the second most influential parameter. Chamber pressure impacted species transport via changes in the mean free path. Gas composition played the largest role in determining the mean electron energy via changes in the electron energy distribution. These results formed a foundational plasma response understanding which was later used to investigate the influence of the ALD environment and assess if observed trends in the plasma response remain valid during deposition processes.

Chapter 5 builds directly on the finding from the previous plasma characterisation work. The H_2/Ar plasma is investigated during the PE-ALD of copper films using Bis(2,4-pentanedionato)copper and H_2/Ar plasma In-situ OES and ERA determined the influence of the ALD environment on the plasma behaviour. Results indicate that trends were preserved with the environmental change but there were absolute value differences. Film characterisation demonstrated that general parameter variations resulted in consistent film properties changes when compared with results from Chapter 3 and published work. Overlapping plasma features between different investigated process parameters resulted in no plasma feature correlations with film properties emerging. However, a limited dataset restricted modelling. The study demonstrated that quantitative plasma diagnostics provides a powerful way of comparing in-situ plasma conditions with pre-ALD reference behaviour to identify changes during processing along with gaining a deeper insight into the plasma physics.

Chapter 6 presents a case study in which plasma instability resulted in non-reproducible growth during ZrN PE-ALD. In this work the absence of a pre-ALD plasma study led to the selection of processing conditions that resulted in instabilities in a $H_2/N_2/Ar$ discharge during Tetrakis(dimethylamino)zirconium(IV) PE-ALD processing. In-situ OES revealed ignition spikes, slow recovery behaviour and general deviations from a consistent discharge. This resulted in significant variations in film thickness, composition and bonding across repeated reference processes. Parameter variations also deviated from previously established trends. This case study highlights the importance of both a pre-ALD study to identify an operating window along with in-situ monitoring to detect process faults.

The results presented in this thesis demonstrate that plasma behaviour is sensitive to processing conditions and can significantly influence film properties. A pre-ALD plasma study provides valuable information for process selection. Quantitative plasma diagnostics allows for deeper insights into important plasma behaviour through features such as mean electron energy and dissociation rates. Further information of the influence of the ALD environment can be obtained by comparing in-process measurements with pre-ALD characterisation. In-situ monitoring of the plasma can also identify significant variations in its response which can be used to identify and understand changes in film properties. The aim of this progression is to provide a coherent understanding of how PE-ALD processes depend on plasma physics and to demonstrate how targeted diagnostics can be utilised to both optimise processing along with improving its reproducibility.

1.6 References

(1) Rajan, S. T.; Subramanian, B.; Arockiarajan, A. A Comprehensive Review on Biocompatible Thin Films for Biomedical Application. *Ceram. Int.* **2022**, *48* (4), 4377–4400.

(2) Xie, G.; Bai, H.; Miao, G.; Feng, G.; Yang, J.; He, Y.; Li, X.; Li, Y. The Applications of Ultra-Thin Nanofilm for Aerospace Advanced Manufacturing Technology. *Nanomaterials* **2021**, *11* (12), 3282.

(3) Silva, J. P.; Sekhar, K. C.; Pan, H.; MacManus-Driscoll, J. L.; Pereira, M. Advances in Dielectric Thin Films for Energy Storage Applications, Revealing the Promise of Group IV Binary Oxides. *ACS Energy Lett.* **2021**, *6* (6), 2208–2217.

(4) Scarpulla, M. A.; McCandless, B.; Phillips, A. B.; Yan, Y.; Heben, M. J.; Wolden, C.; Xiong, G.; Metzger, W. K.; Mao, D.; Krasikov, D.; others. CdTe-Based Thin Film Photovoltaics: Recent Advances, Current Challenges and Future Prospects. *Sol. Energy Mater. Sol. Cells* **2023**, *255*, 112289.

(5) Yan, A.; Wang, C.; Yan, J.; Wang, Z.; Zhang, E.; Dong, Y.; Yan, Z.-Y.; Lu, T.; Cui, T.; Li, D.; others. Thin-Film Transistors for Integrated Circuits: Fundamentals and Recent Progress. *Adv. Funct. Mater.* **2024**, *34* (3), 2304409.

(6) Rao, M.; Shekhawat, M. A Brief Survey on Basic Properties of Thin Films for Device Application. In *International Journal of Modern Physics: Conference Series*; World Scientific, 2013; Vol. 22, pp 576–582.

(7) Chandel, M.; Rosenkranz, A.; Moraru, D.; Woźniak, A.; Jastrzębska, A. M. Measuring the Future–Nanometrology for Advanced Manufacturing of Miniaturized Devices. *Adv. Funct. Mater.* **2025**, *35* (45), 2501663.

(8) Kim, H.; Oh, S.; An, S.; Kim, J.; Kim, T.; Jeong, S.; Kaya, O.; Galvani, T.; Roche, S.; Cha, J. J.; Chhowalla, M.; Shin, H. S.; Shin, H.-J. Future Interconnect Materials for Highly Integrated Semiconductor Devices. *Nat. Rev. Electr. Eng.* **2025**. https://doi.org/10.1038/s44287-025-00233-y.

(9) Wang, M. A Review of Reliability in Gate-All-around Nanosheet Devices. *Micromachines* **2024**, *15* (2), 269.

(10) Shang, C.; Sang, D.; Li, C.; Zou, L.; Wu, J.; Wang, Q. 2D Materials for Marine Corrosion Protection: A Review. *APL Mater.* **2024**, *12* (6).

(11) Mayrhofer, P. H.; Clemens, H.; Fischer, F. D. Materials Science-Based Guidelines to Develop Robust Hard Thin Film Materials. *Prog. Mater. Sci.* **2024**, *146*, 101323.

(12) Jang, Y.-J.; Kim, J.-I.; Kim, W.; Kim, D. H.; Kim, J. Thermal Stability of Si/SiC/Ta-C Composite Coatings and Improvement of Tribological Properties through High-Temperature Annealing. *Sci. Rep.* **2022**, *12* (1), 3536.

(13) Lukose, C. C.; Anestopoulos, I.; Panagiotidis, I.-S.; Zoppi, G.; Black, A. M.; Dover, L. G.; Bowen, L.; Serrano-Aroca, Á.; Liu, T. X.; Mendola, L.; others. Biocompatible Ti3Au–Ag/Cu Thin Film Coatings with Enhanced Mechanical and Antimicrobial Functionality. *Biomater. Res.* **2023**, *27* (1), 93.

(14) Baptista, A.; Silva, F.; Porteiro, J.; Míguez, J.; Pinto, G. Sputtering Physical Vapour Deposition (PVD) Coatings: A Critical Review on Process Improvement and Market Trend Demands. *Coatings* **2018**, *8* (11), 402.

(15) Tian, Y.; Yan, Z.; Jiang, L.; Liu, R.; Liu, B.; Shao, Y.; Yang, X.; Liu, M. Multiscale Models of CVD Process: Review and Prospective. *Materials* **2024**, *17* (20), 5131.

(16) Oviroh, P. O.; Akbarzadeh, R.; Pan, D.; Coetzee, R. A. M.; Jen, T.-C. New Development of Atomic Layer Deposition: Processes, Methods and Applications. *Sci. Technol. Adv. Mater.* **2019**, *20* (1), 465–496.

(17) George, S. M. Atomic Layer Deposition: An Overview. *Chem. Rev.* **2010**, *110* (1), 111–131.

(18) Ehiasarian, A.; Hovsepian, P. E. Novel High-Efficiency Plasma Nitriding Process Utilizing a High Power Impulse Magnetron Sputtering Discharge. *J. Vac. Sci. Technol. A* **2024**, *42* (2).

(19) Ehiasarian, A.; Sugumaran, A.; Hovsepian, P. E.; Davies, C.; Hatto, P. Real-Time Monitoring of Plasma Synthesis of Functional Materials by High Power Impulse Magnetron Sputtering and Other PVD Processes: Towards a Physics-Constrained Digital Twin. *J. Phys. Appl. Phys.* **2022**, *56* (3), 035302.

(20) Knoops, H. C.; Potts, S. E.; Bol, A. A.; Kessels, W. Atomic Layer Deposition. In *Handbook of Crystal Growth*; Elsevier, 2015; pp 1101–1134.

(21) Dingemans, G.; Van Helvoirt, C.; Pierreux, D.; Keuning, W.; Kessels, W. Plasma-Assisted ALD for the Conformal Deposition of SiO2: Process, Material and Electronic Properties. *J. Electrochem. Soc.* **2012**, *159* (3), H277.

(22) Fryauf, D. M.; Phillips, A. C.; Bolte, M. J.; Feldman, A.; Tompa, G. S.; Kobayashi, N. P. Scaling Atomic Layer Deposition to Astronomical Optic Sizes: Low-Temperature Aluminum Oxide in a Meter-Sized Chamber. *ACS Appl. Mater. Interfaces* **2018**, *10* (48), 41678–41689.

(23) Ritala, M.; Leskelä, M.; Dekker, J.-P.; Mutsaers, C.; Soininen, P. J.; Skarp, J. Perfectly Conformal TiN and Al2O3 Films Deposited by Atomic Layer Deposition. *Chem. Vap. Depos.* **1999**, *5* (1), 7–9.

(24) Knoops, H.; Langereis, E.; Van De Sanden, M.; Kessels, W. Conformality of Plasma-Assisted ALD: Physical Processes and Modeling. *J. Electrochem. Soc.* **2010**, *157* (12), G241.

(25) Arts, K.; Deijkers, S.; Puurunen, R. L.; Kessels, W. M.; Knoops, H. C. Oxygen Recombination Probability Data for Plasma-Assisted Atomic Layer Deposition of SiO2 and TiO2. *J. Phys. Chem. C* **2021**, *125* (15), 8244–8252.

(26) Arts, K.; Utriainen, M.; Puurunen, R. L.; Kessels, W. M.; Knoops, H. C. Film Conformality and Extracted Recombination Probabilities of O Atoms during Plasma-Assisted Atomic Layer Deposition of SiO2, TiO2, Al2O3, and HfO2. *J. Phys. Chem. C* **2019**, *123* (44), 27030–27035.

(27) Kwon, O.-K.; Kwon, S.-H.; Park, H.-S.; Kang, S.-W. PE-ALD of a Ruthenium Adhesion Layer for Copper Interconnects. *J. Electrochem. Soc.* **2004**, *151* (12), C753.

(28) Musschoot, J.; Deduytsche, D.; Poelman, H.; Haemers, J.; Van Meirhaeghe, R.; Van den Berghe, S.; Detavernier, C. Comparison of Thermal and Plasma-Enhanced ALD/CVD of Vanadium Pentoxide. *J. Electrochem. Soc.* **2009**, *156* (7), P122.

(29) Kim, W.-H.; Maeng, W.; Moon, K.-J.; Myoung, J.-M.; Kim, H. Growth Characteristics and Electrical Properties of La2O3 Gate Oxides Grown by Thermal and Plasma-Enhanced Atomic Layer Deposition. *Thin Solid Films* **2010**, *519* (1), 362–366.

(30) Caubet, P.; Blomberg, T.; Benaboud, R.; Wyon, C.; Blanquet, E.; Gonchond, J.-P.; Juhel, M.; Bouvet, P.; Gros-Jean, M.; Michailos, J.; others. Low-Temperature Low-Resistivity PE-ALD TiN Using TDMAT under Hydrogen Reducing Ambient. *J. Electrochem. Soc.* **2008**, *155* (8), H625.

(31) Zhao, M.-J.; Zhang, Z.-X.; Hsu, C.-H.; Wu, W.-Y.; Zhang, X.-Y.; Lien, S.-Y.; Zhu, W.-Z. In2O3 Film Prepared by a PE-ALD Process with Balanced Oxygen Radical Supply and Ion Bombardment Damage. *Vacuum* **2021**, *192*, 110411.

(32) Elers, K.-E.; Winkler, J.; Weeks, K.; Marcus, S. TiCl4 as a Precursor in the TiN Deposition by ALD and PE-ALD. *J. Electrochem. Soc.* **2005**, *152* (8), G589.

(33) Van Bui, H.; Wiggers, F. B.; Gupta, A.; Nguyen, M. D.; Aarnink, A. A.; de Jong, M. P.; Kovalgin, A. Y. Initial Growth, Refractive Index, and Crystallinity of Thermal

and Plasma-Enhanced Atomic Layer Deposition AlN Films. *J. Vac. Sci. Technol. A* **2015**, *33* (1).

(34) Park, J.-S.; Park, H.-S.; Kang, S.-W. Plasma-Enhanced Atomic Layer Deposition of Ta-N Thin Films. *J. Electrochem. Soc.* **2001**, *149* (1), C28.

(35) Jiang, S.; Wu, W.-Y.; Ren, F.; Hsu, C.-H.; Zhang, X.; Gao, P.; Wuu, D.-S.; Huang, C.-J.; Lien, S.-Y.; Zhu, W. Growth of GaN Thin Films Using Plasma Enhanced Atomic Layer Deposition: Effect of Ammonia-Containing Plasma Power on Residual Oxygen Capture. *Int. J. Mol. Sci.* **2022**, *23* (24), 16204.

(36) Zeng, X.; Wu, Y.; He, G.; Zhu, W.; Ding, S.; Zeng, Z. High-Pure AlN Crystalline Thin Films Deposited on GaN at Low Temperature by Plasma-Enhanced ALD. *Vacuum* **2023**, *213*, 112114.

(37) Vos, M. F.; van Straaten, G.; Kessels, W. E.; Mackus, A. J. Atomic Layer Deposition of Cobalt Using H2-, N2-, and NH3-Based Plasmas: On the Role of the Co-Reactant. *J. Phys. Chem. C* **2018**, *122* (39), 22519–22529.

(38) Kim, J.; Kim, S.; Jeon, H.; Cho, M.-H.; Chung, K.-B.; Bae, C. Characteristics of HfO2 Thin Films Grown by Plasma Atomic Layer Deposition. *Appl. Phys. Lett.* **2005**, *87* (5).

(39) Raizer, Y. P.; Allen, J. E.; others. *Gas Discharge Physics*; Springer, 1997; Vol. 2.

(40) Chen, F. F.; others. *Introduction to Plasma Physics and Controlled Fusion*; Springer, 1984; Vol. 1.

(41) Schram, D. C. Is Plasma Unique? The Presence of Electrons and the Importance of Charge. *Plasma Sources Sci. Technol.* **2008**, *18* (1), 014003.

(42) Lieberman, M.; Lichtenberg, A. Principles of Plasma Discharges and Materials Procesing. 2 Nd Edn. Hoboken, NJ: John Wiley& Sons, 2005.

(43) Kong, M. G.; Kroesen, G.; Morfill, G.; Nosenko, T.; Shimizu, T.; Van Dijk, J.; Zimmermann, J. Plasma Medicine: An Introductory Review. *New J. Phys.* **2009**, *11* (11), 115012.

(44) Lee, C. G.; Kanarik, K. J.; Gottscho, R. A. The Grand Challenges of Plasma Etching: A Manufacturing Perspective. *J. Phys. Appl. Phys.* **2014**, *47* (27), 273001.

(45) d'Agostino, R.; Favia, P.; Kawai, Y.; Ikegami, H.; Sato, N.; Arefi-Khonsari, F. *Advanced Plasma Technology*; John Wiley & Sons, 2008.

(46) Conrads, H.; Schmidt, M. Plasma Generation and Plasma Sources. *Plasma Sources Sci. Technol.* **2000**, *9* (4), 441.

(47) Raizer, Y. P.; Shneider, M. N.; Yatsenko, N. A. *Radio-Frequency Capacitive Discharges*; CRC press, 2017.

(48) Riemann, K.-U. The Bohm Criterion and Sheath Formation. *J. Phys. Appl. Phys.* **1991**, *24* (4), 493.

(49) Godyak, V. A.; Piejak, R. B.; Alexandrovich, B. M. Electron Energy Distribution Function Measurements and Plasma Parameters in Inductively Coupled Argon Plasma. *Plasma Sources Sci. Technol.* **2002**, *11* (4), 525–543. https://doi.org/10.1088/0963-0252/11/4/320.

(50) Jang, S.; Lee, W. Pressure and Input Power Dependence of Ar/N2H2 Inductively Coupled Plasma Systems. *J. Vac. Sci. Technol. Vac. Surf. Films* **2001**, *19* (5), 2335–2343. https://doi.org/10.1116/1.1385904.

(51) Abdel-Rahman, M.; Gathen, V. S. D.; Gans, T.; Niemi, K.; Döbele, H. F. Determination of the Degree of Dissociation in an Inductively Coupled Hydrogen Plasma Using Optical Emission Spectroscopy and Laser Diagnostics. *Plasma Sources Sci. Technol.* **2006**, *15* (4), 620–626. https://doi.org/10.1088/0963-0252/15/4/005.

(52) Iordanova, S.; Koleva, I.; Paunska, T. Hydrogen Degree of Dissociation in a Low Pressure Tandem Plasma Source. *Spectrosc. Lett.* **2011**, *44* (1), 8–16. https://doi.org/10.1080/00387010903386540.

(53) Boffard, J. B.; Jung, R. O.; Lin, C. C.; Wendt, A. E. Optical Emission Measurements of Electron Energy Distributions in Low-Pressure Argon Inductively Coupled Plasmas. *Plasma Sources Sci. Technol.* **2010**, *19* (6), 065001. https://doi.org/10.1088/0963-0252/19/6/065001.

(54) Yoon, M. Y.; Jeong, J.-R.; Lee, H.-C.; Kim, J.-H. Plasma Low-Energy Ion Flux Induced Vertical Graphene Synthesis. *Appl. Surf. Sci.* **2023**, *636*, 157814. https://doi.org/10.1016/j.apsusc.2023.157814.

(55) Doh, H.-H.; Horiike, Y. Gas Residence Time Effects on Plasma Parameters: Comparison between Ar and C_4F_8. *Jpn. J. Appl. Phys.* **2001**, *40* (5R), 3419. https://doi.org/10.1143/JJAP.40.3419.

(56) Gordiets, B.; Ferreira, C. M.; Pinheiro, M. J.; Ricard, A. Self-Consistent Kinetic Model of Low-Pressure - Flowing Discharges: II. Surface Processes and Densities of N, H, Species. *Plasma Sources Sci. Technol.* **1998**, *7* (3), 379–388. https://doi.org/10.1088/0963-0252/7/3/016.

(57) Jiménez-Redondo, M.; Cueto, M.; Doménech, J. L.; Tanarro, I.; Herrero, V. J. Ion Kinetics in Ar/H_2 Cold Plasmas: The Relevance of ArH^+. *RSC Adv* **2014**, *4* (107), 62030–62041. https://doi.org/10.1039/C4RA13102A.

(58) Smith, G. J.; Diomede, P.; Gibson, A. R.; Doyle, S. J.; Guerra, V.; Kushner, M. J.; Gans, T.; Dedrick, J. P. Low-Pressure Inductively Coupled Plasmas in Hydrogen: Impact of Gas Heating on the Spatial Distribution of Atomic Hydrogen and Vibrationally Excited States. *Plasma Sources Sci. Technol.* **2024**, *33* (2), 025002.

(59) Heil, S. B. S.; Van Hemmen, J. L.; Van De Sanden, M. C. M.; Kessels, W. M. M. Reaction Mechanisms during Plasma-Assisted Atomic Layer Deposition of Metal Oxides: A Case Study for Al2O3. *J. Appl. Phys.* **2008**, *103* (10), 103302. https://doi.org/10.1063/1.2924406.

(60) Mione, M. A.; Engeln, R.; Vandalon, V.; Kessels, W. M. M.; Roozeboom, F. Infrared and Optical Emission Spectroscopy Study of Atmospheric Pressure Plasma-Enhanced Spatial ALD of Al2O3. *Appl. Phys. Lett.* **2019**, *115* (8), 083101. https://doi.org/10.1063/1.5113753.

(61) Van Straaten, G.; Deckers, R.; Vos, M. F. J.; Kessels, W. M. M.; Creatore, M. Plasma-Enhanced Atomic Layer Deposition of Cobalt and Cobalt Nitride: What Controls the Incorporation of Nitrogen? *J. Phys. Chem. C* **2020**, *124* (40), 22046–22054. https://doi.org/10.1021/acs.jpcc.0c04223.

(62) O'Donnell, S.; Snelgrove, M.; Shiel, K.; Weiland, C.; Hughes, G.; Woicik, J.; O'Neill, D.; Jose, F.; McFeely, C.; O'Connor, R. Growth Chemistry of Cobalt Nitride by Plasma Enhanced Atomic Layer Deposition. *Mater. Res. Express* **2022**, *9* (10), 106402.

(63) Fan, Q.; Sang, L.; Jiang, D.; Yang, L.; Zhang, H.; Chen, Q.; Liu, Z. Plasma Enhanced Atomic Layer Deposition of Cobalt Nitride with Cobalt Amidinate. *J. Vac. Sci. Technol. Vac. Surf. Films* **2019**, *37* (1), 010904. https://doi.org/10.1116/1.5062842.

(64) Wu, L.; Eisenbraun, E. Hydrogen Plasma-Enhanced Atomic Layer Deposition of Copper Thin Films. *J. Vac. Sci. Technol. B Microelectron. Nanometer Struct. Process. Meas. Phenom.* **2007**, *25* (6), 2581–2585. https://doi.org/10.1116/1.2779050.

(65) Muneshwar, T.; Cadien, K. Probing Initial-Stages of ALD Growth with Dynamic in Situ Spectroscopic Ellipsometry. *Appl. Surf. Sci.* **2015**, *328*, 344–348.

(66) Jussila, T.; Philip, A.; Tripathi, T.; Nielsch, K.; Karppinen, M. Atomic Layer Deposition of Magnetic Thin Films: Basic Processes, Engineering Efforts, and Road Forward. *Appl. Phys. Rev.* **2023**, *10* (4), 041313. https://doi.org/10.1063/5.0172732.

(67) Hagen, D. J.; Pemble, M. E.; Karppinen, M. Atomic Layer Deposition of Metals: Precursors and Film Growth. *Appl. Phys. Rev.* **2019**, *6* (4), 041309. https://doi.org/10.1063/1.5087759.

2 Experimental Details

2.1 Overview

Understanding how plasma conditions influence thin film properties is critical in plasma-enhanced atomic layer deposition (PE-ALD) processes[1]. This chapter outlines the experimental methodology developed to investigate that relationship, integrating plasma diagnostics, in-situ process monitoring, and surface characterisation. The experimental work is structured in three stages: (1) pre-deposition plasma diagnostics, (2) in-situ plasma monitoring during deposition, and (3) post-deposition thin film characterisation. Together, these stages enable a comprehensive evaluation of how process parameters influence plasma behaviour, and how this behaviour in turn affects film growth and quality.

The first stage focused on characterising the plasma in isolation using both invasive and non-invasive diagnostics[2,3]. Key process variables, namely inductively coupled plasma (ICP) power (W), chamber pressure (mTorr), and plasma feed-gas flow (sccm), were systematically varied to assess their influence on plasma behaviour. These measurements established a baseline for comparison with the plasma conditions observed during PE-ALD processing.

In the second stage, PE-ALD processes were conducted using selected parameter sets informed by the initial diagnostics. Thin films were deposited on silicon wafers using a range of metal-organic precursors in combination with reactive plasma species. During deposition, in-situ optical emission spectroscopy (OES) was employed to monitor the plasma environment in real time, enabling comparison between pre-ALD plasma conditions.

Finally, immediately following deposition, in-situ X-ray photoelectron spectroscopy (XPS) was used to characterise the films[4,5] without exposure to atmosphere. This allowed for accurate measurement of film thickness[6], chemical and elemental composition. Since the films were transferred under high vacuum conditions, any observed impurities could be attributed to incomplete surface reactions rather than environmental exposure, enabling a direct correlation between plasma conditions and film quality.

To support this experimental strategy, this chapter is organised into three main sections. The first section, “Instrumentation and Experimental Setup”, describes the integrated ALD/XPS cluster tool and the high-vacuum environment maintained throughout the study. The second section, “Plasma Diagnostics”, details the plasma characterisation techniques, including both optical emission spectroscopy (OES) and the ion flux probe, as well as the corresponding analysis methods. The final section, “Deposition and Film Characterisation”, outlines the PE-ALD process parameters, chamber configuration, and the in-situ XPS methodology used to assess the chemical and structural properties of the deposited thin films.

2.2 Instrumentation and Experimental Setup

All experimental work in this thesis utilised a state-of-the-art industrial PE-ALD with integrated XPS cluster tool, as seen in Figure 2.1. The tool's configuration enables precise thin film deposition with both chemical and elemental film characterisation without exposure to atmospheric contamination.

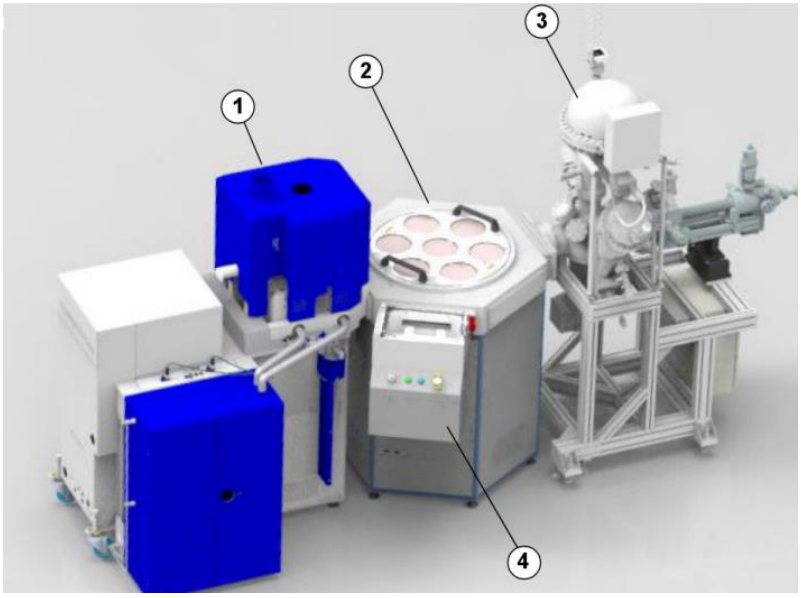


Figure 2.1 - Schematic of the state-of-the-art ALD/XPS cluster tool[7].

The system, which was manufactured in a collaboration between Oxford Instruments and Scienta Omicron, consists of four modules, as labelled in Figure 2.1:

1. An industry used, remote ICP source PE-ALD processing chamber.
2. A transfer chamber housing a robotic hexapod wafer handler.
3. A monochromatic Al source XPS with 128 channel charge-coupled device (CCD) detector.
4. A load lock port to ensure sufficient vacuum is maintained in the cluster tool.

Samples were mounted on 4-inch carrier wafers and introduced into the system via the load lock. Base pressures of the PE-ALD, transfer, and XPS chambers were on the order of 10^{-6}, 10^{-7}, and 10^{-9} mTorr, respectively. This high-vacuum environment was essential to prevent contamination and preserve the surface chemistry of the thin films[8].

The integrated cluster tool architecture was central to the experimental workflow. Following plasma-enhanced ALD processing in the PE-ALD chamber, samples were transferred under vacuum to the XPS module using the robotic hexapod transfer arm. This direct, evacuated transfer path eliminated atmospheric exposure, enabling surface-sensitive characterisation of the as-deposited films. All modules were controlled using a dedicated control software, allowing for recipe-driven processing, automated sequencing, and minimal user intervention.

Each module operated with an independent vacuum system to maintain chamber pressures. The PE-ALD chamber and XPS system were pumped using turbomolecular pumps, with the PE-ALD chamber backed by a dual Edwards iH600 dry vacuum pumping system was used to back the turbomolecular pump. The iH600 is an oil-free mechanical vacuum system comprised of an HCDP80 dry primary pump coupled with an HCMB600 mechanical booster pump mounted at the inlet. This configuration enables efficient pumping from atmospheric pressure to the operating range of the turbomolecular pump. The system incorporates a controlled purge gas supply, and the absence of lubricating fluids within the pumping chambers ensures a hydrocarbon-free environment, minimising the risk of contamination via back-migration. Gate valves and interlocks ensured vacuum isolation between modules as required.

Samples were secured to the carrier wafers using conductive silver paint to ensure both thermal contact and charge dissipation. Prior to loading, wafers were sonicated in

isopropyl alcohol which was followed by N_2 drying before immediately loading onto the carrier wafer. The wafer was then placed inside the load lock and evacuated until a baseline pressure of 10^{-2} mTorr was reached before being moved to the appropriate chamber.

The capabilities of the integrated cluster tool offered a level of process control and analytical precision that would be challenging to replicate using non-integrated instrumentation. The in-situ nature of the surface analysis following deposition was essential for understanding plasma-surface interactions which occurred during deposition. However, the system had certain limitations, most notably the absence of in-line ellipsometry or in-situ thickness monitoring. This limitation was mitigated by utilising the effective attenuation length of the substrate signal in the XPS measurements after deposition to calculate the film thickness[6]. In this approach, photoelectrons emitted from the substrate must travel through the deposited film before reaching the detector, and their intensity decreases exponentially as a function of film thickness due to inelastic scattering within the overlayer. By comparing the attenuated substrate signal to that of the clean substrate and applying the known effective attenuation length of the electrons in the film material, the thickness of the deposited layer can be estimated. However, to utilise the effective attenuation length calculation, ultra-thin films were required, and as-such this work investigated the initial stage-growth for each PE-ALD process selected.

2.3 Plasma Diagnostic Methods

2.3.1 Optical Emission Spectroscopy

2.3.1.1 Overview

Optical Emission Spectroscopy (OES) is a non-invasive diagnostic technique widely used in plasma processing applications, including etching endpoint detection[9]. It operates by detecting light emitted from excited atomic and molecular species within the plasma. When plasma species undergo electronic transitions, returning from excited to lower energy states, they can emit photons at characteristic wavelengths correlating to the energy between the states. The resulting light is collected and spectrally resolved to produce emission spectra, with each peak corresponding to a specific transition. These emission peaks offer insight into plasma composition, excitation dynamics, and the relative presence of reactive species.

In this study, OES is employed both for pre-ALD plasma characterisation and for in-situ monitoring during the PE-ALD process. The diagnostic focus and selected emission lines were based on the plasma feed-gas composition. For ammonia-containing plasmas, the selected emission peaks were the NH 0-0 band transition (336 nm, $A^3\Pi–X^3\Pi$)[10] and the H-alpha line (656 nm, Balmer n=3→2 transition)[11]. In plasmas containing pure hydrogen, the selected emission peaks were the H-alpha line and H-beta (486 nm, Balmer n=4→2) line[11]. Argon was added to some gas compositions and the strong argon line at 750 nm ($2p_1 \rightarrow 1s$ transitions)[12] was used in these cases.

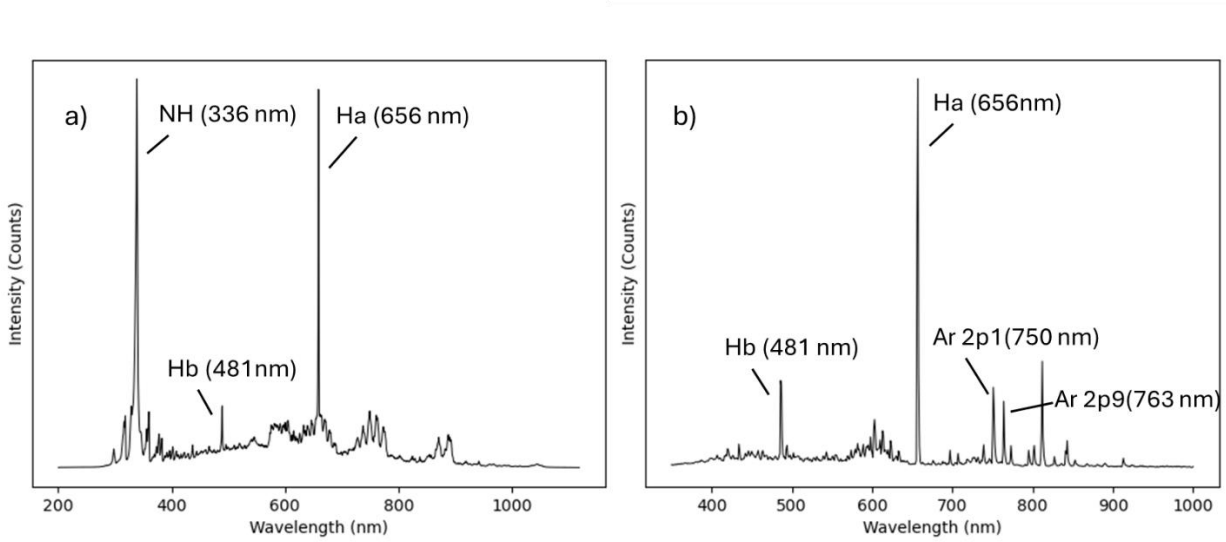


Figure 2.2 - OES spectra of (a) ammonia plasma spectra, collect by the Maya 2000 Pro spectrometer and (b) hydrogen/argon plasma spectra, collected by the USB2000+ spectrometer, with highlighted key emission lines.

In low-temperature plasmas such as those used in PE-ALD, free electrons absorb energy from the applied radio frequency (RF) field. These energetic electrons can collide with neutral gas species, causing direct electron-impact excitation, where an electron within a neutral atom or molecule is promoted to an excited state. The return of these excited species to lower energy states can occur through spontaneous radiative de-excitation, resulting in the emission of photons, which is the light that OES detects.

However, this is not the only pathway through which excited states are populated or de-populated. Additional processes include stepwise excitation where excitation occurs from metastable levels rather than the ground state, photon reabsorption where emitted photons may be reabsorbed by nearby electrons before escaping and collisional de-excitation where energy is lost through collisions without photon emission. These non-radiative processes can suppress or distort the observable emission. As such, OES analysis is most

effective in optically thin plasmas, where emitted photons can escape without being reabsorbed or quenched.

The excitation probability of specific species is often known as the excitation cross section. The cross section will have an energy threshold, above which excitation can occur. However, these cross sections are often complex, and the excitation will depend on the electron energy distribution function (EEDF) within the plasma. Methods such as Boltzmann equation solvers (e.g. BOLSIG+) are often used to simulate the EEDF and compute effective excitation rate coefficients. They utilise excitation cross sections from databases, such as LXCat[13], to influence their calculations. These tools can be useful for more advanced diagnostics.

An extension of OES is actinometry, which allows for the quantitative estimation of atomic species densities by introducing a known concentration of tracer gas with a well understood emission behaviour. By comparing the emission intensities of the target and tracer species, and assuming similar excitation mechanisms, the target ground state densities can be calculated. This technique forms the basis for more sophisticated energy-resolved diagnostics, which are addressed in the Data Analysis section.

While OES is a powerful and non-intrusive diagnostic method, several limitations must be considered:

- Undetectable species: Species that lack emission lines in the spectrometer's range, are not sufficiently excited, or de-excite via non-radiative pathways will not appear in the spectra.
- Spectral overlap: Emission peaks may overlap, especially in complex plasmas. To address this, high-resolution spectrometers were used where needed, and dominant, non-overlapping lines were prioritised.

- Instrument limitations: Limited spectral resolution and signal sensitivity can affect detection of weak or closely spaced lines.

To mitigate these challenges, spectrometers with appropriate spectral ranges and resolutions were selected (see Table 2.1). Spectral response calibration and background subtraction were applied to all spectra, allowing for meaningful comparison between relative emission intensities and spectra.

2.3.1.2 Technical Details

Three Ocean Optics spectrometers were used in this work with the specifications listed in table 2.1 below. For the initial work a broad range Maya 2000 Pro was used with a high-resolution Flame-T USB 4000 for investigation into overlapping emission peaks. For the rest of the work a broad range USB 2000+ was used.

Table 2.1 - Spectrometer specifications.

Spectrometer	Range (nm)	Resolution (nm)	Grating (lines/mm)	Slit width (um)
Maya 2000 Pro	200-1100	0.82	300	25
Flame-T	300-500	0.13	1800	25
USB2000+	350-1000	0.6	600	25

Each spectrometer was connected via optical fibre to a collection lens system mounted at a viewport with a direct line of sight into the inductively coupled plasma (ICP) dielectric tube as seen in Figure 2.3. The spectrometers were operated with an integration time of 250 ms, corresponding to the temporal resolution of the optical emission spectroscopy (OES) measurements. Plasma exposure steps in PE-ALD typically occur on timescales of several seconds, with complete ALD cycles on the

order of tens of seconds. This integration time was sufficient to resolve changes in emission intensity during plasma steps. The RF cycle of the plasma, which occurs on nanosecond timescales, was not captured.

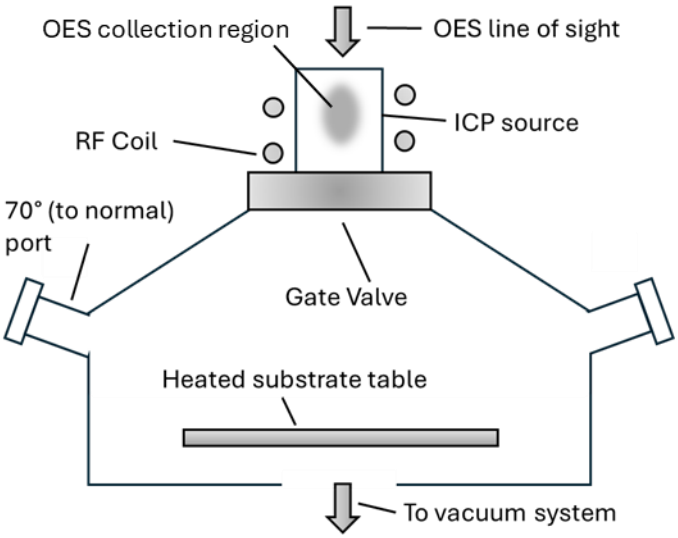


Figure 2.3 - Schematic of ALD chamber with labelled features and OES viewport.

The ICP coil was approximately 100 mm in length, and the distance from the viewport to the coil centre was approximately 100 mm. The lens, with an 80 mm focal length, was focused 150 mm inside the viewport, targeting the centre of the plasma. Both the viewport and lens materials were transparent across the 300–1000 nm spectral range. The ICP source was positioned approximately 250 mm from the heated substrate table. No changes to the spatial setup were made throughout the experiments, ensuring consistent spatial sampling.

Two primary gas compositions were studied. Initial experiments used an ammonia plasma for pre-ALD characterisation and PE-ALD processes. In these cases, OES diagnostics focused solely on emission peak intensities and their ratios without applying further modelling. In later work, H_2 and Ar plasmas were introduced to allow for more

complex modelling and interpretation of plasma behaviour. The process parameters included variations in ICP power, chamber pressure, and gas mixture flow rates for both gas compositions.

OES data acquisition parameters (e.g. integration time per scan) were varied to optimise signal intensity relative to plasma conditions. All spectra underwent background subtraction. As the chamber was well-shielded from external light sources, the background signal was minimal. Multiple measurements were recorded for each process condition to enable averaging and calculation of standard deviations, which were used when appropriate.

In Chapter 5 and 6, time-resolved OES was employed to assess plasma stability over process duration. Although the time resolution (~250 ms per measurement) was significantly longer than the RF cycle, these studies focused on broader trends in plasma stability rather than phase-resolved analysis of the RF cycle itself.

Wavelength calibration was factory-set for the spectrometers and validated using several pure-gas plasmas. Identified emission peaks were compared with values from the Nation Institute of Standard and Technology (NIST) Atomic Spectra Database[14]. Spectral response calibration was carried out using a calibrated tungsten-halogen lamp for each spectrometer[15]. A correction factor was generated and applied to all raw spectral data, enabling a more insightful comparisons of peak emission intensities and their ratios.

2.3.1.3 Data Analysis

The analysis of the OES data was separated into two methods, an initial qualitative investigation into emission intensities and line ratios, and an in-depth quantitative

actinometry based analysis. The initial investigation provided a foundation for the more in-depth analysis. Both analysis methods included several key steps.

The first step in the analysis involved identifying all visible emission lines in the acquired spectra. Each detected peak was matched to transitions listed in the NIST Atomic Spectra Database, ensuring accurate assignment of spectral features. Following identification, emission intensities were calculated using the spectrometers calibration factor, obtained from a tungsten-halogen calibration lamp.

For the qualitative analysis, emission peak intensities and ratios were then analysed to infer trends in plasma behaviour. To obtain quantitative plasma features, a more advanced diagnostic technique, Energy-Resolved Actinometry (ERA), as described by Greb et al[16], was used. ERA extends classical actinometry by accounting for the dependence of excitation processes on the electron energy distribution function (EEDF) by including the dissociative excitation pathways. Selected intensities from Hydrogen and Argon species were utilised along with theoretical models allowing for the simultaneous determination of the molecular hydrogen dissociation rate and local mean electron energy of a plasma.

The three key emission lines selected for this analysis were the H-Balmer series lines of H-Alpha and H-Beta and the Ar $2p_1$ line as previously mentioned above. These lines were chosen based on their visibility in the spectra, diagnostic significance, and well-characterised electron-impact excitation cross-sections. Argon was used as the actinometric gas due to its stable emission characteristics[17].

To utilise the energy resolved actinometry approach, several derivations must be considered. The time averaged emission peak intensity is given by (2.1):

$$< I >_{rf} = hva_{ik} < k_e n_e > n_0 \qquad (2.1)$$

where hv is the photon energy, a_{ik} is the optical branching ratio, k_e is the excitation rate coefficient, n_e is the electron density and n_0 is the ground state density. Classic actinometry utilises equation 2.1 for the ratio of two emission peaks, with the ground state density of the actinometer peak known. However, by introducing the dissociative excitation pathway and following the same procedure taken in classical actinometry a new equation is found (2.2):

$$n_H = \left(I_H h v_{Ar} k^*_{Ar,d} a_{ik,Ar} / I_{Ar} h v_H k^*_{H,d} a_{ik,H}\right) n_{Ar} - (k^*_{H_2,de} / k^*_{H,d}) n_{H_2} \qquad (2.2)$$

$$\text{where } k^* = < k_e n_e >_{rf} / < n_e >_{rf}.$$

k^* is the effective excitation rate coefficient with the direct electron impact excitation denoted by d and dissociative electron impact excitation denoted by de.

From the measured intensity, a pressure independent excitation function $E_i(x,t)$, can be calculated by (2.3) below.

$$E_i(x,t) = 1/n_0 \left(dn_i(x,t)/dt + n_i(x,t)/\tau_{eff}\right) \quad (2.3)^{18}$$

Equation (2.3) represents a rate balance for the population of the excited state. The excitation function corresponds to the rate at which ground state species are excited into state i, normalised by the ground state density. The term $dn_i(x,t)/dt$ describes the temporal change in the excited state population, while $n_i(x,t)/\tau_{eff}$ represents the loss of excited species through spontaneous radiative decay and collisional quenching. The excitation function therefore represents the excitation rate required to balance the observed population dynamics of the emitting state.

$$\text{where } n_i \propto I_i(x,t)/A_{ik} h v_i.$$

$n_i(x,t)$ is the time and space dependent excited state density, A_{ik} is the Einstein coefficient of spontaneous decay, τ_{eff} is the effective lifetime of the excited state which takes collisional quenching into consideration through the relationship (2.4),

$$\tau_{eff} = 1/(\sum_k A_{ik} + \sum_k n_{ik} q_{ik}) \qquad (2.4)$$

in which the sum of all Einstein coefficients of possible lower states and collisional decay channels are considered. Here, q_{ik} represents the collisional quenching rate coefficient for collisions between the excited species i and collision partner k, and n_{ik} is the corresponding density of the quenching species.

To account for all possible electron-impact excitation channels the sum over all products of the electron-impact excitation rates, $E^e_{i,n}$, and density fraction, f_n, of the gas species are considered.

$$E^* = \sum_n f_n E^e_{i,n} \qquad (2.5)$$

As such, the total effective excitation rate for the selected hydrogen line is the combination of the individual rates and hydrogen density fraction which results in the relationship (2.6):

$$E^*_H = f_{H_2}(r_H k_{H,d}(\varepsilon) + k_{H_2,de}(\varepsilon)) \qquad (2.6)$$

where $r_H = n_H/n_{H_2}$is the degree of dissociation and ε is the mean electron energy. Similar derivatives can be made with the Argon line without the need for dissociative excitation and a set of effective excitation ratio of a selected hydrogen/argon line pair can be calculated leaving two equations, (2.7) and (2.8) below, with two unknown variables, namely r_H and ε.

$$\frac{E_{Ha}}{E_{Ar}} = \frac{f_{H_2}}{f_{Ar}} \frac{r_H k_{Ha,d}(\varepsilon) + k_{Ha,de}(\varepsilon)}{k_{Ar}} \qquad (2.7)$$

$$\frac{E_{Hb}}{E_{Ar}} = \frac{f_{H_2}}{f_{Ar}} \frac{r_H k_{Hb,d}(\varepsilon) + k_{Hb,de}(\varepsilon)}{k_{Ar}} \qquad (2.8)$$

Where Hα and Hβ represent the H-alpha and H-beta lines, respectively. From our measured intensity, excitation ratios are acquired and used to simultaneous solve both the degree of dissociation and the mean electro energy.

Due to the nature of the spectral acquisition, the measured emission intensities represent an average over many RF cycles. While the ERA method, as described above, is based on time- and space-dependent excitation, practical measurements integrate over timescales significantly longer than the RF period. In such cases, atomic species densities can be assumed constant within each cycle, whereas the electron energy is strongly modulated as discussed by Waskoenig et al[19]. Consequently, the extracted electron energy from ERA reflects a cycle-averaged energy, weighted by the periods of strongest excitation. To enable comparison of results, all emission data was collected from the bulk plasma region, as the sheath region will have different electron energy, as such the mean electron energy is termed "local mean electron energy", as it is the bulk plasma mean electron energy.

To evaluate the rate coefficients as a function of electron energy, the two-term Boltzmann equation was solved using BOLSIG+[20], a widely adopted solver for electron energy distribution function (EEDF) modelling in low-temperature plasmas. The two-term Boltzmann equation is a simplification of the Boltzmann transport equation in which the electron velocity distribution function is expanded in Legendre polynomials and truncated after the first two terms. This approach assumes that the electron energy distribution is approximately isotropic, allowing the electron energy distribution function (EEDF) to be determined from the balance between energy gained from the electric field and energy lost in collisions with background gas species. The two-term formulation is

widely employed in low-temperature plasma modelling to calculate electron transport coefficients and rate coefficients for electron-impact processes. The solver requires input parameters such as gas composition, gas temperature, and relevant electron-impact excitation cross sections.

In this study, direct and dissociative excitation cross sections for the Hα and Hβ emission lines were taken from Lavrov and Pipa[21], while the direct excitation cross section for the Ar ($2p_1$) state was obtained from Chilton et al[22]. Cross sections for argon metastable and resonance states were taken from Gangwar et al[23], and additional electron–molecule collision cross sections for H_2, including vibrational excitation contributions, were obtained from the Phelps[24] dataset via the LXCat Project.

The ERA method in this work was modified from the method described by Greb et al[16] to include a different gas composition, mixture ratio and pressure regime. As such, original assumption made do not hold, such as the excitation from ground state only for Ar $2p_1$. This assumption for a high pressure O_2 with tracer Ar holds as the O_2 quenching of Ar is approximately 50 times greater than self quenching[25]. Trace amounts of Ar ~2-5% also reduced the density of these states. At high pressure, the 1sX states are further quenched from collisions[26]. These contributions result in the assumption of negligible contribution of the 1sX states to be valid. In this work, the Ar gas content is increased, H_2 quenching of Ar is an order of magnitude low then that of O_2[25] and a lower pressure regime reduced overall collisional quenching. As a result of these key changes, a significant contribution of the 1sX states, as discussed by Boffard et al[26], must be assumed. This contribution cannot be assumed negligible or constant with changes in power and pressure as further described by Boffard. To address this, an estimated density for 1s2,1s3, 1s4 and 1s5 was used. The densities were calculated using interpolated results

from the work of Boffard et al[26] allowing for a first order approximate to be fed into the Bolsig+ calculations.

While the pressure regime remains low, collisional quenching was considered. The relevant quenching rates fall into three categories: (1) Argon quenched by H_2[25], (2) Argon self-quenching (Ar quenched by Ar)[25], and (3) Hydrogen Balmer lines quenched by H_2.

For category (3), the quenching rate was calculated as the product of the thermal velocity of H_2 at 500 K and the quenching cross section for the respective Balmer transition[27]. It was assumed that all quenching of the Balmer lines occurred via collisions with H_2, using the densities of H_2, as molecules quench much stronger than atoms due to more available energy states[25].

The dominant source of systematic uncertainty in the ERA measurements come from the electron-impact excitation cross sections of the Hα and Hβ Balmer lines. Lavrov and Pipa[21] report variations of 15 – 30 % between experimental datasets and theoretical calculations and demonstrate that dissociative excitation of Hb can differ by up to an order of magnitude. A conservative estimate of ~30% systematic uncertain is attributed to the method. Other inputs such as the Ar ($2p_1$) excitation cross sections are better constrained and therefore do not contribution as significantly to the uncertainty estimate.

2.2.2 Ion Flux Probe

2.2.2.1 Overview

A remote inductively coupled plasma (ICP) source was used for all experimental work, as previously mentioned. Non-invasive optical emission spectroscopy (OES) was performed at the plasma source to characterise its behaviour. The OES collection was

performed through a viewport directly above the plasma generation region of the remote ICP source, as illustrated in Figure 2.3. The optical fibre and lens system were positioned to collect emission along a line of sight into the bulk plasma of the source, ensuring that the measured signal reflects the plasma characteristics at the point of generation rather than at the substrate surface. As the plasma is generated remotely, reactive species subsequently undergo transport before reaching the substrate location, and the OES measurement does not directly capture the plasma environment experienced at the wafer.

To gain insight into this transport behaviour, an invasive ion flux probe was installed at the substrate level. In this work, the measured ion flux is used as a first-order approximation for the transport of reactive species. This assumes that, over the transport distance, ions and reactive neutrals/radicals experience similar transport trends. While this approximation provides a useful comparative indicator for process optimisation in PE-ALD, it does not capture the full behaviour of neutral or radical species, which may differ in multiple ways including wall loss probability and recombination rates. The relative changes in flux rates due to experimental parameters provide an insight into the key reactive species transport. However, it has been seen that ions with energies below the film-damage threshold can be beneficial in densifying and improving the crystallinity of films[28].

2.2.2.2 Technical details

The ion flux probe is an invasive diagnostic tool that allows direct measurement of the ion current arriving at a small metallic collection disc exposed to the plasma. The operational principle is shown schematically in Figure 2.4. The disc is connected to a known resistor and is held at a constant negative bias to repel electrons and attract ions.

When ions strike the collection disc, current flows through the resistor, producing a voltage drop. Under ion-saturation conditions, the ion saturation current, I_{sat}, can be related to the ion density, n_i, by (2.9) below:

$$n_i = I_{sat}/A\sqrt{eT_e/M} \qquad (2.9)$$

Where A is the probe collection area, M is the ion mass, e is the elementary charge and T_e is the electron temperature.

In practice, ion saturation current, I_{sat}, can be obtained from the measured voltage drop across the resistor via Ohm's law. Although this current is related to ion density through equation 2.9, in this work the analysis is simplified by using the measured voltage drop directly as the indicator of ion flux. The probe was operated with fixed geometry, resistor value, and bias voltage, so any change in the voltage reflects a relative change in the collected ion current under different plasma conditions. However, because parameters such as T_e and M were not measured for every condition, the results are interpreted solely in terms of relative trends in charged particle transport rather than as absolute densities or flux.

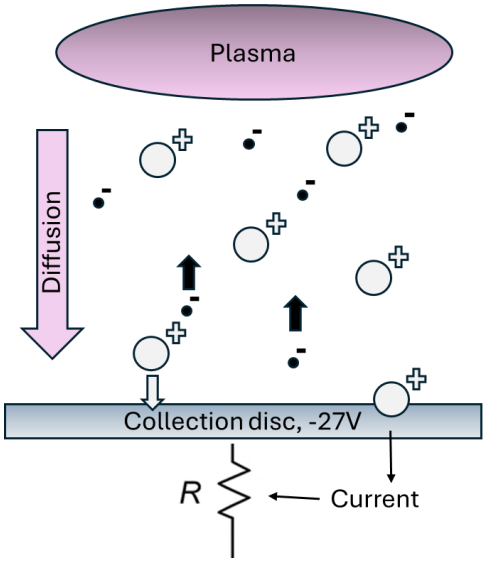


Figure 2.4 - Operating principle of ion flux probe with negative collection bias.

Due to the invasive nature of the probe, measurements were taken only during non-ALD processes to avoid contamination and deposition on the probe. The probe was mounted to the ALD chamber via a 70° KF-valve port, as seen in Figure 2.3, with the tip positioned approximately 50 mm above the substrate location. Given the ~250 mm separation between the plasma source and the substrate, this arrangement provided a representative measurement of ion transport from source to surface. The collection disc (2 mm diameter) was mounted on a SiO_2 dielectric tube for electrical isolation, with an internal wire connecting the disc to the electronics (shown in Figure 2.5).

The ion flux was measured using a biased collection probe with a 10 kΩ resistor and a negative 27 V bias applied to the collection disc. The floating potential is the potential at which the net current to a probe immersed in plasma is zero, meaning the electron and ion fluxes to the probe are balanced. The plasma potential is the potential within the plasma bulk relative to a reference (often ground) and represents the energy barrier ions must overcome to reach surfaces. Although the floating potential was not measured

directly in this experiment, the probe was placed downstream of the plasma source, where the plasma is already partially diffused and possibly cooled, so the local plasma potential is expected to be positive relative to the walls. The probe bias of – 27 V was chosen to ensure operation in the ion saturation region, where primarily ion current is collected with minimal electron contribution, providing reliable ion flux measurements. While RF fields from the source can modulate the sheath and influence probe current, the use of a large series resistor and DC voltage measurement mitigates these effects.

Once ion saturation was reached, voltage readings across the resistor were recorded with a digital multimeter. The measured voltage (in millivolts) is directly proportional to the ion current collected by the probe, with the proportionality determined by the resistor value, sampling area, and bias voltage. Conversion to physical ion flux units (ions/cm²·s) can be achieved by multiplying by a calibration constant derived from the probe geometry and operating conditions. n this work, the values are reported directly in millivolts. For each condition, multiple readings were recorded, and the mean and standard deviation were calculated to characterise the ion flux.

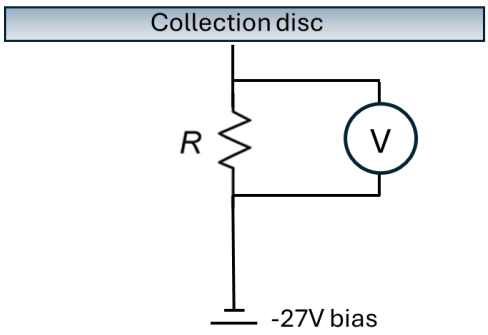


Figure 2.5 - Basic schematic of ion flux probe electronic circuit.

While the ion flux signal obtained from the probe provides useful comparative insight into transport behaviour, it should be interpreted as a first-order approximation of reactive species transport. This is because ions and neutrals or radicals can exhibit different transport physics and losses.

2.3 Thin Film Deposition and Characterisation

2.3.1 Deposition system configuration

2.3.1.1 ALD Chamber

The atomic layer deposition (ALD) processes conducted in this work were performed using a Flex AL 2 system, a commercially available, industrial-grade deposition tool designed for both thermal ALD and plasma-enhanced ALD. A schematic of the system layout can be seen in Figure 2.6.

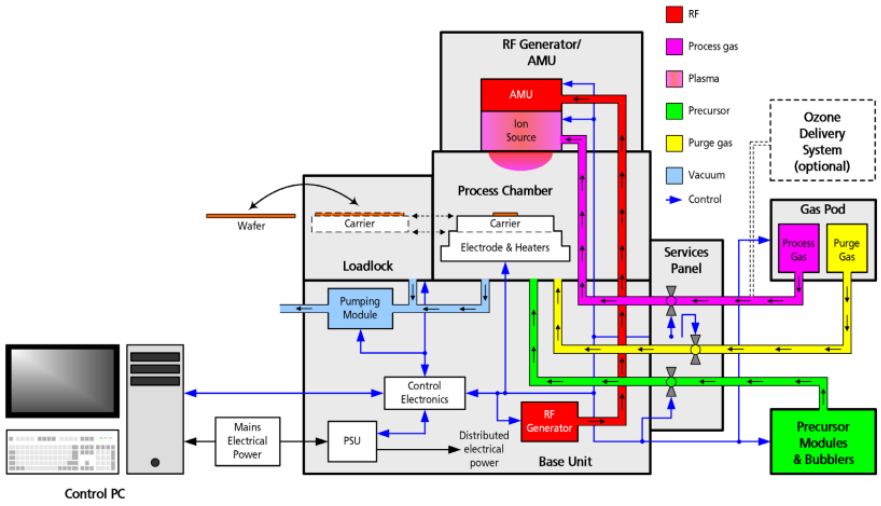


Figure 2.6 - ALD system layout[7].

The tool is a single-wafer reactor, compatible with 4-inch (100 mm) substrates. There is an aluminium conical shaped chamber with precursor inlets at the substrate level and a remote plasma at the top of the chamber. The process chamber is equipped with a mechanically grounded lower electrode, which also serves as the substrate heater. Heating is controlled through a programmable logic controller (PLC) and can reach temperatures

up to 400 °C with ±5 °C accuracy. The uniform heating ensures stable reaction conditions, which is essential for maintaining the self-limiting surface reactions typical of ALD[29].

The gas delivery system is designed with separate lines for ALD precursors, purge gases, and plasma process gases, as seen in Figure 2.6. The system is configured with three precursor input lines, and it supports both vapor-draw and bubbler configurations, offering flexibility for a wide range of chemistries. Each precursor line is independently heated and includes Swagelok High-Performance ALD pneumatic valves with response time of approximately 5ms, enabling precise control over precursor dosing, pulse timing, and purge sequences. Argon is used as the carrier and purge gas.

The vacuum system consists of a turbo-molecular pump (Edwards nEXT 240d) backed by an Edwards iH600 dry pump, allowing the system to reach a base pressure of approximately 1×10^{-6} Torr. This low base pressure minimises background contamination, ensuring high-purity film deposition. During processing, the operating pressure can be dynamically adjusted between 5 and 200 mTorr, depending on the requirements of the ALD cycle and plasma conditions. The high pumping speed and controlled pressure environment help maintain precursor and co-reactant isolation, preventing unwanted CVD-like behaviour. A difference of approximately 4 orders of magnitude between base and operating pressures also minimises the contribution of background gases to plasma chemistry and film growth, which is important in PE-ALD, as described by Sønsteby et al.[30]

The system is fully automated and interfaced through a user-controlled recipe platform, allowing for flexible programming of ALD cycles, including time control of precursor pulses, purges and plasma exposure duration. This level of control is essential for systematic studies of plasma-surface interactions, especially when evaluating time-

dependent phenomena and plasma diagnostics. However, due to the limitations of the automated system, it is currently not possible to modify the plasma parameters during the process. As a result, there is no capability for the implementation of a feedback loop system currently.

2.3.1.2 Plasma Source

The plasma source integrated into the Flex AL 2 system is a remote inductively coupled plasma (ICP) source, which is widely used in PE-ALD due to its ability to generate a high-density plasma while minimising direct ion bombardment of the substrate[28]. The plasma is generated in an insulating quartz tube positioned upstream of the process chamber, approximately 250 mm away from the substrate plane.

Plasma generation is driven by a 13.56 MHz radio frequency (RF) generator, which delivers up to 300 W of power through an automatic matching unit (AMU) to an external planar RF coil wrapped around the quartz tube. The matching network continuously tunes the impedance of the system to ensure efficient power transfer between the RF generator and the plasma load. The use of an AMU is essential, as it compensates for changes in plasma impedance that occur during the ALD cycle maintaining stable plasma conditions across different recipes[31].

The configuration of the AMU is shown in Figure 2.7, which includes two tuneable capacitors (C1 and C2) arranged in an L-type matching network, along with fixed padding capacitors. This configuration enables dynamic impedance matching between the 13.56 MHz RF generator and the plasma load, ensuring efficient power transfer to the inductively coupled plasma. The entire plasma control system is integrated into the Flex AL control software, allowing for recipe-based adjustments of RF power, gas flow, and

plasma exposure duration. Process gases such as O_2, N_2, NH_3, Ar, and H_2 can be introduced into the plasma source independently enabling flexibility in plasma chemistry and surface activation.

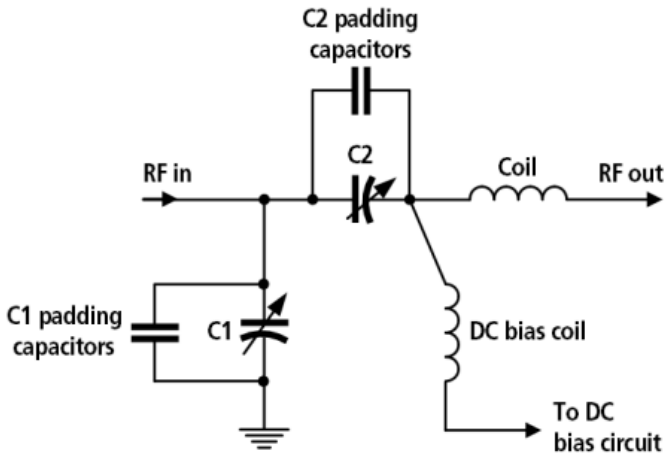


Figure 2.7 - Automatic match unit schematic diagram[7].

2.3.2 X-ray Photoelectron Spectroscopy (XPS)

2.3.2.1 Overview

X-ray Photoelectron spectroscopy (XPS) is a non-destructive surface characterisation technique which provides information on the chemical structure of the surface of a material. The technique is based on the interaction between x-rays with the atoms on a surface. The x-ray interaction with the surface creates free electrons via photoemission. This phenomenon, also known as the photoelectric effect, is the transfer of energy from photons to the electrons of the surface atoms, resulting in the electrons escaping. The energy with which the electrons escape the atom depends on the incidence photon energy and the binding energy of both the orbital and atom. The binding energy of the photoelectron can be calculated using Equation 2.10, where K_e is the kinetic energy of

the photoelectron, hv is the energy of the incident x-ray, B_e is the binding energy and Φ is the work function of the spectrometer.

$$K_e = hv - B_e - \Phi \quad (2.10)$$

Detection and analysis of the photoelectrons reveal information not only about the specific atom and orbital the photoelectron originates from but also the chemical state of the atom. This is due to the impact the chemical bonds on an atom have on its binding energy. XPS is a powerful technique which reveals a lot of information about thin film and film-substrate interfaces.

2.3.2.2 Technical Details

A typical XPS set up consists of an x-ray source, analyser and detector in a high to ultra-high vacuum (HV-UHV) environment. The vacuum is usually necessary as it increases the mean free path of the electrons emitted, which must travel from the substrate surface through to the detector without collision. A schematic can be seen in Figure 2.8. Electrons are generated through thermoemission and are accelerated towards an anode via a large bias in the order of kV's. The electrons impact with the anode which is coated in a metal usually Al or Mg due to their narrow linewidths for characteristic K-alpha radiation[32]. This produces characteristic x-rays which can be passed through a monochromator before ultimately interacting with the sample under analysis. The interaction produces photoelectrons, which are passed into the hemispherical analyser. This separates the electrons based on energy. Electrons with the correct energy, determined by the pass energy, are then collected by the detector which counts the number of electrons detected. By varying the electron pass energy in the analyser, energy resolved spectra are produced.

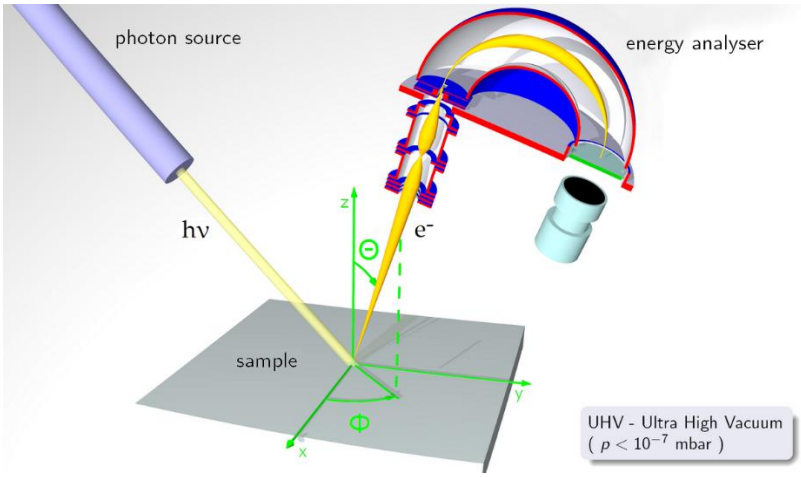


Figure 2.8 - XPS operational schematic[33].

The characteristics x-rays produced by the anode target material can often have multiple energies which if used can produce spectra with ghost features. A monochromator is used to isolate an energy providing a spectrum with higher resolution. Aluminium is a common target material providing K-alpha x-rays of energies 1486.7 eV (K-alpha 1) and 1486.27eV (K-alpha 2)[34] and is used in this work. A monochromator can isolate the K-alpha 1 line increasing the resolution. Figure 2.9 shows a $Ag\ 3d$ peak with and without a monochromator. All measurements in this work utilised a monochromator, allowing the energy resolution of approximately 300 meV.

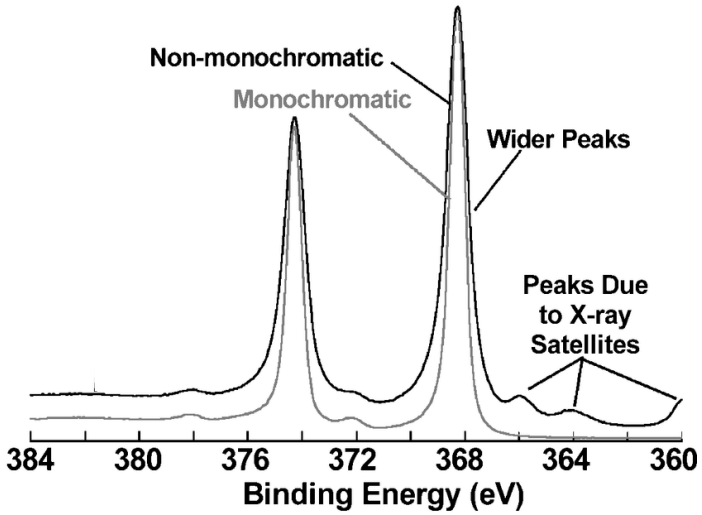


Figure 2.9 - Ag 3d peak with and without monochromator[35].

Deceleration plates within the XPS system control the kinetic energy of electrons entering the analyser, allowing the scanning of electron energies to produce spectra. The hemispherical analyser then separates electrons according to their kinetic energy using two concentric electrodes of radii $R_1$and $R_2$for the inner and outer hemispheres, respectively. The electrons will only arrive at the detector if their energy is equal to the pass energy which is defined by (2.11).

$$E = e\Delta V\left(\frac{R_1 - R_2}{R_2^2 - R_1^2}\right) \qquad (2.11)$$

E is the energy required to pass, e is the charge of an electron and ΔV is the potential difference between the inner and outer electrode.

The analyser can have two operational modes: Constant Retardation Ratio (CRR) or Constant Analyser Energy (CAE) and they sweep through the energy range defined by the user to provide spectra. In CAE mode, the electron energies are modified to reach a user defined energy known as the pass energy. The resolution of the spectra is increased as the pass energy is reduced. However, there is a corresponding decrease in the electron

count with the reduced pass energy. CAE provides a constant resolution and is used for all measurements in this work.

XPS utilises the different binding energies of electrons in atoms and molecules to determine chemical structure and composition of a film, while film thickness is determined from the attenuation of substrate signal intensities. An atom has multiple electrons in orbital energy levels. The emission of an electron from these energy levels requires a threshold energy also known as a binding energy. The binding energies are specific to the atom and the orbital energy level the emitted electron originated from. For example, $Si\ 2p$ and $Al\ 2p$ have binding energies of 99.4 eV and 73 eV respectively[34]. The binding energies are determined by the atom which the electron originates from as well as the distance from the nucleus. The unique nature of an element's orbital binding energies allows XPS to determine the composition of a sample using peaks in the spectra.

The chemical environment also impacts the binding energies through chemical shifts. When an electron originates from a $Si\ 2p$ orbital which is chemically bonded to only Si, the resulting binding energy will be 99.4 eV as previously mentioned. However, in SiO_2 the Si is now bonded with O which has an increased electronegativity of 3.44 compared to Si which has 1.9. This electronegativity increases in the Si-O bonds which increases the binding energy due to the electron 'being pulled' more strongly by the O or in other words the electron density shifts towards the O atom. The increased strength of this 'pull' is realised in the $Si\ 2p$ peak by an increased binding energy of 103.5 eV characterised by the 4th oxidation state of Si because of the surrounding four O atoms[36]. Variations in the oxidation state from 0th (Si) to 4th (SiO_2) can be identified by XPS allowing the user to gain insight into the chemical structure of the sample under investigation.

2.3.2.3 Data Analysis

The depth sensitivity of XPS is approximately 8 nm or less depending on the material[37]. The limitation is a result of inelastic collisions of the photoelectrons due to the MFP of the material. X-rays incident on the sample generates photoelectrons at a depth d within the sample with an initial intensity I_0. For the photoelectrons to be detected they must escape the material without changes in their energy because off collisions. The final intensity I_k of photoelectrons which undergo this process is described by the Beer Law equation:

$$I_k = I_0 e^{(-d/\lambda_{IMFP}\cos\theta)} \qquad (2.12)$$

Where λ_{IMFP} is the inelastic mean free path (IMFP) of the material and θ is the take of angle with respect to the normal. The IMFP is both dependent on the element and orbital which the photoelectrons originate as well as the material which the photoelectron is passing through.

Quantitative measurements via XPS require knowledge of elemental cross sections. As discussed in a previous section, a cross section is the probability of an event to occur. For XPS the elements orbitals all have a cross section for achieving photoelectron emission. The photoemission peak intensity of a homogeneous material is defined as:

$$I_p = J\rho\sigma K\lambda_{IMFP} \qquad (2.13)$$

Where J is the photon flux, ρ is the concentration of the element in the material, σ is the cross section for the element (and orbital) and K is a constant for instrumental factors. I_p can be calculated from either the maximum intensity or more commonly the peak area. Relative sensitivity factors (RSF) for common orbitals of most elements have been collected into databases[38]. CasaXPS software[39] utilises such a its own database allowing

for direct comparison between elements. From the RSF the determination of the materials composition is calculated by (2.14).

$$Element\ A(\%) = \left[\frac{I_A/RSF_A}{\Sigma_I/RSF}\right] x\ 100 \qquad (2.14)$$

Where I is the intensity of the element. All elemental composition was calculated using CasaXPS's built in function. Equation (2.14) provides a first-order estimate of elemental composition based on sensitivity factor normalisation and assumes a homogeneous sample. In practice, additional corrections related to the analyser transmission function and variations in scattering volume with electron kinetic energy can influence quantitative results and are not explicitly included in this simplified formulation. For ultrathin films on substrates, signals may originate from different depths, meaning the calculated atomic percentages can be systematically skewed. As a result, the absolute values in this work should be considered an approximation. However, as all samples were analysed consistently, relative compositional changes between processes remain reliable. Powell and Seah[40] show that quantitative XPS measurements are limited primarily by systematic uncertainties, which are generally much larger than the random noise typically reported by the instrument. Their analysis demonstrates that even under well-controlled conditions, quantitative XPS can carry uncertainties of up to 10%, arising from factors such as uncertainties in sensitivity factors, inelastic mean free paths (IMFPs), and instrument-dependent parameters. At the same time, they note that XPS can exhibit very high precision. Compositional changes of 2% are measurable, meaning that film-to-film comparisons using XPS provides excellent relative precision. Accordingly, a 10% uncertainty is assumed for all calculated elemental compositions to account for these intrinsic limitations of the technique. In addition, CasaXPS's built-in Monte Carlo function was used to estimate peak-fitting uncertainties by repeatedly refitting noise-

perturbed spectra, demonstrating that the derived fit parameters are largely resistant to realistic noise variations and providing error estimates for the fit.

As previously mentioned, the XPS peaks can be affected by chemical shifts. Other influencing factors also include charging effects and spin-orbital splitting. Sample charging is a result of the removal of photoelectrons from the material. If the material doesn't allow movement of electrons to replenish the photoelectrons, then an attractive force occurs between the positively charged material and the bound electrons. This is represented by the increases in the binding energy throughout the measurement. Methods are available to replace the emitted photoelectrons for charge sensitive samples, typically dielectrics, by using electron flood guns.

Spin orbital splitting or j-j coupling is a result of the degeneracy of the spin state for the orbital. All orbitals, except for those with zero angular momentum (s orbitals) result in two peaks in XPS which is known as orbital splitting. The peak ratios are calculated via Equation 2.15 below.

$$j = l + s \qquad (2.15)$$

Where j is the degeneracy of the spin state, l is the angular momentum and s is the spin angular momentum which is ± ½. For example, a Si 2p spectra results in j values of ½ and ³⁄₂ as the angular momentum is 1. This is recognised in XPS spectra by two peaks in the Si 2p peak area with ratios of 2:1, for $2p_{3/2}$:$2p_{1/2}$. The Coster-Kronig effect is an exception to this. The Coster-Kronig effect limits the lifetime of the electron holes due to Auger processes within the orbital resulting in a broadening of peaks but reducing the peak intensity, so the peak area remains the same[41].

Inelastic collisions which occur in the material contribute to the formation of a background within the XPS spectra. The background grows after all major peaks are a

result of the scattering from the orbital contribute to the background. The Shirley Sherwood background is a common background type used in XPS analysis software for peak fitting. It utilises the peak areas to proportionally increase the background after the peak in an iterative process for increased accuracy.

Film thickness was determined using X-ray Photoelectron Spectroscopy (XPS) by applying the concept of the effective attenuation length (EAL), a material-dependent parameter that describes the average distance an electron of known kinetic energy can travel through a solid before undergoing inelastic scattering. The EAL is critical for interpreting XPS spectra when analysing thin films, as it governs the attenuation of substrate signals by an overlayer.

To calculate the EAL, the software tool developed by NIST, known as the NIST Electron Effective Attenuation Length Database[42], was employed. This program allows for the estimation of the EAL based on either pre-defined reference materials or user-defined parameters such as inelastic mean free path (IMFP), density, and bandgap of the overlayer material. The program simulates the attenuation of the substrate signal as a function of overlayer thickness. The underlying principle is described by equation 2.12 which relates the ratio of the substrate signal intensity before and after deposition to the thickness of the overlayer and the EAL.

By comparing the measured attenuation of the substrate signal with simulated values, the film thickness can be accurately extracted, provided the substrate signal remains detectable post-deposition. This requirement limits the effective measurement range to include the substrate signal so a max film thickness of approximately 8 nm. Therefore, the number of atomic layer deposition (ALD) cycles was kept deliberately low to maintain substrate signal visibility and enable full film characterisation. Pre-deposition

spectra were always collected to serve as a reference for signal attenuation calculations. A uncertainty of 10.2 % was applied to all thicknesses based on element-specific IMFP/EAL error reported by Powell and Jablonski[42].

2.4 References

(1) Profijt, H.; Potts, S.; Van de Sanden, M.; Kessels, W. Plasma-Assisted Atomic Layer Deposition: Basics, Opportunities, and Challenges. *J. Vac. Sci. Technol. A* **2011**, *29* (5).

(2) Wang, S.; Wendt, A. E.; Boffard, J. B.; Lin, C. C.; Radovanov, S.; Persing, H. Noninvasive, Real-Time Measurements of Plasma Parameters via Optical Emission Spectroscopy. *J. Vac. Sci. Technol. A* **2013**, *31* (2).

(3) Bogdanova, M.; Lopaev, D.; Zyryanov, S.; Voloshin, D.; Rakhimova, T. Relation between the Ion Flux and Plasma Density in an Rf CCP Discharge. *Plasma Sources Sci. Technol.* **2018**, *27* (2), 025003.

(4) Fukumizu, H.; Sekine, M.; Hori, M.; McIntyre, P. C. Initial Growth Analysis of ALD Al2O3 Film on Hydrogen-Terminated Si Substrate via in Situ XPS. *Jpn. J. Appl. Phys.* **2020**, *59* (1), 016504.

(5) O'Donnell, S.; Jose, F.; Shiel, K.; Snelgrove, M.; McFeely, C.; McGill, E.; O'Connor, R. Thermal and Plasma Enhanced Atomic Layer Deposition of Ultrathin TiO2 on Silicon from Amide and Alkoxide Precursors: Growth Chemistry and Photoelectrochemical Performance. *J. Phys. Appl. Phys.* **2021**, *55* (8), 085105.

(6) Powell, C. J.; Jablonski, A. Electron Effective Attenuation Lengths for Applications in Auger Electron Spectroscopy and X-Ray Photoelectron Spectroscopy. *Surf. Interface Anal. Int. J. Devoted Dev. Appl. Tech. Anal. Surf. Interfaces Thin Films* **2002**, *33* (3), 211–229.

(7) Oxford Instruments. *FlexAL II Plasma ALD System User Manual*; Oxford Instruments Plasma Technology, 2018.

(8) Pelissier, B.; Kambara, H.; Godot, E.; Veran, E.; Loup, V.; Joubert, O. XPS Analysis with an Ultra Clean Vacuum Substrate Carrier for Oxidation and Airborne Molecular Contamination Prevention. *Microelectron. Eng.* **2008**, *85* (1), 151–155.

(9) Jansen, H.; Gardeniers, H.; de Boer, M.; Elwenspoek, M.; Fluitman, J. A Survey on the Reactive Ion Etching of Silicon in Microtechnology. *J. Micromechanics Microengineering* **1996**, *6* (1), 14.

(10) Ni, T.; Yu, S.; Ma, X.; Kong, F. NH (A3Π→ X3Σ-) Emission from 193 Nm Two-Photon Photolysis of NH3. *Chem. Phys. Lett.* **1986**, *126* (5), 413–416.

(11) Wiese, W. L.; Smith, M. W.; Glennon, B. Atomic Transition Probabilities. Volume 1. Hydrogen through Neon. **1966**.

(12) Wiese, W. L.; Smith, M. W.; Miles, B. *Atomic Transition Probabilities. Volume 2. Sodium through Calcium*; 1969.

(13) LXCat. LXCat Database, 2025. https://us.lxcat.net/data/set_type.php.

(14) Ralchenko, Y.; Jou, F. C.; Kelleher, D. E.; Kramida, A. NIST Atomic Spectra Database, 2025. https://www.nist.gov/pml/atomic-spectra-database.

(15) Optics, O. *Halogen Calibration Light Source HL-2000-CAL*; Ocean Optics.

(16) Greb, A.; Niemi, K.; O'Connell, D.; Gans, T. Energy Resolved Actinometry for Simultaneous Measurement of Atomic Oxygen Densities and Local Mean Electron Energies in Radio-Frequency Driven Plasmas. *Appl. Phys. Lett.* **2014**, *105* (23).

(17) Naz, M.; Shukrullah, S.; Khan, Y.; Ghaffar, A.; Rehman, N.; Ullah, S. Actinometry Study on Dissociation Fraction in Low Pressure Capactively Coupled Ar–O2 Mixture Plasma. *High Energy Chem.* **2015**, *49* (6), 449–458.

(18) Gans, T.; O'Connell, D.; Schulz-Von Der Gathen, V.; Waskoenig, J. The Challenge of Revealing and Tailoring the Dynamics of Radio-Frequency Plasmas. *Plasma Sources Sci. Technol.* **2010**, *19* (3), 034010.

(19) Waskoenig, J.; Niemi, K.; Knake, N.; Graham, L.; Reuter, S.; Schulz-Von Der Gathen, V.; Gans, T. Atomic Oxygen Formation in a Radio-Frequency Driven Micro-Atmospheric Pressure Plasma Jet. *Plasma Sources Sci. Technol.* **2010**, *19* (4), 045018.

(20) Hagelaar, G. J. M.; Pitchford, L. C. Solving the Boltzmann Equation to Obtain Electron Transport Coefficients and Rate Coefficients for Fluid Models. *Plasma Sources Sci. Technol.* **2005**, *14*, 722–733. https://doi.org/10.1088/0963-0252/14/4/014.

(21) Lavrov, B.; Pipa, A. Account of the Fine Structure of Hydrogen Atom Levels in the Effective Emission Cross Sections of Balmer Lines Excited by Electron Impact in Gases and Plasma. *Opt. Spectrosc.* **2002**, *92* (5), 647–657.

(22) Chilton, J. E.; Boffard, J. B.; Schappe, R. S.; Lin, C. C. Measurement of Electron-Impact Excitation into the 3 p 5 4 p Levels of Argon Using Fourier-Transform Spectroscopy. *Phys. Rev. A* **1998**, *57* (1), 267.

(23) Gangwar, R. K.; Sharma, L.; Srivastava, R.; Stauffer, A. D. Argon Plasma Modeling with Detailed Fine-Structure Cross Sections. *J. Appl. Phys.* **2012**, *111* (5), 053307. https://doi.org/10.1063/1.3693043.

(24) Phelps, A. V. Cross Sections and Swarm Coefficients for H+ , H2+ , H3+ , H, H2, and H- In H2 for Energies from 0.1 eV to 10 keY. *J Phys Chem Ref Data* **1990**, *19*.

(25) Sadeghi, N.; Setser, D.; Francis, A.; Czarnetzki, U.; Döbele, H. Quenching Rate Constants for Reactions of Ar (4p′[1/2], 4p [1/2], 4p [3/2] 2, and 4p [5/2] 2) Atoms with 22 Reagent Gases. *J. Chem. Phys.* **2001**, *115* (7), 3144–3154.

(26) Boffard, J. B.; Jung, R. O.; Lin, C. C.; Wendt, A. E. Optical Emission Measurements of Electron Energy Distributions in Low-Pressure Argon Inductively Coupled Plasmas. *Plasma Sources Sci. Technol.* **2010**, *19* (6), 065001. https://doi.org/10.1088/0963-0252/19/6/065001.

(27) Wouters, M.; Khachan, J.; Falconer, I.; James, B. Quenching of Excited Ar I and H by H2 in a Gas Discharge. *J. Phys. B At. Mol. Opt. Phys.* **1999**, *32* (12), 2869.

(28) Profijt, H. B.; Kessels, W. Ion Bombardment during Plasma-Assisted Atomic Layer Deposition. *ECS Trans.* **2013**, *50* (13), 23.

(29) Van Hemmen, J.; Heil, S.; Klootwijk, J.; Roozeboom, F.; Hodson, C.; Van de Sanden, M.; Kessels, W. Plasma and Thermal ALD of Al2O3 in a Commercial 200 Mm ALD Reactor. *J. Electrochem. Soc.* **2007**, *154* (7), G165.

(30) Sønsteby, H. H.; Yanguas-Gil, A.; Elam, J. W. Consistency and Reproducibility in Atomic Layer Deposition. *J. Vac. Sci. Technol. A* **2020**, *38* (2).

(31) Bacelli, G.; Ringwood, J.; Iordanov, P. Impedance Matching Controller for an Inductively Coupled Plasma Chamber: L-Type Matching Network Automatic Controller. **2007**.

(32) Citrin, P.; Eisenberger, P.; Marra, W.; Åberg, T.; Utriainen, J.; Källne, E. Linewidths in X-Ray Photoemission and x-Ray Emission Spectroscopies: What Do They Measure? *Phys. Rev. B* **1974**, *10* (4), 1762.

(33) Chemistry LibreTexts. Photoelectron Spectroscopy, 2021. https://chem.libretexts.org/Bookshelves/Physical_and_Theoretical_Chemistry_Textbook_Maps/Surface_Science_(Nix)/05%3A_Surface_Analytical_Techniques/5.03%3A_Photoelectron_Spectroscopy (accessed 2021-06-10).

(34) Thompson, A.; Attwood, D.; Gullikson, E.; Howells, M.; Kortright, J.; Robinson, A.; others. X-Ray Data Booklet (2009). *URL Httpxdb Lbl Gov* **2009**.

(35) Watts, J. F.; Wolstenholme, J. *An Introduction to Surface Analysis by XPS and AES*; John Wiley & Sons, 2019.

(36) Rumble Jr, J.; Bickham, D.; Powell, C. The NIST X-Ray Photoelectron Spectroscopy Database. *Surf. Interface Anal.* **1992**, *19* (1–12), 241–246.

(37) López-Santos, M.; Yubero, F.; Espinós, J.; González-Elipe, A. Non-Destructive Depth Compositional Profiles by XPS Peak-Shape Analysis. *Anal. Bioanal. Chem.* **2010**, *396* (8), 2757–2768.

(38) XPS Library. XPS Library: X-Ray Photoelectron Spectroscopy Reference Database, 2025. https://xpslibrary.com/.

(39) CasaXPS. CasaXPS — X-Ray Photoelectron Spectroscopy Software, 2025. http://www.casaxps.com/.

(40) Powell, C. J.; Seah, M. P. Precision, Accuracy, and Uncertainty in Quantitative Surface Analyses by Auger-Electron Spectroscopy and x-Ray Photoelectron Spectroscopy. *J. Vac. Sci. Technol. Vac. Surf. Films* **1990**, *8* (2), 735–763. https://doi.org/10.1116/1.576956.

(41) Coster, D.; Kronig, R. de L. New Type of Auger Effect and Its Influence on the X-Ray Spectrum. *Physica* **1935**, *2* (1–12), 13–24.

(42) Powell, C. J.; Jablonski, A. The NIST Electron Effective-Attenuation-Length Database. *J. Surf. Anal.* **2002**, *9* (3), 322–325.

3 Plasma optimisation and in-situ film characterisation of Co PE-ALD

3.1 Introduction

This chapter examines the growth of cobalt nitride (CoN) via plasma-enhanced atomic layer deposition. Cobalt nitride is a material with a wide range of applications including adhesion promotion/barrier layer for copper interconnects in back end of line (BEOL) semiconductor manufacturing processes[1,2]. Electron transport within Cu interconnects is impacted by surface scattering and grain boundary scattering[3]. As feature sizes in complementary metal oxide semiconductor (CMOS) processes shrink, interconnect widths decrease, leading to more frequent electron collisions. This increased resistance (R), combined with higher capacitance (C) between interconnects due to reduced spacing, significantly increases the circuits' RC delay and limits performance[4,5]. To tackle these effects, low resistance, adhesion promoting diffusion barrier layers, such as CoN, are investigated. These materials help maximise the volume of Cu available for conduction, reducing electron scattering and lowering resistance, while also providing an additional material for electron transport.

PE-ALD produced Cobalt nitride (CoN) has competitively low resistivity, approximately 180 $\mu\Omega$cm [6], to other barrier layers such as TaN, approximately 240 $\mu\Omega$cm[7], while providing a low phase mismatch (~1% for Co_4N) with Cu which promotes strong bonding[1]. A wide range of precursors have been explored for ALD of cobalt-containing films, with Bis(cyclopentadienyl)cobalt(II) ($CoCp_2$) and cyclopentadienyl cobalt dicarbonyl ($CpCo(CO)_2$) among the most prominent. $CoCp_2$, like other metallocene precursors, is known to be difficult to reduce due to the carbon-metal bond stability within the precursor[8], making an investigation into processing plasma optimisation desirable.

Previous work from Van Stratten et al. demonstrated the temperature-dependence of $CoCp_2$ and NH_3 plasma PE-ALD processing, with cobalt nitride formation below 260 °C, metallic cobalt above 350 °C and a mixed phase at intermediate temperatures[9]. O'Donnell et al utilised an integrated ALD/XPS cluster tool to show that, under fixed plasma conditions, $CoCp_2$ had significant carbon contribution due to incomplete Cp removal[10]. Vos et al identified NH radicals as the critical plasma species responsible for Cp ligand removal, providing molecular-level insight into the mechanism[11].

The mentioned studies provide vital information for the understanding of $CoCp_2$ and NH_3 PE-ALD process. However, except for Vos et al, no investigation into the plasma processing parameters was performed. Vos et al investigated plasma feed-gas mixing ratio but no investigation into other plasma processing parameters was conducted. A systemic investigation into how plasma operating conditions influence ligand removal and carbon incorporation is lacking.

In this chapter, the deposition of cobalt nitride films from $CoCp_2$ and NH_3 plasma is studied using optical emission spectroscopy (OES) as an in-situ plasma diagnostic method. Building on previous work by O'Donnell et at, which reported high carbon incorporation under fixed plasma conditions, three plasma parameters, ICP power, chamber pressure, and NH_3 flow, were systematically varied to examine their influence on plasma chemistry and film quality. A pre-ALD investigation was performed and from the gathered data two optimisation strategies were employed. The first was maximising the NH (336 nm) emission peak intensity, motivated by the role of NH radicals in Cp removal. The second strategy was maximising the NH:Hα ratio, providing a relative measure of NH excitation against hydrogen excitation. The optimised plasmas obtained by these strategies are benchmarked against a reference condition from the O'Donnell et al work, as the current work utilised the same system.

Deposition experiments were conducted under these plasma conditions, with OES monitoring during the process. Following deposition, the resulting films were characterised by in-situ XPS enabling direct correlation between plasma features and film composition. Comparisons were also drawn between pre-deposition plasma behaviour and plasma behaviour during ALD to assess the influence of the ALD environment on plasma dynamics.

There were two main objectives of this study. The first was to establish whether OES, utilising only emission peaks and ratios, can guide plasma optimisation along with provide in-situ diagnostics. The second was to determine if correlations between plasma features and film properties can be obtained. This study therefore demonstrates the potential of OES as a practical tool for non-invasive diagnostics and monitoring for the CoN PE-ALD process.

3.2 Experimental Details

Cobalt nitride thin films were deposited by plasma-enhanced ALD using bis(cyclopentadienyl)cobalt(II) ($CoCp_2$, Merck), heated to 80 °C, as the metal precursor and NH_3 plasma as the co-reactant. Each ALD cycle consisted of a 3 s $CoCp_2$ dose at 15 mTorr, followed by a 3 s Ar purge and a 6 s pump step. The NH_3 plasma step was applied for 10 s in all cases, after which the chamber was purged with Ar for 3s and pumped for 3 s before the next cycle. The substrate temperature was maintained at 270 °C.

Films were deposited on Si substrates with native oxide. Prior to deposition, substrates were cleaned in an isopropanol (IPA) sonicated bath for 10 min, dried under N_2 flow, and loaded into the system's load lock. A pretreatment consisting of a 3 min O_2 plasma exposure followed by a 3 min NH_3 plasma exposure was performed on all samples, as in previous work, to clean and functionalise the surface. Post-treatment Si 2p XPS measurements indicated a surface oxide thickness of 0.8 nm, determined using the method of Jensen et al.[12]

Each experiment comprised of 15 ALD cycles, producing thin cobalt-containing films. Film thickness was calculated via Si 2p signal attenuation in post-deposition XPS, as described in Chapter 2. After deposition, samples were transferred to the XPS chamber via the robotic handler under vacuum. Survey spectra were collected over 900–0 eV binding energy at 100 eV pass energy. High-resolution spectra of all identified elements were acquired at 50 eV pass energy. All spectra were analysed using CasaXPS software with a Shirley–Sherwood background. Binding energies were referenced to the Si $2p_{3/2}$ peak at 99.4 eV, with care taken to account for the overlap of Si 2p and Co 3s peaks.

3.3 Results

This chapter presents the results of plasma diagnostics and film characterisation in three main sections. First, pre-ALD plasma diagnostics was performed to establish how the parameters, namely ICP power, chamber pressure, and NH_3 feed-gas flow, influence the plasma behaviour and OES features. This provides a baseline understanding of plasma behaviour isolated from the ALD environment. From this understanding, an optimised plasma parameter set was identified.

Second, these selected parameter set was applied during PE-ALD operation. In-situ plasma monitoring via OES was performed and the measurements allowed for post-deposition analysis. Comparison with the pre-ALD data reveals how the plasma environment is modified by precursor introduction.

Finally, the resulting film properties were characterised via XPS. Variations in film thickness, composition, and chemical bonding states are presented as a response to the parameter sets, enabling identification of optimised processes and highlighting the limitations of basic OES measurement diagnostics when considered in isolation. Together, these results establish the relationship between plasma conditions, reactive species dynamics, and PE-ALD film properties, forming the basis for the discussion in Section 3.4.

3.3.1 Pre-ALD Plasma diagnostics

3.3.1.1 NH emission intensity

The initial analysis focused on the absolute intensity of the NH (336 nm) emission line, a species identified by Vos et al. as critical for Cp ligand removal in $CoCp_2$ PE-ALD using

NH_3. Figure 3.1 shows the normalised NH intensity as a function of ICP power, chamber pressure, and NH_3 flow.

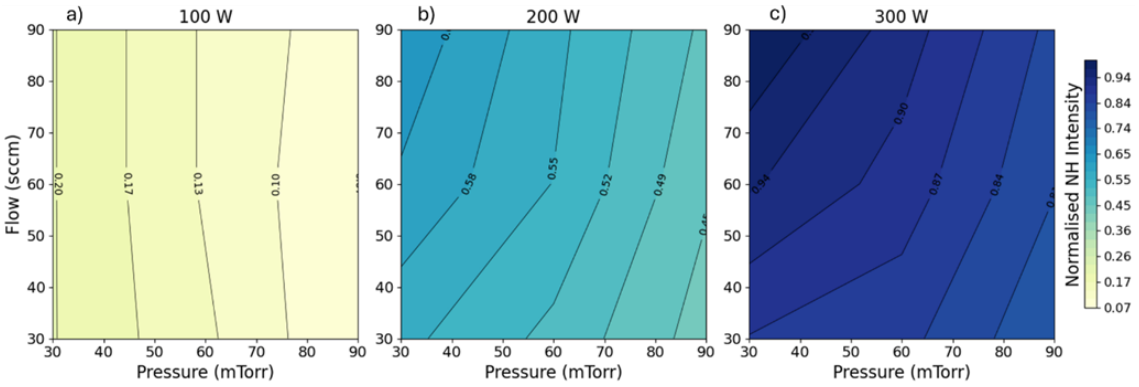


Figure 2.1 - NH emission intensity contour plot for feed-gas flow (sccm) vs chamber pressure (mTorr) for a) 100 W, b) 200 W and c) 300 W ICP power.

Increasing the ICP power resulted in a substantial increase in the NH emission intensity. At 100 W, the NH intensity ranged between 10 – 20 % of the emission intensity of the maximum. A significant increase was observed at 200 W, which had a range between ~45 % to 60 % of the maximum intensity. However, 300 W had the highest range between 85 – 100 % of the maximum. The significant increase suggests both the NH density and excitation efficiency are both improved with power.

In contrast, increasing chamber pressure consistently reduced NH intensity. At higher pressures more species are available for excitation. However, this also reduced the mean free path of energetic electron, reducing the excitation/dissociation ability. The increased pressure's reduction of NH intensity was also power and flow dependent but led to an average decrease of approximately 10 – 15 % from the maximum intensity.

The effect of NH_3 flow rate was found to be dependent on plasma power. At low power, increasing flow had little impact on NH emission, which could suggest low overall dissociative ability of the plasma. However, at higher powers increasing the NH_3 flow increased NH intensity. This suggests a higher throughput of neutral species allows for more radical production and excitation.

The reference process (100 W, 30 mTorr, 60 sccm) produced relatively weak NH emission, with a normalised intensity of 0.2. The most intense NH emission was observed under high power and flow with low pressure conditions (300 W, 30 mTorr, 90 sccm). This parameter set was therefore selected as the NH-optimised process for subsequent study.

3.3.1.2 NH:H theoretical production

To complement the experimental OES analysis, the relative production of NH radicals and atomic hydrogen from NH_3 dissociation was investigated using a reaction cross-section model. Snoeckx et al.[13] reported cross sections for the NH_3 dissociation pathways, which were used as inputs to the BOLSIG+ solver to calculate rate coefficients under varying electron energies. The effective rate coefficients, K, for each dissociation channel were obtained by summing the contributions of all associated sub-channels:

$$K_{x,y} = \sum_i k_{x,y}^i \qquad (3.1)$$

where $k_{x,y}^i$ are the rate coefficients for individual channels. Three key pathways were considered:

- K_{31}: $NH_3 \rightarrow NH + H_2$
- K_{32}: $NH_3 \rightarrow NH_2 + H$

- K_{21} : $NH_2 \rightarrow NH + H$

The production rate of NH radicals can then be written as:

$$\frac{dn_{\mathrm{NH}}}{dt} = K_{31} n_{NH_3} + K_{21} n_{NH_2} \qquad (3.2)$$

and the production rate of atomic hydrogen as:

$$\frac{dn_{\mathrm{H}}}{dt} = K_{32} n_{NH_3} + K_{21} n_{NH_2} \qquad (3.3)$$

The treatment of the intermediate NH_2 radical introduces some uncertainty. If NH_2 is assumed to be in steady state with no additional loss mechanisms, then:

$$n_{NH_2} = \frac{K_{32}}{K_{21}} n_{NH_3} \qquad (3.4)$$

which gives the following ratio of NH to H production:

$$\frac{n_{\mathrm{NH}}}{n_H} = \frac{K_{31}+K_{32}}{2K_{32}} \qquad (3.5)$$

Alternatively, if NH_2 undergoes complete loss, the ratio reduces to:

$$\frac{n_{\mathrm{NH}}}{n_H} = \frac{K_{31}}{K_{32}} \qquad (3.6)$$

The calculated NH:H ratios in Figure 3.2 are based on the rate coefficients for NH_3 dissociation as a function of mean electron energy, a plasma parameter representing the average energy of electrons in the discharge. The terms “no loss” and “full loss” describe the assumed behaviour of the intermediate NH_2 radical: “no loss” assumes NH_2 remains in steady state with no additional removal, while “full loss” assumes NH_2 is completely removed before contributing to NH formation. These represent two limiting cases, with the actual plasma expected to exhibit behaviour somewhere between these extremes. The electron energy influences the rate coefficients of each dissociation pathway and

therefore the NH:H ratio, but the ratio changes only modestly across the 2 – 8 eV range, assuming a fixed loss rate, which is a typical range for low pressure ICP plasmas.

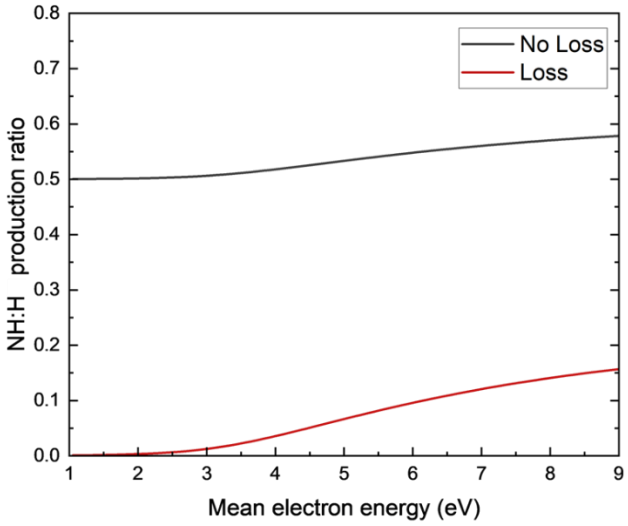


Figure 3.2 - NH:H production ratio vs mean electron energy, with no loss (black) and full loss (red) of NH_2 intermediate radical.

This analysis assumes fixed loss rates of the NH_2 intermediate radical over the investigated electron energy range. Under this assumption, variations in the observed NH:Hα emission ratio are unlikely to arise from changes in radical production rates. Instead, the ratio therefore reflects differences in excitation efficiency governed by the electron energy distribution. Accordingly, the NH:Hα ratio is used here as a diagnostic of plasma excitation behaviour, not as a direct measure of absolute radical densities.

3.3.1.3 OES NH:H-alpha emission ratio

Building on the theoretical analysis, the NH:Hα emission ratio was evaluated experimentally as an indicator of plasma excitation behaviour. The NH (336 nm)

emission has a lower excitation threshold (3.69 eV[14]) compared with the Hα line at 656 nm (12.09 eV[15]). As such, variations in the ratio provide an insight into the relative abundance of high-energy electrons capable of exciting atomic hydrogen compared with those sufficient to excite NH radicals.

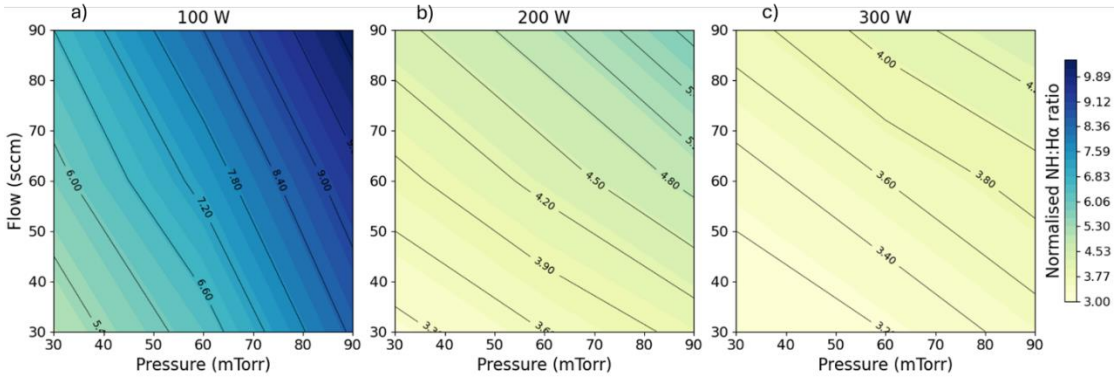


Figure 3.3 - NH:Hα ratio contour plot for feed-gas flow (sccm) vs chamber pressure (mTorr) for a) 100W, b) 200W and c) 300W ICP power.

Figure 3.3 summarises the measured ratios across the investigated plasma parameter space. Increasing ICP power led to a systematic decrease in the ratio, indicating a higher proportion of energetic electrons capable of reaching the 12.09 eV threshold for H excitation. At lower powers, NH emission dominates suggesting there are fewer high energy electrons.

In contrast, increasing both chamber pressure and NH_3 flow increased the NH:Hα ratio. Higher pressures reduce the electron mean free path, resulting in more frequent but lower-energy collisions, suppressing excitation of atomic hydrogen relative to NH. Similarly, higher NH_3 flow increases gas throughput, shortening residence times in the plasma source and reducing the probability of high-energy electron–molecule interactions, which preferentially suppresses H excitation.

These findings demonstrate that while atomic hydrogen excitation is sensitive to ICP power, it is also influenced by chamber pressure and gas flow, to a lesser extent. Based on these observations, a second optimised plasma condition was selected: 100 W ICP power, 90 mTorr chamber pressure, and 90 sccm NH_3 flow, corresponding to the highest NH:Hα ratio. Together with the NH-optimised and reference processes, this condition was carried forward for ALD processing with in-situ plasma diagnostics and a subsequent film growth study.

3.3.1.4 NH vs N_2 emission peak investigation

An additional investigation was carried out to confirm the reliability of the NH (336 nm) emission analysis, due to its proximity to the N_2 (337 nm) emission line. The limited resolution of the MayaPro spectrometer used for broad-range OES measurements could result in partial spectral overlap between these two peaks, potentially leading to overestimation of NH intensity. To investigate this, high-resolution spectra were acquired using an Ocean Optics Flame-T spectrometer for the parameter space.

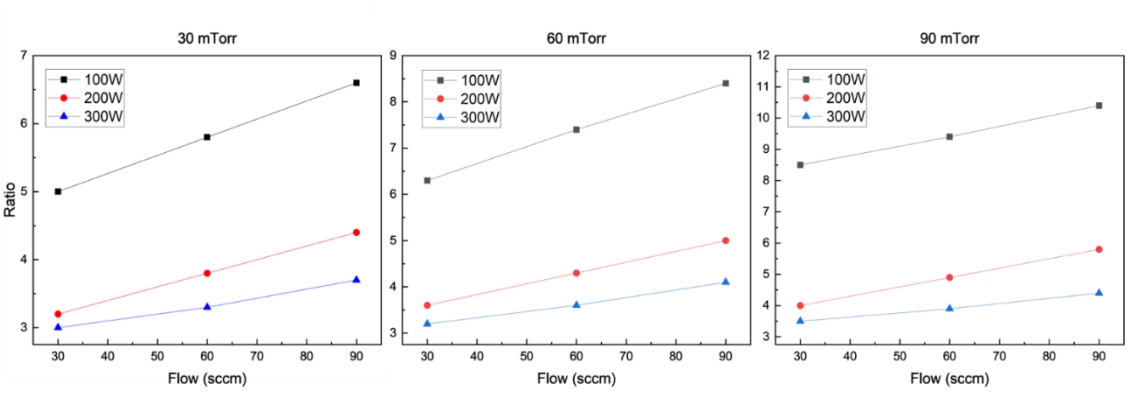


Figure 3.3 - NH:N_2 emission intensity ratio for ICP power vs feed gas flow for 30mTorr, 60 mTorr and 90 mTorr chamber pressure.

Figure 3.4 shows the plots of the NH:N_2, (336 nm:337 nm) emission ratio across the investigated plasma parameter space. In all conditions, the NH peak intensity was found to dominate over the N_2 emission with a minimum ratio of 3, confirming that the NH features observed in the MayaPro data reflect primarily NH rather than a convolution of NH and N_2. This validates the earlier NH emission analyses.

The high-resolution data also provide additional insight into the relative behaviour of NH and N_2 under varying plasma conditions. Increasing the ICP power led to a reduction in the ratio, likely due to the increased energy within the plasma allowing for the dissociation of NH_3 into atomic N followed by the recombination into N_2. At lower powers, there is less dissociation reducing the potential for N_2. Increasing the pressure resulted in the preferential reduction of the N_2 intensity. This supports the conclusion that decreasing the plasma's dissociation capability, due to quenching for pressure and reduced energy for the power, results in less ground state N_2 which is confirmed by the decreased emission intensity. Increasing the flow also resulted in an increase in the ratio. The shorter residence time of species in the source, with increased flow, reduces the possibility N_2 formation which reduces the overall emission intensity.

These findings suggest that the NH:N_2 ratio may serve as a useful plasma diagnostic for tuning nitrogen incorporation pathways in PE-ALD films. Low-flow plasmas that yield a reduced NH:N_2 ratio could favour N_2 incorporation, whereas high-flow plasmas promote NH radical. The impact of this behaviour on film composition is further investigated in Section 3.3 (Film Characterisation).

3.3.1.5 Selection of Plasma Conditions for PE-ALD

Based on the pre-ALD analysis, five representative plasma conditions (see Table 3.1) were selected for further investigation during PE-ALD deposition. These parameter sets capture a range of plasma behaviours observed in the pre-ALD diagnostics and provide a basis for evaluating plasma dynamics under PE-ALD conditions and their impact on film properties.

Table 3.1 - Experimental PE-ALD process plasma parameters.

Process	Power (W)	Pressure (mTorr)	Flow (sccm)
1 – Reference	100	30	60
2 - Optimised NH	300	30	90
3 - Max NH:H-alpha ratio	100	90	90
4 - Low flow	300	30	30
5 - High Pressure	300	90	30

3.3.2 In-situ Plasma diagnostics during PE-ALD process

Having identified five plasma conditions from the pre-ALD analysis (Table 3.1), these parameter sets were next applied during PE-ALD. Depositions consisted of 15 ALD cycles on cleaned, pre-treated Si substrates. In-situ OES measurements were acquired during a single plasma step for each condition. Plasma stability across the full cycle sequence was not investigated in this chapter but is addressed in future chapters. For the present study, all cycles for a given parameter set were assumed to be identical.

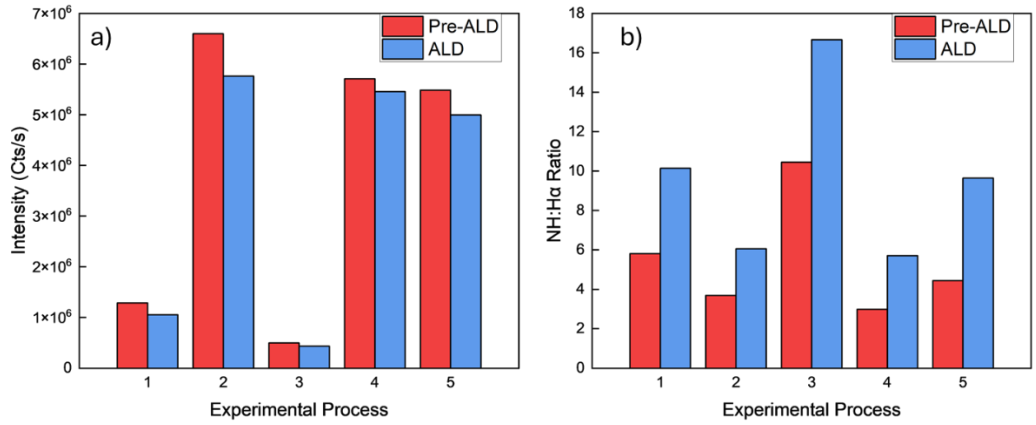


Figure 3.4 - Bar charts) for a) NH emission and b) NH:Hα ratio for pre-ALD (red) and ALD (blue) processes with experimental process number from Table 3.1.

The NH emission intensities varied significantly between processes, with the lowest values observed under low-power conditions (processes 1 and 3) and the highest under high-power conditions (processes 2, 4, and 5). Increasing chamber pressure from 30 mTorr (process 2) to 90 mTorr (process 5) reduced NH intensity, consistent with more frequent collisional cooling, while reducing NH_3 flow from 90 sccm (process 2) to 30 sccm (process 4) also lowered the intensity due to reduced precursor availability.

Overall, the in-situ results followed the same relative trends, as seen in Figure 3.5, as the pre-ALD plasma measurements. However, the absolute NH emission intensities were lower across all processes during PE-ALD, with an average decrease of 10% as seen in Figure 3.5 a),

The NH:Hα ratios also maintained the same relative trends as in the pre-ALD measurements. However, a significant increase in the absolute ratio was observed for all processes during deposition. The largest change was seen in the high-pressure condition

(process 5), where the ratio increased by 120%. This effect resulted primarily from a strong reduction in Hα emission, while NH emission decreased less significantly.

In summary, the in-situ plasma measurements show that while the relative behaviour of NH intensity and NH:Hα ratio with respect to plasma parameters remains consistent with the pre-ALD results, the absolute values are strongly modified under deposition conditions. All processes exhibited reduced NH intensity and suppressed Hα emission, leading to elevated NH:Hα ratios. The implications of these changes, and their origin in plasma–ALD environment interactions, are addressed in the discussion section (Section 4.1).

3.3.3 Film Characterisation

After deposition, all samples were transferred under vacuum to the integrated XPS chamber to minimise surface contamination. Survey scans were used to determine elemental composition, while film thicknesses were estimated from Si 2p attenuation as described in Chapter 2. At the beginning of this work, a series of films were deposited using the reference PE-ALD process to investigate film reproducibility. XPS analysis of these films revealed a high degree of reproducibility in their overall surface compositions, with the standard deviation of each measured element remaining below 0.5%, as shown in Figure 3.6. Peak fitting of the corresponding high-resolution spectra also demonstrated consistent bonding within the films. The fitting methodology applied is described in detail in the “Benchmark XPS Analysis” section below. These results confirm the expected reproducibility of the PE-ALD process under the consistent chamber conditions.

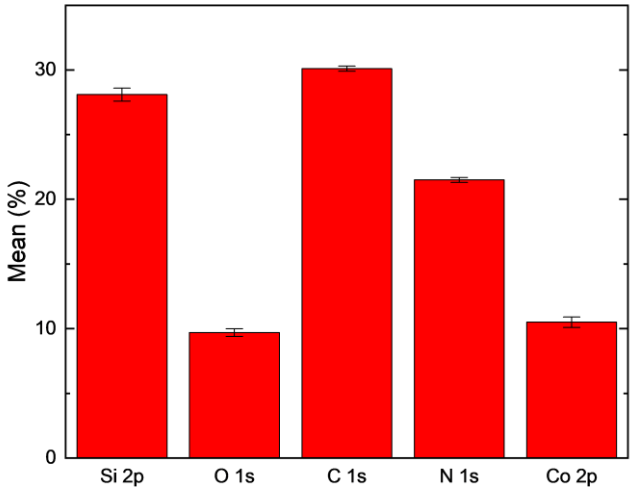


Figure 3.5 - Mean XPS survey composition of initial PE-ALD reference process with standard deviation represented by error bars.

Following the completion of this reproducibility study, the deposition system underwent an upgrade to the pumping configuration and modifications to the ICP source. These improvements altered the chamber performance, including the base pressure, gas flow dynamics and plasma characteristics. Therefore, the pre-ALD plasma investigation was performed after these system upgrades, and all subsequent Co PE-ALD experiments were also carried out under the new modified conditions.

Due to the changes in the vacuum and plasma environments, the film properties of the reference PE-ALD process differed between the pre-upgrade and post-upgrade conditions. However, film reproducibility had already been established during the initial study. In addition, the later experiments were conducted under stable, unchanged post-upgrade conditions. For these reasons, the reproducibility of the Co PE-ALD films was assumed to remain consistent during the subsequent investigations.

After the pre-ALD study, the five selected PE-ALD processes were performed. Table 3.2 summarises the elemental compositions and thicknesses for the five plasma processes.

Table 3.2 - PE-ALD process XPS elemental composition (%) and film thickness (nm).

Process	Si2p (%)	O1s (%)	C1s (%)	N1s (%)	Co2p (%)	Thickness (nm)
1 – Reference	45.4	17.2	17.0	12.1	8.3	1.3 ± 0.1
2 - Optimised NH	39.2	13.1	18.1	16.3	13.2	1.7 ± 0.2
3 - Max NH:Hα	67.5	24.9	4.3	1.9	1.5	0.2
4 - Low flow	32.9	11.1	22.2	21.9	12.0	2.2 ± 0.2
5 - High Pressure	57.7	21.3	11.8	4.7	4.5	0.6 ± 0.1

While atomic percentages are reported and discussed throughout this work, they should primarily be interpreted in terms of relative compositional changes between samples. Such comparisons provide the most reliable insight for ultrathin films analysed by XPS, where absolute values may be influenced by substrate contributions and the simplified quantification approach described in more detail in Section 2.3.2.3. Significant variation in both film thickness and composition was observed across the processes, demonstrating the strong influence of plasma parameters on film growth. Cobalt incorporation ranged from as little as 1.5 at.% (process 3) to more than 13 at.% (process 2), while nitrogen varied from 1.9 at.% to nearly 22 at.%. The Co:N ratio also varies significantly between processes. Processes 2 and 4 exhibit ratios approaching unity, consistent with plasma conditions that favour NH radical generation and efficient ligand removal, resulting in greater incorporation of both Co and N. In contrast, processes 3 and 5 show much lower nitrogen relative to cobalt. These conditions correspond to suppressed film growth and extremely thin films, where reduced radical flux and increased substrate signal contribute to the apparent decrease in nitrogen incorporation. Film thicknesses spanned more than an order of magnitude, from 0.2 nm (process 3) to 2.2 nm (process 4).

Processes 2 (optimised NH intensity) and 4 (low flow variation) yielded the thickest films with the highest Co and N contents, consistent with improved ligand removal and film growth. In contrast, processes 3 (max NH:Hα ratio) and 5 (high pressure variation) produced very thin films with low metal and nitrogen content, dominated by substrate signals (Si, O). Carbon remained present in all films, typically 12–22 at.%, reflecting incomplete removal of Cp ligands.

The survey spectra indicate that plasma conditions exert a major influence on PE-ALD film growth. The optimised NH and low-flow processes promoted thicker, more Co–N rich films, whereas high pressure and high NH:Hα ratio suppressed deposition. These trends motivated detailed high-resolution XPS analysis of the reference process film for use as a benchmark, presented in the following section.

3.3.3.1 Benchmark XPS analysis

It should be noted that pre-ALD plasma treatment resulted in the complete removal of C 1s peaks, as such the resulting post-deposition C 1s is directly related to unremoved precursor ligands. The reference process (1) was analysed in detail as a benchmark for comparison. High-resolution XPS spectra of the O 1s, C 1s, N 1s and Co 2p regions are shown in Figures 3.7 and Figure 3.8. The same fitting methodology was applied to all films.

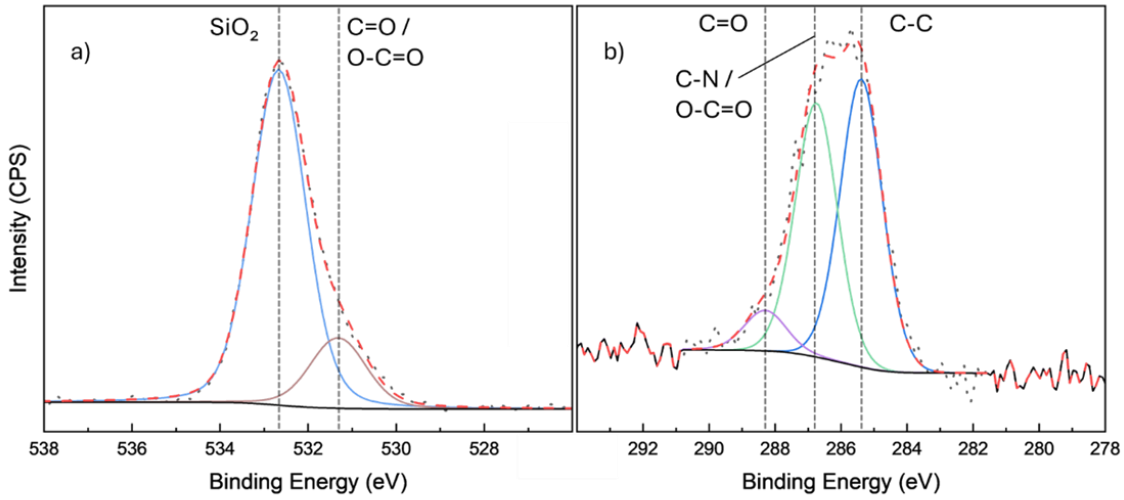


Figure 3.7 - Fitted a) O 1s and b) C 1s high resolution XPS peaks for the reference process.

In Figure 3.7 (a), the O 1s region was fitted with two clear peaks at 531.4 eV and 532.7 eV, which correspond to carbon-oxygen and SiO_2 bonding, respectively. The relative peak areas were 83.5 ± 0.8 % for SiO_2 and 16.5 ±0.8 % for carbon-oxygen. The 531.4 eV peak contribution is attributed to the initial precursor bonding to the active surface sites on the native SiO_2 overlayer, followed by incomplete removal of precursor ligands resulting in the carbon presence. 531.5 is attributed to aromatic C=O bonding, which suggests unremoved Cp ligands, and O-C=O, suggesting fragmentation of the Cp ligand. To further investigate this oxygen peak, the carbon-oxygen bonding in the C 1s was examined, Figure 3.7 (b). The C 1s envelope contained three peaks located at 285.2 eV, 286.7 eV and 288.1 eV. The 285.2 eV feature corresponds to C–C bonding, attributed entirely to the precursor ligands. The 288.1 eV feature is assigned to C=O bonding, while the 286.7 eV peak is associated with a mixture of C–N bonding and O–C=O bonding.

For this film, both the C at % and O at % contributions to the overall survey composition were approximately 17 %. From the O 1s, 531.4 eV peak contributed 16.5 ± 0.8 % to the

overall fit. It can be assumed that a similar fraction is also oxygen bonded in the C 1s. In the C 1s fit the 288.1 eV peak contributed 6.6 ± 0.9 % leaving approximately 10 % still attributable to oxygen bonding within the 286.7 eV feature. The 286.7 eV peak contributed to 44.4 ± 2.3 %, suggesting approximately 34.4 ± 2.3% is attributable to C-N bonding. The overall C 1s composition is thus 49 ±2.3, 34.4 ± 2.3% C-N and 17 % carbon-oxygen bonding, which is consistent with the O 1s fitting.

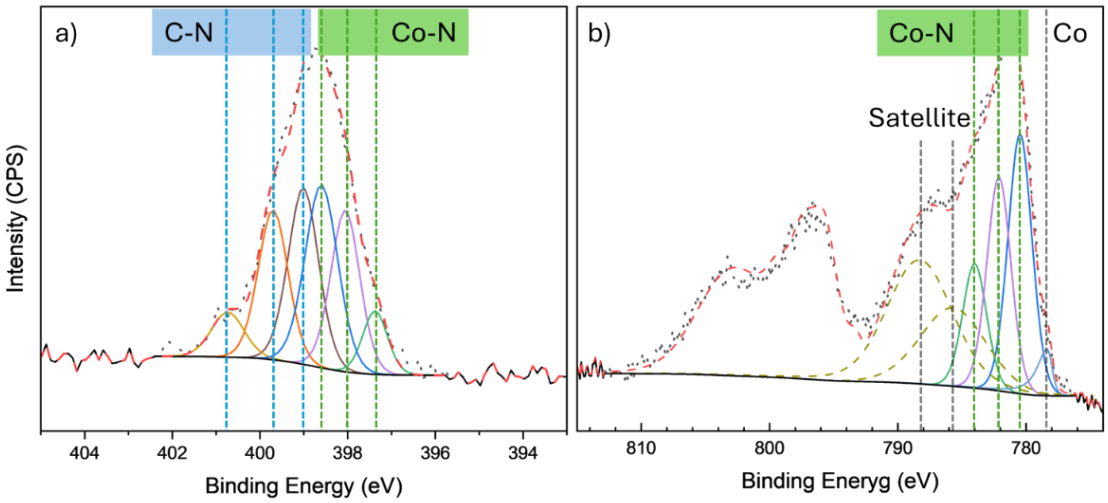


Figure 3.8 - Fitted a) N 1s and b) Co $2p_{3/2}$ high resolution XPS peaks for the reference process.

In Figure 3.8 (a), the N 1s spectrum was fitted with peaks at 397.4 eV, 398.0 eV, 398.5 eV, 399.0 eV, 399.7 eV and 400.8 eV. These were assigned to Co-rich CoN, stoichiometric CoN, N-rich CoN, pyridinic nitrogen, pyrrolic nitrogen and protonated or graphitic nitrogen, respectively[10,16–18].

Of these, only the peaks at 399.0 eV and above contribute to carbon–nitrogen bonding, giving a combined contribution of approximately 48% of the N 1s envelope, while the remaining 52% corresponds to CoN bonding. Since the N 1s region accounts for 12 % of

the overall survey composition, this translates to ~5.7% attributed to carbon–nitrogen bonding and ~6.2% attributed to Co–N bonding within the film. Comparison with the C 1s region, in which 34.4 % of the envelope corresponds to C–N bonding yielded 5.8 % of the survey composition. The excellent agreement of C-N bonding between the C 1s (5.8%) and N 1s (5.7%) analyses, differing by only 0.1%, demonstrates the reliability of the O 1s, C 1s and N 1s fittings.

Following the same method, the Co–N contribution from the N 1s analysis was quantified as 6.2% of the survey composition. The Co $2p_{3/2}$ region was fitted with components at 778.2 eV, 780.5 eV, 782.1 eV and 784.0 eV, together with shake-up satellites at 786 eV and 788 eV. The 778.2 eV feature corresponds to metallic Co, while the 780.5–784.0 eV peaks represent Co-rich CoN, stoichiometric CoN and N-rich CoN environments, respectively[10]. The satellite peaks are characteristic of Co^{2+} effects[19]. Quantification of the Co–N fraction, including the satellite contributions, gave 8.0% of the total Co 2p signal (8.2% of the survey composition), compared with 6.2% from the N 1s analysis. This slight (1.8%) difference is attributed to the greater complexity and uncertainty of Co $2p_{3/2}$ fitting, particularly due to multiplet splitting and satellite features, whereas the N 1s region provides a more direct measure of nitrogen bonding environments. Overall, both analyses confirm that cobalt is incorporated predominantly in nitride bonding states.

In summary, detailed XPS analysis of the reference film confirmed the presence of carbon residues from incomplete ligand removal, a significant fraction of C–N bonding consistent across both the C 1s and N 1s regions, and Co–N bonding confirmed independently by the N 1s and Co 2p spectra. The good agreement between the different core levels demonstrates the reliability of the fitting methodology, which was subsequently applied to the other films. Having established this benchmark, the following

section compares the reference process with the optimised NH plasma process to evaluate the influence of process conditions on film composition and bonding environments.

3.3.3.2 Reference process compared to NH optimised process

To assess the impact of plasma optimisation, the film deposited under the reference condition (process 1) was compared with the optimised NH process (process 2). Table 3.1 shows the survey results, while Figure 3.9 presents the high-resolution Co 2p, N 1s and C 1s spectra of the two films. The same peak-fitting methodology described for the reference process was applied to the optimised NH film to ensure consistency.

The optimised process (a) produced a thicker film (1.7 ± 0.2 nm vs. 1.3 ± 0.1nm) with higher Co (13.2 vs. 8.5 at.%) and N (16.3 vs. 12.0 at.%) contents. The C 1s fraction was similar in both cases (~18%). However, the optimised NH film had an increased thickness which reduces the overall carbon density within the film. A simple Co 2p:C 1s ratio improved from 0.47 (reference) to 0.73 (optimised NH), reflecting more efficient precursor ligand removal and improved film composition.

Both films contained a mixture of metallic Co and Co–N bonded states. The optimised film exhibited a higher overall Co intensity, but also a stronger metallic Co (778.4 eV) contribution compared with the reference, as seen in Figure 3.9. The relative proportions of Co-rich and stoichiometric CoN were similar in both cases, with N-rich environments contributing the least.

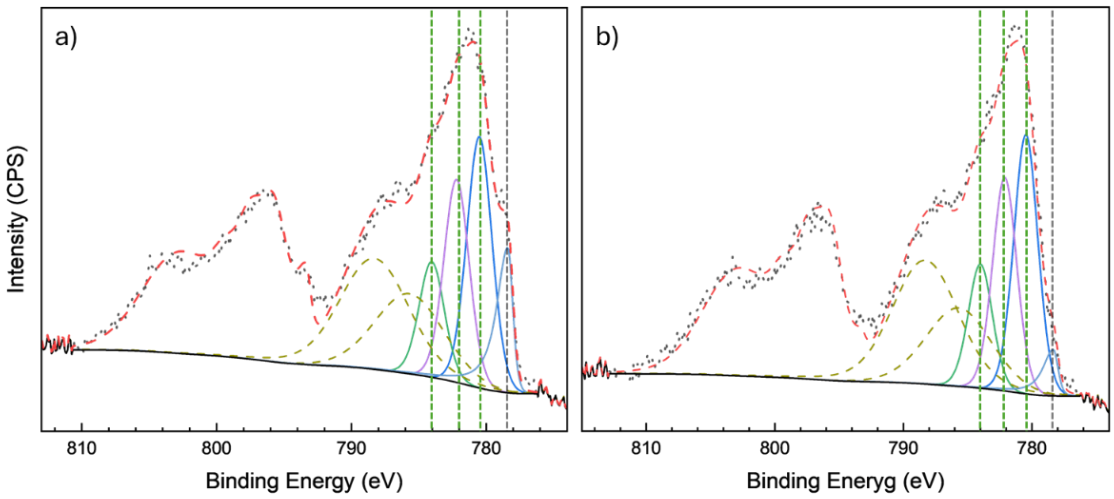


Figure 3.9 - Fitted Co $2p_{3/2}$ peaks for a) Optimised NH process and b) reference process.

The N 1s spectra of both films were consistent with the Co 2p analysis, showing comparable fractions of Co-rich and stoichiometric CoN. The main difference was the higher total N content in the optimised NH film, consistent with its greater thickness and higher overall Co incorporation.

The C 1s region was also similar in both cases, with dominant C–C bonding at ~285 eV, a secondary C–N contribution at ~287 eV, and a weaker C=O component at ~289.5 eV[20]. The optimised film showed a slight decrease in the relative C–C fraction and a corresponding increase in C–N bonding compared with the reference, suggesting a greater degree of carbon incorporation in bonded environments with a decrease in unreacted ligands.

In summary, the optimised NH process produced a thicker film with higher Co and N contents and an improved Co 2p:C 1s ratio compared with the reference. Both films displayed similar Co–N bonding distributions, though the optimised NH case contained a larger metallic Co component. Carbon residues remained present in both films,

indicating that precursor ligand removal was still incomplete despite the plasma optimisation.

3.3.3.3 Max NH:Hα process

To investigate the effect of maximising the NH:Hα ratio, the film deposited under these conditions (process 3) was compared with the reference process (process 1). Figure 3.10 shows the survey spectra of the two films which were both deposited at 100 W ICP power.

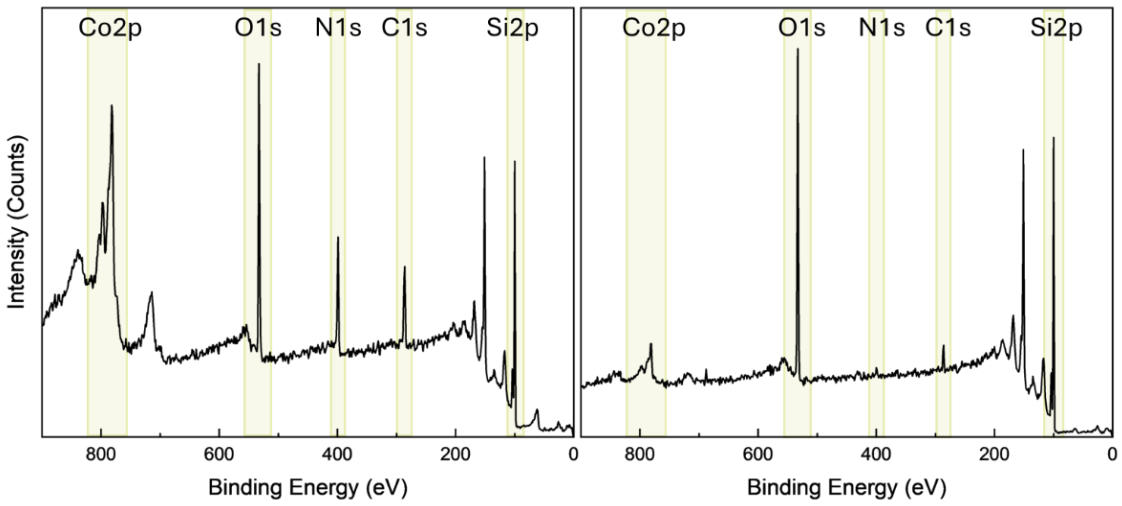


Figure 3.10 - Survey XPS of the reference process (left) and the max NH:Ha ratio process (right), with regions of interest highlighted, both processes had a plasma power of 100 W.

The NH:Hα-optimised process produced negligible film growth, with only weak Co and N signals compared to the reference. This result indicates that maximising the NH:Hα ratio alone does not promote deposition, and in this case strongly suppressed growth.

Plasma emission data for the two processes are compared in Figure 3.5. Although process 3 achieved the maximum NH:Hα ratio, the absolute NH intensity was significantly lower

than in the reference plasma. This corresponds directly with the poor film growth observed, suggesting that absolute NH emission, rather than the relative excitation ratio, is a potential critical factor in sustaining deposition.

However, a key process difference was the operating pressure. The max NH:Hα film was deposited at 90 mTorr, three times higher than the reference. This points to increased pressure as a potential cause of the reduced film growth. The effect of pressure on growth was therefore investigated further with the optimised NH process and a high-pressure variant.

3.3.3.4 Variation of pressure

To evaluate the influence of pressure directly, a high-pressure variant of the NH process (process 5: 300 W, 90 mTorr, 90 sccm) was compared with the optimised NH condition (process 2: 300 W, 30 mTorr, 90 sccm). The survey spectrum, from Figure 3.11, shows that the high-pressure process produced a significantly thinner film (0.6 ± 0.1 nm vs 1.7 ± 0.2 nm) with reduced Co (4.5 at.% vs 13.2 at.%) and N (4.7 at.% vs 16.3 at.%) contents. At the same time, the C 1s decreased to 11.8 at.% compared with 18.1 at.% for the optimised NH film. The decrease in C 1s is attributed to the significantly decreased film thickness. A simple C 1s to thickness ratio provides further information on the relative C 1s contribution per nm in which the optimised NH film is 10.6 % per nm while the higher-pressure film had 19.6 % per nm.

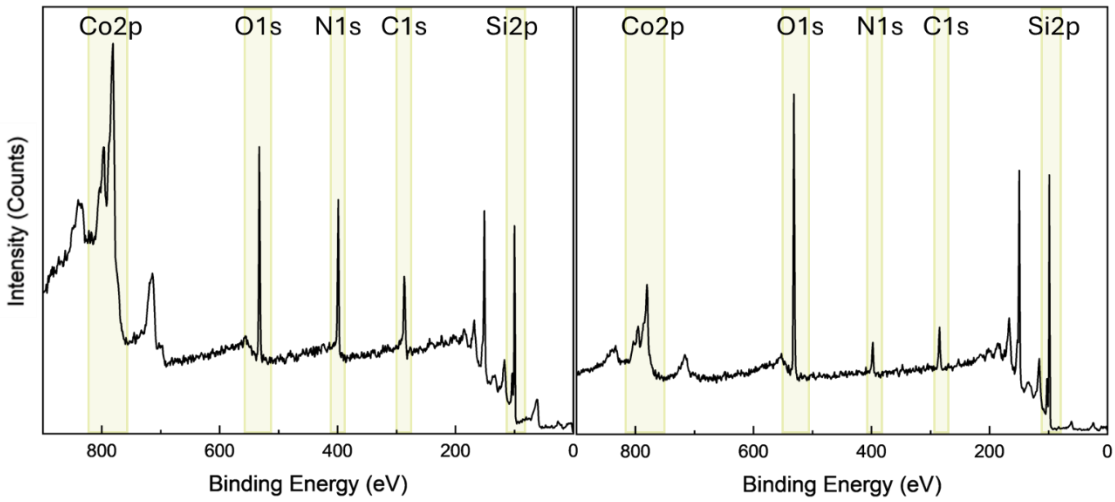


Figure 3.11 - Survey XPS of the Optimised NH process (left) and the high pressure process (right), with regions of interest highlighted.

The high-resolution C 1s spectra (Figure 3.12) reveal a difference in the relative contributions of C–C and C–N peaks. In the high-pressure variant, the proportion of C–C bonding increases significantly to 67.2 ± 4 % of the total C 1s signal, compared with 49 ± 2.3% for the optimised NH process. Conversely, the contribution from 286.7 eV bonding decreases from 44.4 ± 2.3 % in the optimised NH process to 27.1 ± 3.5% under higher pressure. This trend indicates that increasing the pressure suppresses surface reactions. In a remote source configuration, elevated pressure increases the likelihood of collisions in the gas phase before the reactive species reach the substrate, reducing their reactivity at the surface. As a result, a higher proportion of unreacted precursor ligands remain in the film, leading to a relative increase in C–C bonding and a decrease in C–N bond formation

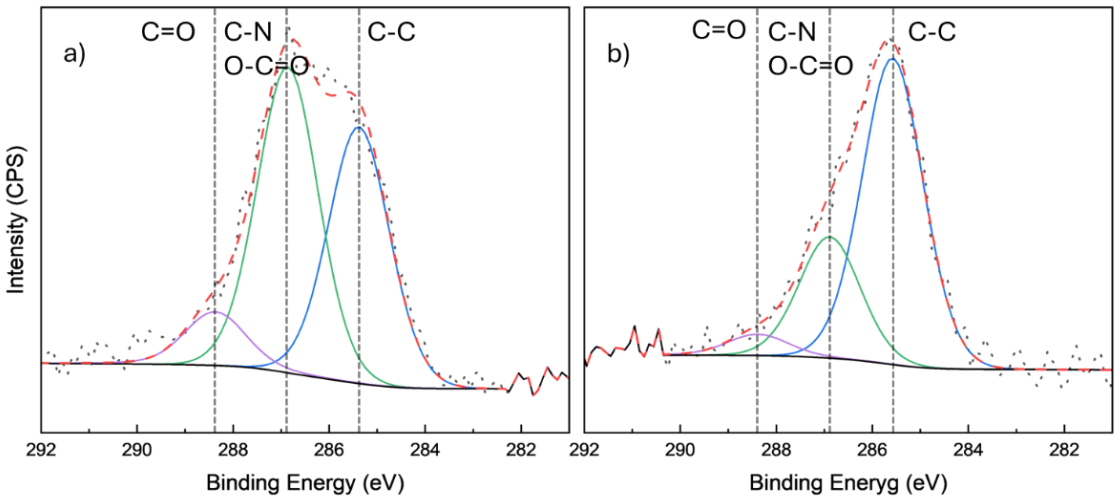


Figure 3.12 - C 1s fitted peaks for a) Optimised NH process and b) high pressure process.

3.3.3.5 Variation of flow

Next, the impact of feed-gas flow was investigated using a low flow variation (300W, 30sccm, 30mTorr) of the optimised NH process (300W, 90sccm, 30mTorr). From Table 3.2, the low-flow condition yielded the thickest film of all processes (2.2 ± 0.2 nm), with Co, N and C contents of 12.0 at.%, 21.9 at.% and 22.2 at. %, respectively. While the optimised NH process had Co, N and C contents of 13.2 at.%, 16.3 at.% and 18.1 at %.

The high-resolution Co 2p spectra for the two processes (Figure 3.13) show Co–N peaks, with comparable distributions of Co-rich, stoichiometric, and N-rich CoN environments. The metallic Co contributions of the low flow process were minor compared with the optimised process, suggesting that the lower flow condition produced a more stable Co–N phase.

Fitting of the C 1s showed near identical contribution for the two processes. A slight increase of the C-N bonding with a similar reduction in the C-C bonding was identified for the low flow process. The carbonate contribution of this peak was found to be the same for both processes. Due to the minor change in the fitted peaks the overall increased

C 1s contribution of the low flow process is due to the increased film thickness. The two processes also had almost identical N 1s contribution which suggests that the increased N 1s content is also a result of the thicker film.

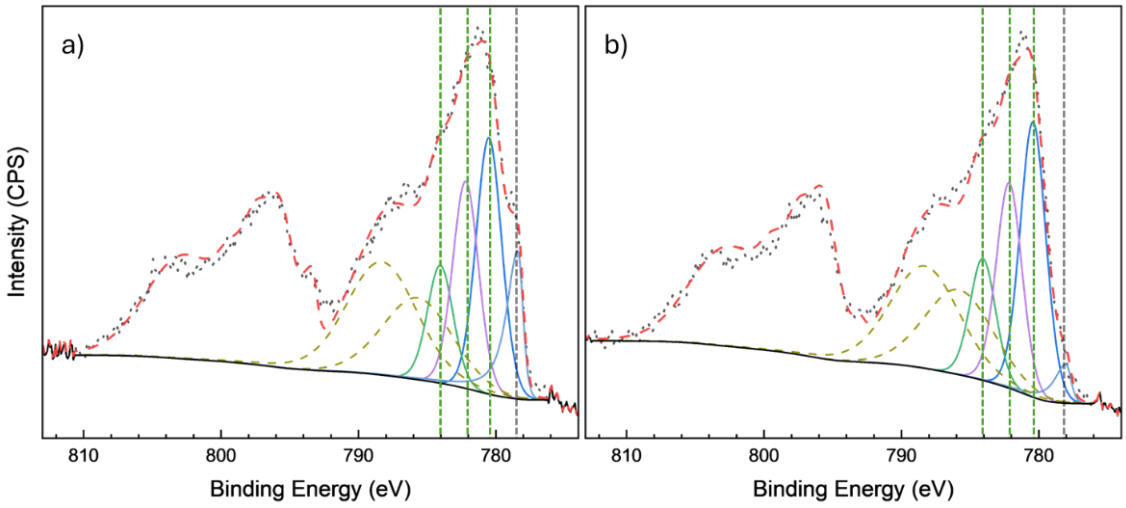


Figure 3.13 - Fitted high resolution Co $2p_{3/2}$ peaks for a) Optimised NH process and b) low flow process.

Overall, reducing NH_3 flow appears to enhance growth per cycle while reducing the cobalt but increasing the nitrogen incorporation. The C 1s content per nm of film thickness remains the same between the two processes at approximately 10 at % per nm.

3.3.3.6 Summary

The XPS analysis across the five selected plasma conditions shows that plasma parameters strongly impact both film thickness and composition. The optimised NH process produced improved Co and N incorporation compared with the reference. The max NH:Hα ratio process failed to produce meaningful growth, highlighting the

importance of the NH emission intensity measurement. High pressure strongly suppressed deposition and increased carbon incorporation but had the most stoichiometric film, while low NH_3 flow yielded the best overall film growth with increased nitrogen incorporation.

These results establish clear links between plasma conditions and film properties, providing a foundation for the subsequent discussion, where the influence of the parameters on the process plasma, the impact of the ALD environment on the plasma behaviour, the influence of the parameters on the film properties and the correlation between plasma features and film properties are addressed in detail.

3.4 Discussion

3.4.1 Influence of controllable parameters on process plasma

From the pre-ALD study, there was clear evidence that the selected parameters shape the plasma's response, allowing for control of its properties. From the radical production analysis using the cross sectional data from Snoeckx et al[13] it was found that across the relevant electron energies, the production of hydrogen atoms is consistently higher than NH radicals, with slight variation over the range. This result demonstrates that variation in the observed emission ratios is not attributed to significant changes in radical production rates. Instead, the ratio primarily reflects differences in excitation behaviour governed by the EEDF. The emission threshold energies of NH (~3.7eV) and Hα (~12.1eV), as previously mentioned, provide insight into the low and high energies electrons of the EEDF via the NH:Hα ratio.

At increased ICP power, the resulting EEDF has an increase in high-energy electrons, which enhanced the Hα excitation and reduces the NH:Hα ratio. Previous studies of low pressure ICP have demonstrated increasing power reduces the mean electron energy but significantly enhanced the overall population of electron density across the EEDF, including the high-energy tail[21,22]. The increased high-energy electrons along with the overall higher production of atomic hydrogen reduces the NH:Hα ratio with increasing power. The increased overall electron density was observed by the general increase in the NH intensity, which is a response of the increased dissociation and excitation due to the higher density.

Increasing chamber pressure was seen to reduce the overall NH and Hα emission intensities while increasing the NH:Hα ratio. Boffard et al[23] showed that in a low-pressure ICP, rising pressure reduces the population of high-energy electrons due to collisional

energy losses. This depletion of energetic electrons lowers the dissociation and excitation rates responsible for both NH and Hα emission. However, because Hα emission requires higher-energy electrons for excitation of atomic hydrogen, it decreases more rapidly with pressure than NH emission. Consequently, the NH:Hα ratio increases even though the absolute intensity of both species declines.

Finally, Tong et al[24] has demonstrated in low-pressure Ar/ N_2 ICPs, that increases in feed-gas flow moderately increases electron density over the 5-50 sccm range. From the measured OES data, it was found that higher flow rates increased both the NH and the NH:Hα ratio, with more significant increases at higher powers. These trends are consistent with the reported increase in electron density at higher flow rates, as a larger electron population increases the probability of collisional excitation.

These finding confirm that both the identified plasma diagnostics features, namely NH and NH:Hα ratio, provide insight into the plasma's behaviour, which follow previously established low pressure ICP trends. The parameters can therefore be tuned to obtain a plasma with desirable behaviour for the selected PE-ALD process.

3.4.2 Impact of the ALD environment on plasma behaviour

When comparing the pre-ALD and the in-situ process monitoring OES spectra, a clear change in the emission was observed. The relative behaviour of the NH intensity and NH:Hα ratios with respect to the process parameters was preserved. However, the absolute emission intensities were strongly altered once the plasma was introduced to the ALD environment. While all emission peaks were reduced in intensity, the Hα was significantly more suppressed, leading to an increased NH:Hα ratio under all conditions.

No prior work directly measuring the suppression of high-energy electrons in ALD environments has been reported. However, several studies have reported changes or reductions in optical emission spectroscopy (OES) peaks during PE-ALD processes, attributing these effects to plasma contamination or precursor–plasma interactions. For example, Heil et al[25] observed that reaction by-products released during ALD cycles altered the emission characteristics of normal plasma operation. Emission intensities were attenuated in the presence of the ALD environment, consistent with the impact observed in this work. Similarly, Mione et al[26] found that excited O species were consumed during the ALD process, indicating that the ALD environment significantly affects plasma composition. Boris et al[27] also noted that precursor dosing can distort OES measurements, further demonstrating the strong influence of the ALD environment on the process plasma.

From the above discussion, and considering the factors influencing plasma emission, the observed suppression is due to an increased concentration of collisional quenching partners (precursors, fragments, and reaction by-products). The disproportionate impact on the Hα emission results from quenching of high-energy electrons due to a reduced mean free path, an effect that has been identified in previous work.

Overall, these findings demonstrate that the NH:Hα ratio and Hα are modified by the ALD environment. The disproportionate suppression of Hα emission highlights the sensitivity of high-energy electron-driven processes to precursor–plasma interactions, a factor that must be considered when interpreting OES diagnostics in PE-ALD systems.

3.4.3 Influence of plasma parameters on film properties

Film thickness and composition varied by more than an order of magnitude across the investigated parameter set, highlighting the strong sensitivity of PE-ALD to plasma behaviour. The trends observed in $CoCp_2$ & NH_3 PE-ALD have been split into the parameters impact on the process.

Increasing ICP power enhanced Co and N incorporation and yielded thicker films. This behaviour is consistent with the role of plasma power in increasing electron density and driving more efficient NH_3 dissociation, thereby raising the density of reactive NH radicals. Vos et al.[11] identified NH radicals as the key species responsible for Cp ligand elimination during Co ALD, demonstrating their direct role in enabling ligand removal. Zhang et al[28] investigated the impact of power variation on PE-ALD produced AlN. Increases in both the growth per cycle and density were observed. Additionally, the oxygen content dropped and both the Al and N content increased with higher power. Yoon et al[29] varied power while depositing TiO_2 films via PE-ALD. A constant GPC was maintained over all powers, but it was concluded that the high power resulted in films with improved density and etch resistance due to enhanced reactivity of the plasma oxygen species with the Ti atoms. The published work indicates that increasing plasma power enhances film quality, though the GPC is more material dependent. O radical typically have lower recombination probability ($10^{-4} - 10^{-2}$) when compared to nitrides or metals (0.03-0.3) resulting in less sensitive GPC with increased radical density due to higher power[30]. The trends observed here align with these reports, showing that higher power promotes both film growth and increased incorporation of nitrogen and Co.

Increasing chamber pressure suppressed film growth and increased the relative carbon content of the films. Li et al.[31] reported that higher process pressure improved film properties in thermal ALD of Al_2O_3. Although their system did not employ a remote

plasma source, their results suggest that increased gas density at higher pressure can enhance precursor surface saturation and promote more uniform growth. In contrast, Faraz et al.[32] demonstrated that in remote plasma systems, similar to the setup used in this work, raising the pressure drastically reduces ion flux and energy due to enhanced collisions and radical recombination. This leads to a lower concentration of reactive species reaching the substrate, consistent with the observed reduction in growth rate and increased carbon incorporation in our films.

Lowering the feed-gas flow resulted in an increased GPC and higher nitrogen incorporation. However, similar levels of carbon incorporation were observed under both low and high flow conditions. High-resolution OES measurements indicated that lower flow rates led to enhanced N_2 excitation, as evidenced by an increased NH:N_2 emission ratio. The longer residence time of the gas within the source at reduced flow rates likely increases the probability of nitrogen species generation, which in turn promotes N–N recombination and results in stronger N_2 emission. This enhanced nitrogen activity can lead to greater nitrogen incorporation into the film, consistent with the observed higher nitrogen concentrations. Profijt et al[33] reported that changes in plasma feed-gas flow modify the plasma conditions by altering the residence time of reactive species. Increased residence time at lower flow rates can enhance radical generation, leading to a higher radical density reaching the substrate. This elevated radical flux has been identified as a key factor influencing growth per cycle and overall film deposition behaviour in plasma-assisted ALD processes.

Overall, these results show that plasma parameters shape both radical generation and their subsequent transport and recombination, producing trends consistent with those reported previously. These parameters directly influence film growth, leading to variations in both

thickness and composition, which motivates the following discussion on how plasma features correlate with the resulting film properties.

3.4.3 Correlation of plasma features with film properties

Several functional forms, namely linear, logarithmic, exponential and power-law models, were evaluated to assess correlations between the selected plasma features and film properties. A minimum threshold of $R^2 \geq 0.7$ was used as the criterion for acceptance, corresponding to an association that explains at least 70% of the variance and is classified as 'very strong' correlation according to Hair[34]. Parameter uncertainties were extracted from the covariance matrix of the regression model and represent the 1σ confidence interval for each fitted coefficient. Small uncertainties indicate a well constrained parameter, while large uncertainties indicate weak parameter stability. Model accuracy was assessed using the root mean square error (RMSE), which quantifies the average residual deviation between the fitted model and the measured data. Lower RMSE values correspond to a closer match between the model and the observations.

The investigated plasma features were the NH intensity and the NH:Hα ratio, while the examined film properties included the Co 2p content, film thickness, and the Co 2p:C 1s ratio. No significant correlations were identified between NH intensity and any of the investigated film properties, with R^2 values between 0.35 and 0.45. This indicates that the absolute NH emission intensity alone does not directly reflect the plasma conditions that govern film growth. Although Vos et al[11] proposed that NH is a key reactive species for this PE-ALD process, the presented results imply that there are additional underlying factors which contribute to surface reactions. Consequently, a more comprehensive and quantitative plasma diagnostic approach is required to fully capture the relevant plasma chemistry and its impact on film growth.

While the absolute NH intensity showed no meaningful correlation with any of the film properties, the NH:Hα ratio displayed acceptable correlations with both the Co 2p content and film thickness, with all four investigated models exceeding the threshold of $R^2 \geq 0.70$. For each model, parameter stability was assessed using the relative uncertainty of the fitted coefficients. The relative uncertainties were averaged to obtain a single measure of overall model stability, and the model with the lowest mean relative uncertainty was considered the most statistically reliable.

For both film properties, the linear model provided the lowest mean relative uncertainties with 21% for Co 2p and 24% for film thickness. This indicates well-constrained parameters. The exponential and power-law models exhibited higher uncertainty values ranging from 36 % to 41%, while logarithmic models showed considerably poorer stability, with uncertainties ranging from 85 % to 149 %.

To further evaluate the linear fits, the RMSE was calculated on normalised data for comparison between fits, giving values of 0.14 for Co 2p and 0.15 for film thickness. These low RMSE values indicate small average deviations between the model predictions and the measured data. From these results it is demonstrated that the NH:Hα ratio provides a meaningful and quantitative correlation with these film properties.

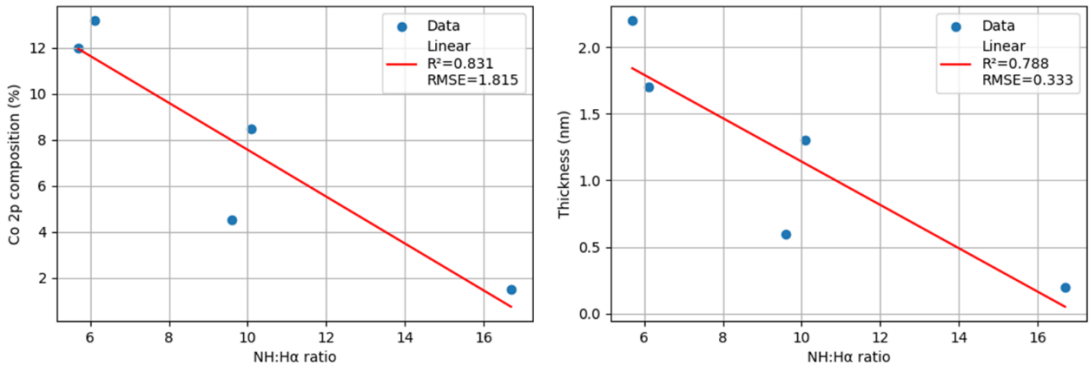


Figure 3.14 - Linear correlation between NH:Hα measurements and film properties ((a)Co 2p composition (%) and (b) film thickness (nm))

Physically, the NH:Hα ratio reflects the balance between low-energy and high-energy electron excitation channels in the plasma. A high NH:Hα ratio therefore indicates a plasma dominated by lower-energy excitations, which suppresses the generation of higher-energy electrons that are necessary to sustain efficient ligand removal and Co–N bond formation. This interpretation is consistent with the failure of the max NH:Hα process, where a high NH:Hα ratio was achieved, and film growth was negligible.

Overall, these findings show that while NH species have been identified as the primary reactive species for the investigated PE-ALD process, maximising the NH intensity alone does not produce significant correlations with the investigated film properties. However, the NH:Hα ratios provides a strong correlation with growth-related metrics such as Co incorporation and thickness.

3.5 Conclusion

This chapter has investigated optical emission spectroscopy (OES) as a plasma diagnostic for PE-ALD of cobalt nitride using $CoCp_2$ and NH_3 plasma. A pre-ALD parametric study identified several plasma conditions using NH emission intensity and the NH:Hα ratio as indicators, which were subsequently investigated in deposition processes.

In-situ OES revealed that the ALD environment modifies plasma behaviour through quenching of excited states, particularly higher-energy transitions such as Hα, while relative trends observed in the pre-ALD investigated were preserved. This demonstrates that pre-ALD diagnostics capture useful comparative behaviour, but accurate quantification during deposition requires in-situ monitoring.

Film characterisation confirmed that plasma parameters strongly affect growth, composition, and bonding. The NH-optimised process yielded the highest Co incorporation and improved growth per cycle compared to the reference condition. High-pressure and maximum NH:Hα processes suppressed growth, highlighting the importance of the role of reactive species transport. Low NH_3 flow produced the thickest films with enhanced nitrogen incorporation. An inverse linear relationship between the NH:Hα ratio and both the film's Co 2p composition percentage and its thickness was observed. However, no correlations were found between the absolute NH emission intensity and any of the investigated film properties in this experimental work.

While optical emission spectroscopy (OES) proved valuable for identifying relative plasma trends and correlating them with film outcomes, it also has inherent limitations. Emission intensities represent only the excited-state populations of species and therefore do not capture transport behaviour or provide more detailed information on the plasma. This limitation highlights the need for complementary plasma diagnostics. The following

chapter will establish a more quantitative understanding of the influence of the controllable parameters on the plasma behaviour by using a multi-diagnostics approach.

3.6 References

(1) Bhandari, H. B.; Yang, J.; Kim, H.; Lin, Y.; Gordon, R. G.; Wang, Q. M.; Lehn, J.-S. M.; Li, H.; Shenai, D. Chemical Vapor Deposition of Cobalt Nitride and Its Application as an Adhesion-Enhancing Layer for Advanced Copper Interconnects. *ECS J. Solid State Sci. Technol.* **2012**, *1* (5), N79–N84. https://doi.org/10.1149/2.005205jss.

(2) Im, Y. B.; Na, Y. S.; Lim, H. J.; Kim, D. U.; Seo, K. B.; Lee, S. C.; Choi, C. Chemical and Elecrtrical Charaterization of ALD Cobalt Nitride (CoN) as an Alternative Barrier for Advanced Cu Interconnects. In *2025 IEEE International Interconnect Technology Conference (IITC)*; IEEE: Busan, Korea, Republic of, 2025; pp 1–4. https://doi.org/10.1109/IITC66087.2025.11075438.

(3) Gall, D. The Search for the Most Conductive Metal for Narrow Interconnect Lines. *J. Appl. Phys.* **2020**, *127* (5), 050901. https://doi.org/10.1063/1.5133671.

(4) Moon, J. H.; Jeong, E.; Kim, S.; Kim, T.; Oh, E.; Lee, K.; Han, H.; Kim, Y. K. Materials Quest for Advanced Interconnect Metallization in Integrated Circuits. *Adv. Sci.* **2023**, *10* (23), 2207321. https://doi.org/10.1002/advs.202207321.

(5) Baklanov, M. R.; Adelmann, C.; Zhao, L.; De Gendt, S. Advanced Interconnects: Materials, Processing, and Reliability. *ECS J. Solid State Sci. Technol.* **2015**, *4* (1), Y1–Y4. https://doi.org/10.1149/2.0271501jss.

(6) Fan, Q.; Sang, L.; Jiang, D.; Yang, L.; Zhang, H.; Chen, Q.; Liu, Z. Plasma Enhanced Atomic Layer Deposition of Cobalt Nitride with Cobalt Amidinate. *J. Vac. Sci. Technol. Vac. Surf. Films* **2019**, *37* (1), 010904. https://doi.org/10.1116/1.5062842.

(7) Van Der Straten, O.; Zhang, X.; Motoyama, K.; Penny, C.; Maniscalco, J.; Knupp, S. ALD and PVD Tantalum Nitride Barrier Resistivity and Their Significance in via Resistance Trends. *ECS Trans.* **2014**, *64* (9), 117–122. https://doi.org/10.1149/06409.0117ecst.

(8) Luithardt, W.; Benndorf, C. Deposition of Fe-C:H Coatings from a Ferrocene Precursor in a Plasma-Activated r.f. Process. *Diam. Relat. Mater.* **1995**, *4* (4), 346–349. https://doi.org/10.1016/0925-9635(94)05240-9.

(9) Van Straaten, G.; Deckers, R.; Vos, M. F. J.; Kessels, W. M. M.; Creatore, M. Plasma-Enhanced Atomic Layer Deposition of Cobalt and Cobalt Nitride: What Controls the Incorporation of Nitrogen? *J. Phys. Chem. C* **2020**, *124* (40), 22046–22054. https://doi.org/10.1021/acs.jpcc.0c04223.

(10) O'Donnell, S.; Snelgrove, M.; Shiel, K.; Weiland, C.; Hughes, G.; Woicik, J.; O'Neill, D.; Jose, F.; McFeely, C.; O'Connor, R. Growth Chemistry of Cobalt Nitride by Plasma Enhanced Atomic Layer Deposition. *Mater. Res. Express* **2022**, *9* (10), 106402.

(11) Vos, M. F.; van Straaten, G.; Kessels, W. E.; Mackus, A. J. Atomic Layer Deposition of Cobalt Using H2-, N2-, and NH3-Based Plasmas: On the Role of the Co-Reactant. *J. Phys. Chem. C* **2018**, *122* (39), 22519–22529.

(12) Jensen, D. S.; Kanyal, S. S.; Madaan, N.; Vail, M. A.; Dadson, A. E.; Engelhard, M. H.; Linford, M. R. Silicon (100)/Sio2 by Xps. *Surf. Sci. Spectra* **2013**, *20* (1), 36–42.

(13) Snoeckx, R.; Tennyson, J.; Cha, M. S. Theoretical Cross Sections for Electron Collisions Relevant for Ammonia Discharges Part 1: NH3, NH2, and NH. *Plasma Sources Sci. Technol.* **2023**, *32* (11), 115020.

(14) Cvejanovic, D.; Adams, A.; King, G. C. Radiative Lifetime Measurements of NH and CH Using the Electron-Photon Delayed Coincidence Method. *J. Phys. B At. Mol. Phys.* **1978**, *11* (9), 1653.

(15) Wiese, W. L.; Smith, M. W.; Glennon, B. Atomic Transition Probabilities. Volume 1. Hydrogen through Neon. **1966**.

(16) Artyushkova, K. Misconceptions in Interpretation of Nitrogen Chemistry from X-Ray Photoelectron Spectra. *J. Vac. Sci. Technol. A* **2020**, *38* (3), 031002. https://doi.org/10.1116/1.5135923.

(17) Fei, H.; Dong, J.; Arellano-Jiménez, M. J.; Ye, G.; Dong Kim, N.; Samuel, E. L. G.; Peng, Z.; Zhu, Z.; Qin, F.; Bao, J.; Yacaman, M. J.; Ajayan, P. M.; Chen, D.; Tour, J. M. Atomic Cobalt on Nitrogen-Doped Graphene for Hydrogen Generation. *Nat. Commun.* **2015**, *6* (1), 8668. https://doi.org/10.1038/ncomms9668.

(18) Hellgren, N.; Haasch, R. T.; Schmidt, S.; Hultman, L.; Petrov, I. Interpretation of X-Ray Photoelectron Spectra of Carbon-Nitride Thin Films: New Insights from in Situ XPS. *Carbon* **2016**, *108*, 242–252. https://doi.org/10.1016/j.carbon.2016.07.017.

(19) Biesinger, M. C.; Payne, B. P.; Grosvenor, A. P.; Lau, L. W. M.; Gerson, A. R.; Smart, R. St. C. Resolving Surface Chemical States in XPS Analysis of First Row Transition Metals, Oxides and Hydroxides: Cr, Mn, Fe, Co and Ni. *Appl. Surf. Sci.* **2011**, *257* (7), 2717–2730. https://doi.org/10.1016/j.apsusc.2010.10.051.

(20) Beamson, G. High Relution Xps of Organic Polymers. the Scienta Esca 300 Database. *ICIplc* **1992**.

(21) Godyak, V. A.; Piejak, R. B.; Alexandrovich, B. M. Electron Energy Distribution Function Measurements and Plasma Parameters in Inductively Coupled Argon Plasma. *Plasma Sources Sci. Technol.* **2002**, *11* (4), 525–543. https://doi.org/10.1088/0963-0252/11/4/320.

(22) Singh, H.; Graves, D. B. Measurements of the Electron Energy Distribution Function in Molecular Gases in an Inductively Coupled Plasma. *J. Appl. Phys.* **2000**, *87* (9), 4098–4106. https://doi.org/10.1063/1.373036.

(23) Boffard, J. B.; Jung, R. O.; Lin, C. C.; Aneskavich, L. E.; Wendt, A. E. Optical Diagnostics for Characterization of Electron Energy Distributions: Argon Inductively Coupled Plasmas. *Plasma Sources Sci. Technol.* **2011**, *20* (5), 055006. https://doi.org/10.1088/0963-0252/20/5/055006.

(24) Tong, L. Numerical Study of the Effect of Gas Flow in Low Pressure Inductively Coupled Ar/N2 Plasmas. *Open Phys.* **2012**, *10* (4), 888–897. https://doi.org/10.2478/s11534-012-0034-y.

(25) Heil, S. B. S.; Van Hemmen, J. L.; Van De Sanden, M. C. M.; Kessels, W. M. M. Reaction Mechanisms during Plasma-Assisted Atomic Layer Deposition of Metal Oxides: A Case Study for Al2O3. *J. Appl. Phys.* **2008**, *103* (10), 103302. https://doi.org/10.1063/1.2924406.

(26) Mione, M. A.; Engeln, R.; Vandalon, V.; Kessels, W. M. M.; Roozeboom, F. Infrared and Optical Emission Spectroscopy Study of Atmospheric Pressure Plasma-Enhanced Spatial ALD of Al2O3. *Appl. Phys. Lett.* **2019**, *115* (8), 083101. https://doi.org/10.1063/1.5113753.

(27) Boris, D. R.; Johnson, M. J.; Woodward, J. M.; Wheeler, V. D.; Walton, S. G. Remote Inductively Coupled Plasmas in Ar/N2 Mixtures and Implications for Plasma Enhanced ALD. *J. Vac. Sci. Technol. A* **2024**, *42* (3), 033008. https://doi.org/10.1116/6.0003538.

(28) Zhang, X.-Y.; Peng, D.-C.; Yan, J.-H.; Zhang, Z.-X.; Ruan, Y.-J.; Zuo, J.; Xie, A.; Wu, W.-Y.; Wuu, D.-S.; Huang, C.-J.; Lai, F.-M.; Lien, S.-Y.; Zhu, W.-Z. Plasma Power Effect on Crystallinity and Density of AlN Films Deposited by Plasma Enhanced Atomic Layer Deposition. *J. Mater. Res. Technol.* **2023**, *27*, 4213–4223. https://doi.org/10.1016/j.jmrt.2023.10.302.

(29) Yoon, H. J.; Jeon, H. Impact of Plasma Power on Plasma Enhanced Atomic Layer Deposited TiO2 as a Spacer. *Thin Solid Films* **2024**, *807*, 140551. https://doi.org/10.1016/j.tsf.2024.140551.

(30) Knoops, H. C. M.; Faraz, T.; Arts, K.; Kessels, W. M. M. (Erwin). Status and Prospects of Plasma-Assisted Atomic Layer Deposition. *J. Vac. Sci. Technol. Vac. Surf. Films* **2019**, *37* (3), 030902. https://doi.org/10.1116/1.5088582.

(31) Li, M.-Y.; Chang, Y.-Y.; Wu, H.-C.; Huang, C.-S.; Chen, J.-C.; Lue, J.-L.; Chang, S.-M. Effect of Process Pressure on Atomic Layer Deposition of Al[Sub 2]O[Sub 3]. *J. Electrochem. Soc.* **2007**, *154* (11), H967. https://doi.org/10.1149/1.2778861.

(32) Faraz, T.; Arts, K.; Karwal, S.; Knoops, H. C. M.; Kessels, W. M. M. Energetic Ions during Plasma-Enhanced Atomic Layer Deposition and Their Role in Tailoring Material Properties. *Plasma Sources Sci. Technol.* **2019**, *28* (2), 024002. https://doi.org/10.1088/1361-6595/aaf2c7.

(33) Profijt, H.; Potts, S.; Van de Sanden, M.; Kessels, W. Plasma-Assisted Atomic Layer Deposition: Basics, Opportunities, and Challenges. *J. Vac. Sci. Technol. A* **2011**, *29* (5).

(34) Hair, J. F. Multivariate Data Analysis. **2009**.

4 Plasma Characterisation of Remote ICP H_2/Ar Sources for PE-ALD

4.1 Introduction

Hydrogen-containing plasmas are widely utilised in plasma-enhanced atomic layer deposition (PE-ALD) due to their ability to provide highly reducing environments arising from the generation of hydrogen radicals[1]. These reactive species promote ligand removal and facilitate reduction reactions that are not achievable under conventional thermal ALD conditions[2]. As a result, hydrogen plasma enables low temperature film growth alongside other benefits typically associated with plasma-enhanced ALD, such as a wider range of film processes and improved film properties[3].

The production of metallic films via PE-ALD is often challenging due to the strongly reducing conditions required, especially for metals which oxidise readily[4]. Hydrogen plasma provides a means of generating a highly reducing environment capable of driving the necessary surface reactions. However, plasma exposure can also lead to undesirable effects such as surface damage, etching, or hydrogen incorporation into the film[5]. To mitigate these effects along with achieving improved process control, a detailed understanding of plasma behaviour through diagnostics is essential, as concluded by Boris et al[3].

Previous studies have shown that the inclusion of additional gases in the feed gas, such as N_2 or Ar, can significantly alter the characteristics of hydrogen plasmas[6]. In particular, the addition of argon has been reported to increase the generation of hydrogen radicals and improve plasma stability through enhanced electron density[7,8].

Optimisation of hydrogen plasma for PE-ALD processing remains challenging due to the large number of interacting parameters involved. Operating conditions such as power, pressure, feed-gas composition and flow all influence the generation and transport of reactive species. By isolating the ALD environment and focusing on plasma behaviour in a simplified case, a clearer understanding of these fundamental dependencies can be achieved.

The previous chapter demonstrated the value of optical emission spectroscopy (OES) as a diagnostic tool for PE-ALD of thin cobalt nitride films. A pre-ALD plasma response investigation revealed the potential of characterising and optimising the process plasma independently of deposition cycles. However, it was also shown that introducing the plasma into an ALD environment influences its response, though relative trends remain. As a result, pre-ALD parametric studies can effectively guide PE-ALD process optimisation while providing information into the plasma behaviour.

While OES provided valuable insight into excited species, it offered limited information about ground-state and ionised species. Therefore, a need for additional diagnostics was identified. In this chapter, a multi-diagnostic approach is used, taking advantage of the pre-ALD configuration to include invasive diagnostics. The plasma features investigated include the ion flux (Φ) at the substrate (approximately 250 mm from the remote source), the degree of H_2 dissociation (r_H), and the local mean electron energy (ε). These parameters provide a more quantitative and complete view of the plasma's response to the operating conditions.

Energy-resolved actinometry is employed to gain additional insight into plasma characteristics. This technique, as described in Chapter 2, is a modified version of the method demonstrated by Greb et al.[9], in which O_2/Ar plasma was examined. The present

implementation differs in key aspects, including operating pressure, gas composition, and mixture ratio. These modifications affect several of the assumptions made in the original method and have been discussed in detail in preceding chapters.

A systematic parametric study of the remote ICP source is presented here for a low-pressure H_2/Ar plasma. The study examines the effects of key operating parameters on plasma properties that are critical for PE-ALD processing. A multi-diagnostic approach is taken where energy-resolved actinometry is used to determine mean electron energy (ε) and molecular hydrogen dissociation (r_H). In addition, an ion flux probe is installed near the substrate to quantify the ion flux, which serves as an approximation for reactive species flux. Together, these diagnostics enable a more direct and quantitative characterisation of the plasma compared with OES alone.

The primary objective of this chapter is to establish a comprehensive parametric study of H_2/Ar plasma characteristics that can serve as a reference framework for interpreting plasma behaviour in PE-ALD environments. This framework provides diagnostic quantities extending beyond excited-state emissions, offering a more detailed foundation for understanding plasma–surface interactions. The results generated in this study form the basis for the following chapter, where these diagnostics are applied in situ to PE-ALD processes.

The results of Chapter 3 demonstrated significant variations in film growth and composition under different NH_3 plasma conditions, highlighting the influence of plasma behaviour on ALD processes. However, the NH_3 plasma was not characterised in detail, motivating a dedicated parametric study of a model H_2/Ar plasma in this chapter. Chapter 4 provides a foundational understanding of how key plasma features respond to changes

in operating parameters. This foundation is then applied in Chapter 5 to interpret and optimise PE-ALD processes.

4.2 Experimental Details

A parametric study of the remote ICP source was undertaken by systematically varying conditions including ICP power, chamber pressure, total flow, and gas mixing ratio for a H_2/Ar plasma. Prior to the study, the reactor was cleaned using a 3 min O_2 plasma exposure followed by a 30 s Ar purge. The system was then allowed to pump down to its base pressure of 1×10^{-6} mTorr before beginning the experiments.

ICP power was varied between 100 and 300 W in steps of 25 W. Chamber pressure was adjusted from 10 to 100 mTorr, spanning the typical operating window for ALD processes on this system, in steps of 10 mTorr. The gas mixture flow was varied between 15 and 55 sccm in steps of 10 mTorr and the H_2 gas composition fraction adjusted from 30% to 90% in increments of 10%. Reference values of 200 W ICP power, 50 mTorr pressure, 35 sccm total flow, and 80% H_2 were maintained for all parameters not under investigation. The maximum hydrogen flow was limited by the H_2 mass flow controller (50 sccm).

Each plasma was allowed to stabilise for 3 s before measurements were taken. OES was employed to record five spectra evenly spaced over a 2 s interval, covering the 350–1000 nm range. Appropriate integration times were selected to maximise signal intensity for each parameter set. The Hα (656.3 nm), Hβ (486.1 nm), and Ar $2p_1$ (750.4 nm) lines were used for the ERA diagnostics from the recorded spectra. As described in Chapter 2, from the ERA calculations quantitative plasma features were obtained, namely the local mean electron energy (ε) and the degree of dissociation of molecular hydrogen (r_H).

Ion flux was measured near the substrate plane using a planar ion flux probe mounted 50 mm above the heated substrate holder, corresponding to a transport distance of ~200 mm from the remote source. The probe was operated at a constant bias of -27 V, and the voltage drop across a 10 kΩ resistor was measured. The measured voltage is presented as

only the relative trends are investigated in this work. Multiple measurements were taken after the 3 s allocated to stabilise the plasma, and the results averaged. This measurement provides a practical approximation for the reactive species flux incident on the substrate during ALD processing.

4.3 Results

An initial investigation into the OES data focused on the stability of each plasma condition to determine whether any specific parameter sets produced unstable plasmas that should be avoided in PE-ALD processes. Stability was evaluated by monitoring the OES signals of the Ar $2p_1$ (750 nm) and Hα (656 nm) emission lines over the recorded 2 second interval. Once the stability of the full dataset had been established, the analysis shifted to investigating the response of the plasma for each parameter set.

4.3.1 Plasma stability

For each process condition, five consecutive OES spectra were recorded over a 2 s period. The mean and standard deviation of the Hα and Ar $2p_1$ intensities were calculated, and from these values the coefficient of variation ($CV = \sigma/\mu \times 100\%$) was obtained. This metric provides a normalised measure of variability that allows direct comparison between conditions. The resulting CV values for Hα and Ar $2p_1$ were then used to quantify plasma stability across the full set of parameter variations.

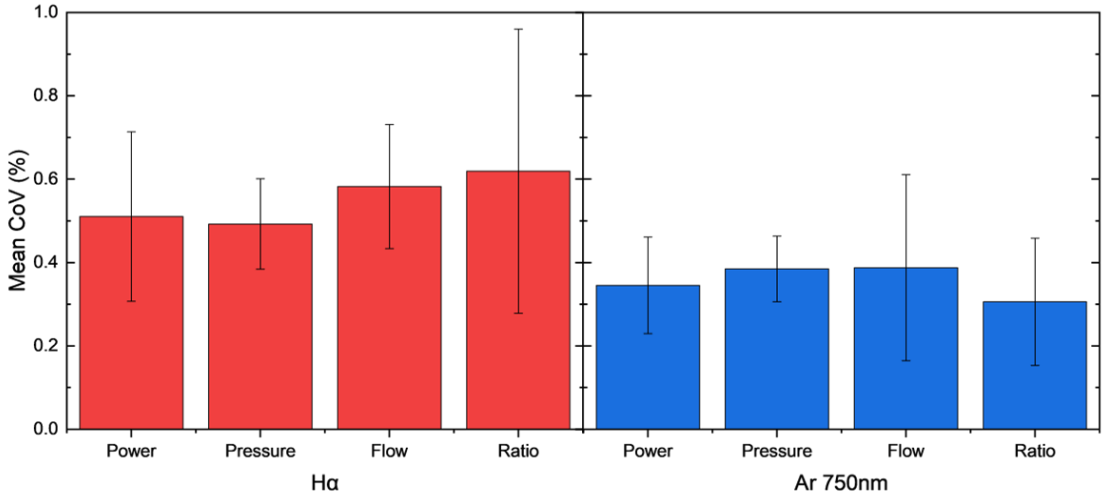


Figure 4.1 - Mean CV for Ha and Ar $2p_1$ emission lines, with error bar representing the standard deviation, for each plasma parameter investigated.

The mean CV values for all parameter sets are shown in Figure 4.1, with error bars representing the observed maximum and minimum values within each parameter group. Across all conditions studied, the CV remained below 2 %. The argon emission was consistently more stable, with maximum CV value of 1.2%, while the hydrogen emission exhibited slightly higher variability, reaching just over 1.8%. These results demonstrate that the plasma was highly stable under all variations of power, pressure, flow, and H_2/Ar ratio.

4.3.2 Plasma features vs parameters

The influence of each plasma condition was investigated by varying each parameter systematically while holding the other variables constant using the reference values described in the experimental details section of this chapter. For all plasma conditions the local mean electron energy, degree of dissociation and ion flux were measured and calculated.

4.3.2.1 Influence of ICP power

Figure 4.2 shows that the local mean electron energy decreased as ICP power is raised from 100 to 300 W. At 100 W the ε is 4.5 eV. The initial power increase to 175 W results in a uniform decrease to 4.2 eV. Further increases to the maximum power of 300 W only result in a further decrease of 0.1 eV at 300 W. The local mean electron energy was calculated using the ERA method which carries an uncertainty of ~ 30%, as previously described. The small change of 0.1 eV at high power is comparable to the 0.1 eV step size used in the calculation and is therefore not significant. The main trend is the larger decrease from 100 W to 175 W, followed by an approximate plateau at higher powers.

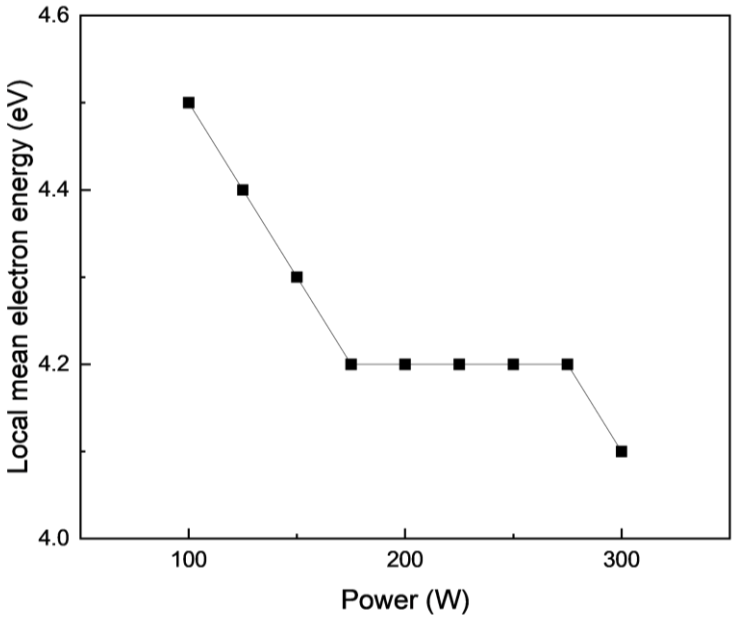


Figure 4.2 - Local mean electron energy (eV) vs ICP power (W).

The r_H has a two-stage response to increasing power, as seen in Figure 4.3. At the initial 100 W, r_H is 0.75 % which increases by nearly order of magnitude to 5.9 % at 175 W.

The increase from 100 W to 175 W has a near linear response. However, a linear response is then identified above for power increases above 175 W. 300 W provides the highest r_H of 11.5 %, indicating that higher powers produce more dissociative collisions.

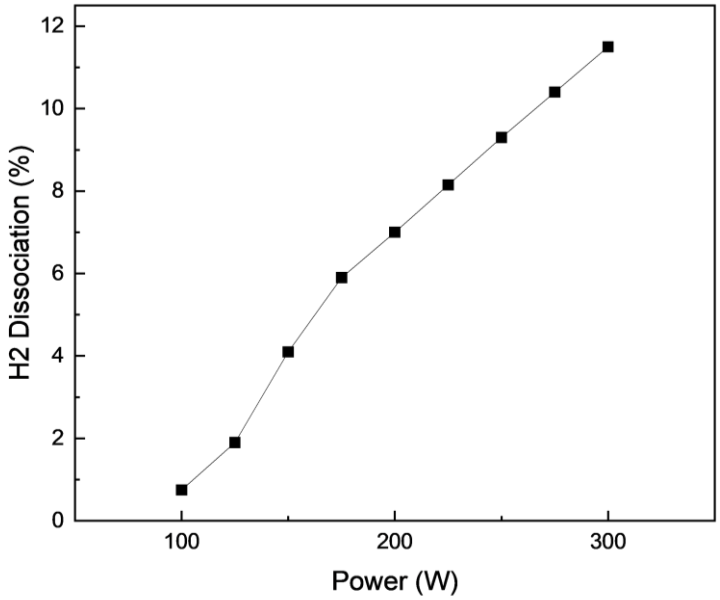


Figure 4.3 - Degree of H_2 dissociation (%) vs ICP power (W).

From Figure 4.4, between 100 W and 175 W the ion flux remains relatively constant, with values close to 30 mV. This plateau region indicates that initial increases in power do not translate into significant changes in ion delivery. Above 175 W the trend changes and the flux increase linearly, rising to 42.5 mV at 300 W. The data suggest a two-stage response with a low-power regime where ion flux is largely insensitive to power followed by a higher-power regime where the plasma couples energy more efficiently into ion generation and transport.

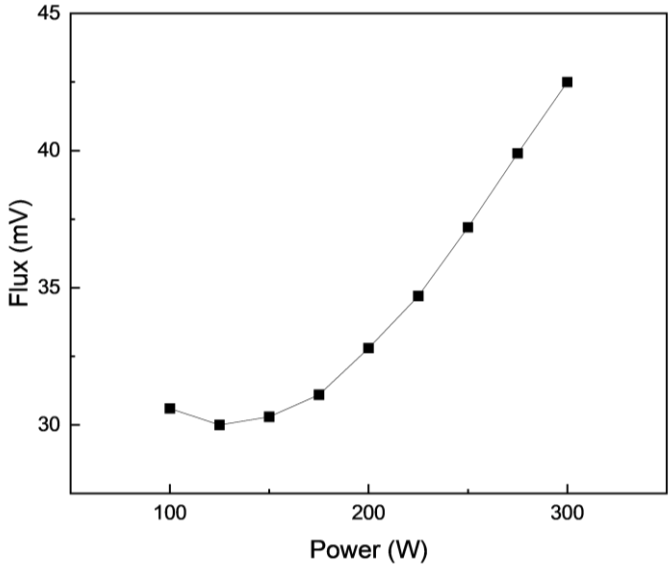


Figure 4.4 - Ion flux (mV) vs ICP power (W).

In summary, increasing ICP power produces a non-linear decrease in the local mean electron energy. A two-stage ion flux response with a low-power plateau and a high-power growth regime is observed. Additionally, there is also a steady rise in the degree of dissociation with indication of a two-stage response. The largest change in r_H was a result of power variations which increased by approximately 11% over the investigated range. Both the ion flux and ε had significantly smaller variations. These trends highlight power as a key control parameter governing reactive species production.

4.3.2.2 Influence of chamber pressure

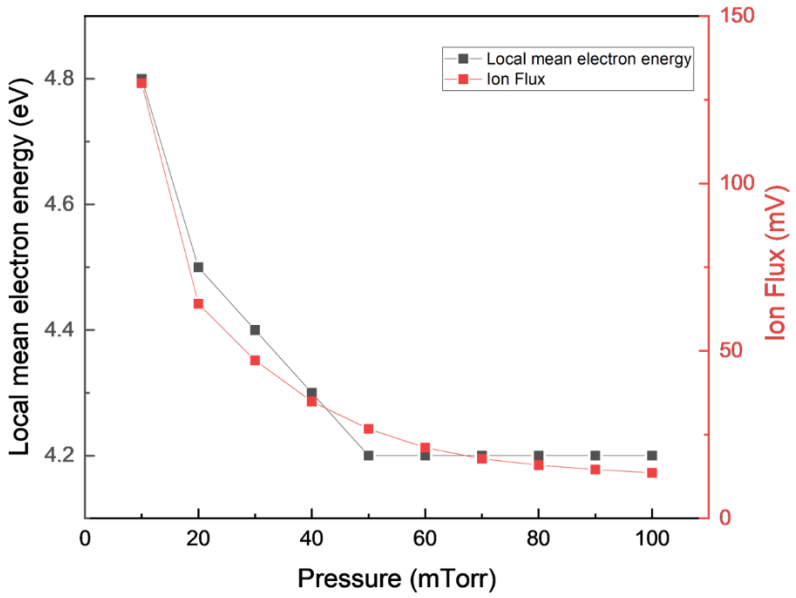


Figure 4.5 - (a) Local mean electron energy (eV) (black) & ion flux (mV) (red) for variations in chamber pressure (mTorr).

The ion flux, shown in Figure 4.5 (red), starts with 130 mV at 10 mTorr and it falls sharply to 64 mV at 20 mTorr, representing almost a 50% decrease. Between 20 and 100 mTorr the decline continues more gradually, reaching 13.6 mV at the highest pressure. The overall reduction is close to an order of magnitude and follows an exponential decay curve. This demonstrates that pressure is a dominant factor in determining ion and reactive species delivery to the substrate region.

The local mean electron energy had an initial strong decrease with pressure increasing from 10 to 40 mTorr resulting in a change from 4.8 to 4.3 eV. After 50mTorr was reached there was no further decrease from 4.2 eV. However, due to the step size of 0.1 eV it is possible there is a further decrease is masked due to the step size as seen in power

variations. From Figure 4.5, both the graphs show very similar trends suggesting the relationship of ε and pressure is exponential decay.

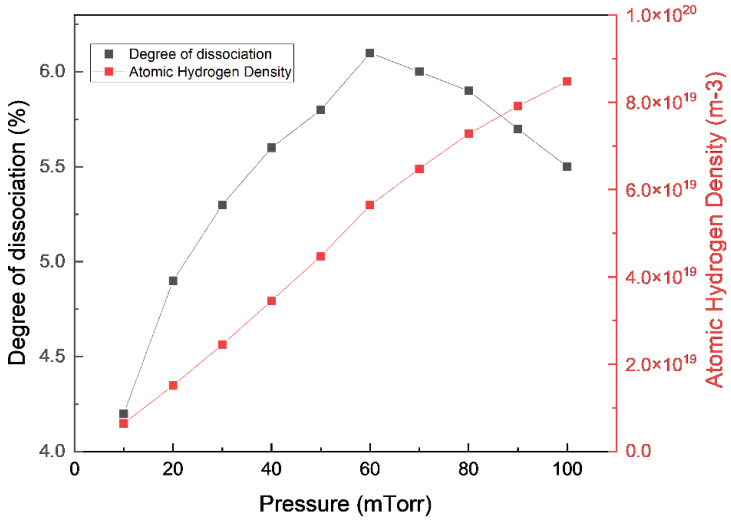


Figure 4.6 - (a) Degree of H_2 dissociation (r_H) (black) & atomic hydrogen density (n_H) (red) for variations in chamber pressure (mTorr).

Figure 4.6 presents the degree of dissociation (black) and atomic hydrogen density (n_H) (red). r_H follows a non-linear relationship. Increasing the pressure resulted in a slight increase to a maximum value at 60 mTorr. Further increases in pressure result in a slow decrease until the maximum pressure of 100 mTorr. The n_H increased consistently with increasing pressure, suggesting the base H_2 density from the pressure outweighs the changes in the degree of dissociation for producing the most atomic hydrogen density.

In summary, Figure 4.5 demonstrates that increasing chamber pressure results in a strong reduction of the local mean electron energy. There is also an exponential decay of ion flux with pressure reducing the number of reactive species reaching the substrate surface. The degree of dissociation has a maximum at 60 mTorr but a linear increase of atomic hydrogen density with pressure was found. While the pressure variations had influenced

all investigated plasma features, it produced the largest change in ion flux of around 120 mV. It's impact on ε and r_H were less significant. Pressure therefore plays a central role in the reactive species transport but is also influential in the reactive species generation.

4.3.2.3 Influence of gas flow

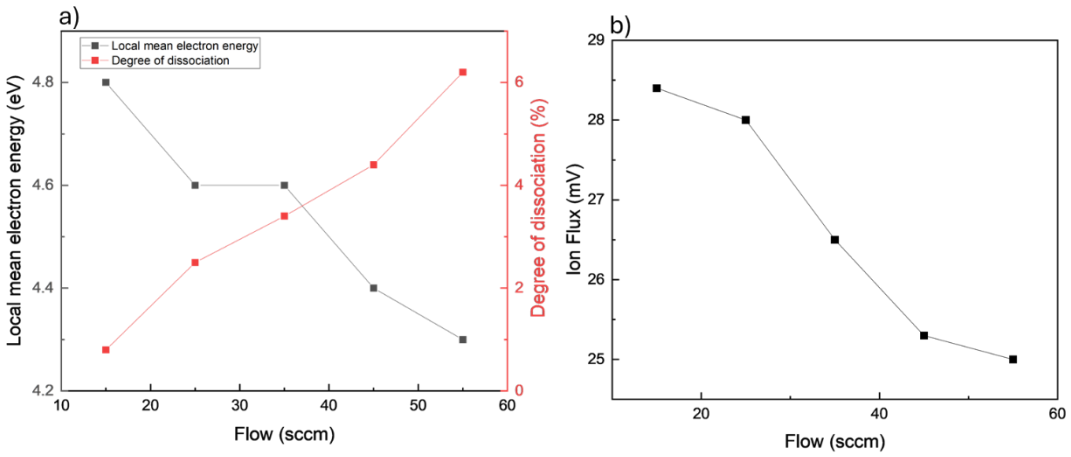


Figure 4.7 - (a) Local mean electron energy (eV) (black) & degree of dissociation (red) and b) ion flux (mV) for variations in total feed-gas flow (sccm).

From Figure 4.7 (a), it is seen that ε decreases with increasing total flow. At 15 sccm, ε is 4.8eV, falling to 4.6 eV at 35 sccm and then 4.3 eV at 55 sccm. The change in ε is of a similar order as that for pressure and greater than the power variation. r_H, rises from 0.8% at 15 sccm to 6.2% at 55 sccm. The relationship is close to linear across the investigated range. The change in r_H sits between the response of power and pressure, suggesting that while feed-gas flow is not the key influencing factor, it plays a significant role in atomic hydrogen generation.

The ion flux is 28.4 mV at 15 sccm, decreasing slightly to 28.0 mV at 25 sccm, 26.5 mV at 35 sccm, and 25.0 mV at 55 sccm, as seen inf Figure 4.7 (b). The changes are very small, showing that flow rate has negligible influence on reactive species transport.

In summary, Figure 4.7 demonstrates that increasing total flow results in a reduction of ε. While the overall change for ion flux was minimal, an inverse linear relationship was found. r_H was seen to be linear with flow. Variations produced the second largest change in r_H of around 5%. Flow is therefore another influencing parameter in the production of plasma species. However, it showed little impact on the transport of these species.

4.3.2.4 Influence of H2/Ar Ratio

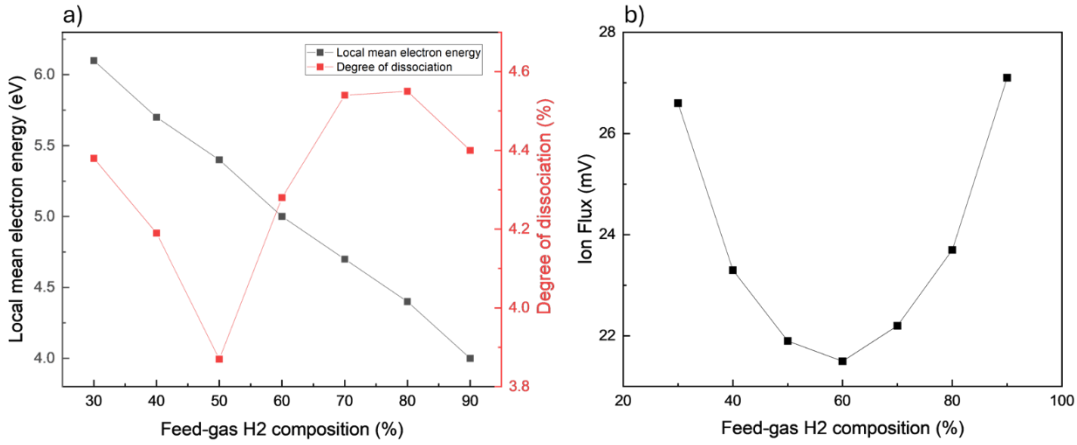


Figure 4.6 - (a) Local mean electron energy (eV) (black) & degree of dissociation (red) and b) ion flux (mV) for variations in H_2 feed-gas content (%).

Figure 4.8 (a) shows that ε is significantly impacted by the feed-gas mixture. Increasing the H_2 content from 30% to 90% results in ε to decrease by over 2 eV. There is an inverse linear relationship between the increasing H_2 content and the ε. The degree of dissociation fluctuates significantly with increasing H_2 content. For increases in the H_2 content from 30 to 50 % there is an initial linear decrease in r_H. Above 50% H_2, another regime

dominated resulting in a non-linear increase to a maximum at 70-80% H_2, after this r_H begins to decrease. However, the overall absolute change in the degree of dissociation remains below 0.6 % for all investigated gas mixtures.

From the ion flux trend, Figure 4.6 (b), there is a local minimum at 60 % at H_2. The overall variation is relatively low compared to power and pressure variations of approximately 7mV, but the non-linear behaviour indicates a balance between argon-driven ionisation at low H_2 fractions and hydrogen-dominated ionisation at high fractions.

In summary, Figure 4.8 demonstrates that increasing the H_2 content produces significant changes in the local mean electron energy. The other investigated parameters produced a similar range of around 4.6 - 4.2 eV while variations in the feed-gas content produced a range of 6 - 4 eV. As such, feed-gas mixture is a controlling parameter of the electronic properties of the plasma. Minimal changes in ion flux and the degree of dissociation were observed. Overall, the response of the plasma due to feed-gas mixture had minimal impact on the key features of ion flux and r_H making it a lesser priority for investigation.

The systematic uncertainty associated with energy-resolved actinometry is estimated to be approximately 30% as discussed in the Chapter 2. As a result, no statistical error bars derived from the variation over the 2 s measurement window are shown for the plasma features, as this would misrepresent the dominant error source. The observed OES stability ensures that the statistical contribution is negligible compared to the systematic error, and the reported features can be interpreted reliably in terms of relative trends.

4.4 Discussion

From the above results, each investigated parameter was found to influence the plasma behaviour. The discussion section is organised according to the impact of the parameter on different aspects of the plasma. First is a discussion on the effect on the electrons within the plasma, as characterised by the local mean electron energy. This is followed by a discussion on the influence on the generation and transport of reactive species, as evidenced by ion flux measurements and H_2 dissociation.

4.4.1 Impact of controlled parameters on electronic properties of the discharge

The ε decreased non-linearly with increasing power. The 100 W plasma produced a value of 4.5 eV which fell to 4.2 at 175 W at which the value remained until a final drop to 4.1 eV at 300 W. It is clear from these results that increasing the ICP power reduced the overall local mean electron energy. Godyak et al showed that in an Ar ICP, increasing power reduced the mean electron energy at pressures in the range of 10-100 mTorr[10]. It was stated that at higher densities, electron-electron collisions increased which 'Maxwellianises' the low-energy region of the EEDF. The Ar ionisation process becomes dominated by two-step excitation which results in a lower mean energy and higher ionisation with increased power. Jang et al showed that there was a similar decrease in electron energy for a H_2 ICP plasma with increasing power at 30 mTorr[11]. The overall reduction of 0.3 eV between 100 W and 175 W indicates a transition from E-mode (capacitively coupled) to H-mode (inductively coupled) which results in a significant increase in electron density[12]. As discussed by Godyak, this increase in density leads to enhanced collisional processes that reduce the mean electron energy. While a reduction

in ε at the centre of the discharge might be attributed to a shielding effect, the skin depth at these conditions is small compared with the plasma dimensions, and the RF fields would not be expected to penetrate to the centre. Therefore, any shielding within this region is minimal, and the observed reduction in ε remains small, consistent with previous studies.

The variation of pressure produced a larger change in the ε of 0.6 eV, while maintaining a similar range to the power variations. It was seen that the reduction followed an exponential decay curve with initial pressure increases from 10 mTorr to 20 mTorr having the largest impact. Work by Boffard et al showed that in a low pressure ICP Ar plasma both probe and optical measurements observed a similar trend of decreasing electron temperature with increasing pressure in the range of 1-25 mTorr[15]. Similar results were found by Rauner et al for low pressure ICP H_2 plasma[16]. Over a 7.5 to 75 mTorr range an exponential decay curve, similar to this work, was observed reducing the electron temperature from approximately 4 eV to 2.5 eV. These works found that increasing the operating pressure increased the plasma density which in turn resulted in increased collisional processes and reduced mean free path (MFP) which drive the mean electron energy down. The results observed in this work align well with previous low pressure ICP studies.

Increases in feed-gas flow reduced the mean electron energy by a similar overall range as the increased pressure variation. However, the trend observed was linear in nature for this work. Previous work using global modelling demonstrated that increased flow increased the electron density along with decreasing the electron temperature[17]. This can be understood by considering the through-put of species in the source. Increased feed-gas flow reduces the residence time of individual neutral species in the plasma, meaning each particle spends less time in the source. However, the higher flow also increases the

absolute number of neutrals entering the plasma per unit time, raising the overall neutral density within the source. With more neutrals available for ionisation and excitation, the electron production rate increases, resulting in a higher electron density. The higher electron density then leads to more frequent collisions, which enhances collisional cooling and reduces the mean electron energy (ε), consistent with the observed trend.

Varying the feed-gas H_2 composition had the largest effect on the ε. In this work, increasing the H_2 composition resulted in a significant decrease in the ε. Hjartarson et al showed that in a global model of a low-pressure H_2/Ar discharge, increasing the H_2 content increased the electron temperature under Maxwellian conditions[18]. Further investigation showed that adopting a Druyvesteyn model increased the electron temperature significantly, approximately 40%, to sustain the same ionisation rates. Kimura et al experimentally investigate ICP H_2/Ar discharges and observed a change from Druyvesteyn-like to Maxwellian-like distributions as the H_2 content increased[19]. Figure 4.9 presents example Druyvesteyn and Maxwellian electron energy distribution functions (EEDFs). The Druyvesteyn distribution is characterised by a relatively broad peak and a suppressed high-energy tail, while the Maxwellian distribution exhibits a more exponential decay at higher energies.

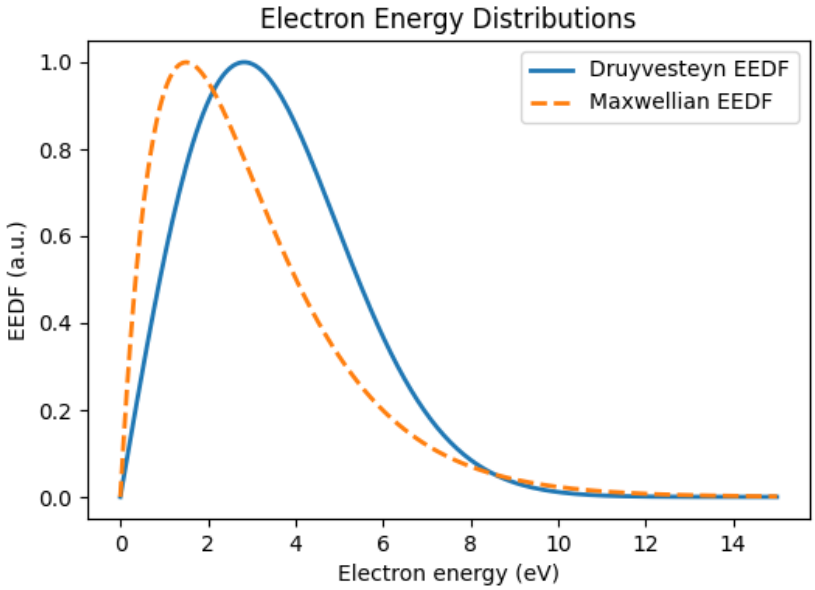


Figure 4.9 – Electron energy distribution functions (EEDFs) of a Druyvesteyn (blue) distribution and Maxwellian (orange) distribution.

Increased e-H_2 collisions reduced the apparent electron temperature with increased H_2 composition. Jiménez-Redondo et al also investigated varying H_2 content in H_2/Ar discharges at low pressures[20]. They found a reduction in the electron temperature with increasing H_2 content, which they attributed to a change in the plasma kinetics towards vibrational energy exchange, which contributes to the Maxwellian-like distribution. Smith et al.[14] demonstrated that in a H_2 plasma, spatial variations in gas temperature modify the vibrational distribution function (VDF). Such changes, through electron-vibration coupling, can indirectly influence electron energy within the discharge. At low H_2 content, the plasma EEDF is Druyvesteyn-like, with less low-energy electrons and an increased mean electron energy. Increasing the H_2 fraction introduces more vibrational inelastic collisions, which cool the bulk of the electron population and promotes thermalisation, producing a Maxwellian-like distribution. Despite the Maxwellian tail extending to higher energies, most electrons occupy lower energies, resulting in a reduced

mean electron energy. These trends are consistent with the observed reduction in ε with increasing H_2 content.

The results demonstrate that variations in power, pressure, and gas flow rate each exert only a small influence on the local mean electron energy. Their overall impact produces changes of less than 1 eV over the ranges investigated. These parameters have been shown to primarily change the collisional rate and density of the discharge, leading to cooling. In contrast, the feed-gas composition emerged as a dominant factor for controlling the ε. Increased hydrogen composition altered the electron energy distribution function from Druyvesteyn-like to Maxwellian-like. This was achieved through the promotion of vibrational cooling and collisional thermalisation. The distribution change reduced the high energy electron tail proportion leading to lower observed ε. Overall, the findings indicated that the gas composition is the principal factor determining the electronic properties of the plasma.

4.4.2 Impact of controlled parameters on reactive species generation and transport

4.4.2.1 Species generation

The generation of reactive species for this work is defined by the dissociation fraction along with the atomic hydrogen density. Since the atomic hydrogen density scales with the degree of dissociation and the H_2 density (which is determined by pressure only within this work) all parameters except pressure variations only investigated the degree of dissociation.

Variations of the power had the largest influence on the dissociation of H_2, with 100 W resulting in 0.8 % and 300 W resulting in over an order of magnitude increase to

approximately 11 %. This significant increase has been demonstrated by previous publications. Abdel-Rahman et al used a range of diagnostic methods and demonstrated that increasing the power in a H_2/Ne/Kr ICP plasma (95%,3.5%,1.5%, respectively) resulted in a near linear increase for 100 W – 250 W with a saturation occurring above this[21]. It was concluded that a mode transition from a low-density (E-mode) to higher density (H-mode) occurred with increased power producing the increased dissociative efficiency. In the work the r_H increases near linearly with increasing from 100 W to 175 W, then linearly from 175 W to 300 W. From the powers influence on the mean electron energy, a mode transition between 100 W and 175 W was identified. This explains the significant increase observed in r_H in this range. The transition results in a significant increase in electron density, which the degree of dissociation depends on. Increases in the electron density directly increase the probability of dissociative collisions.

Abdel-Rahman additionally showed that variations in pressure from 35 mTorr to 180 mTorr resulted in an initial increase in dissociation fraction to a maximum found at 75 mTorr, before a gradual decrease. Other work by Iordanova et al showed that in a H_2/Ar discharge at lower pressures, 7.5 – 45 mTorr, there was a linear increase in r_H with pressure[22]. The initial increased pressure aids collisional excitation and enhances dissociation. At higher pressures energy losses due to decreased MFP reduces the dissociation efficiency. Both the described effects can be observed in this work with a maximum degree of dissociation occurring at 60 mTorr, which aligns well with published results. While the pressure variations did result in changes in r_H, it must be noted that the maximum change that occurred was only 1.3 %, suggesting that the pressure plays a minimum role in dissociation efficiency.

Feed-gas flow provided the second largest change in the degree of dissociation, with an overall change of approximately 5.5% over the investigated range. A linear relationship

was observed. While little published work on the impact of flow for similar set ups was found, some publications provide insight into this works results. Gordiets et al investigate low pressure N_2- H_2 discharges with varying flow rates[23]. From this work it was observed that flow rates determine the residence time in the source and higher flow resulted in less local dissociation. However, an investigation into Ar/O_2 discharge by Gavrilov et al demonstrated that a low to moderate flow O_2 regime (30-100sccm) resulted in increased degree of dissociation, while higher flow regimes (>100 sccm) which led to increased pressure resulted in saturation[24]. It was proposed that the local O_2 density depends on the flow and geometry as opposed to static pressure, moderate flows lead to increased local density promoting electron-impact dissociation.

The feed-gas composition was shown to have little impact on the degree of dissociation, with a maximum change of approximately 0.5 %. Hjartarson demonstrated that increasing the H_2 concentration in a H_2/Ar discharge slightly increases in r_H over 20 – 60 mTorr range.

This work demonstrates the impact of the investigated plasma parameters on the degree of dissociation in a low-pressure ICP H_2/Ar discharge followed trends found in previously published works with similar set ups. Both the feed-gas composition and the chamber pressure provide little control over the resulting degree of dissociation. Increased control can be obtained by varying the feed-gas flow. However, the most significant parameter for the generations of key reactive species, in this case atomic hydrogen, is the ICP power.

4.4.2.2 Species transport

As previously stated, in this work the ion flux measurements are utilised as an approximation for reactive species transport from the remote ICP source to the substrate.

Ionisation primarily occurs in the bulk plasma near the ICP source, where the electron density and energy are sufficient to drive ionisation of neutral species. The ions and radicals generated in this region then transport downstream toward the substrate. Although the RF fields are largely confined to the outer regions of the dense plasma due to the limited skin depth, the bulk plasma maintains sufficient electron energy to sustain ionisation. By the time the reactive species reach the substrate, the local fields are minimal, and transport is dominated by collisions and recombination rather than further acceleration by the RF field. Under these conditions, the ion flux measured at the substrate provides a reliable representation of reactive species delivery, offering key insight into how each process parameter influences transport from the source to the substrate. Increases in the ICP power resulted in a two-stage response with ion flux. The initial response showed little change in the ion flux with increasing power. After 150 W there was a shift to a second regime which was seen to have a linear relationship with power, increasing from ~30 to ~42 mV. Chevolleau et al demonstrated that increasing a low pressure ICP Ar discharge power resulted in a near linear relationship with ion flux[25]. The setup involved included a remote ion flux gauge located approximately 10 cm from the source. A two-stage response wasn't found in this work, suggesting a pure Ar discharge could have a different response. The previously described work by Abdel-Rahman demonstrated a mode change in a hydrogen discharge from E-mode to H-mode around 100/150 W which resulted in a higher electron density. A significant increase in ion density produced because of increased electron density, from such a mode transition, could mitigate transport losses such as recombination. With a constant pressure, transport losses due to collisions remain consistent and a significant increase in production of ion would result in a linear trend seen above 150 W. This suggests that a regime change is indicated by the two-stage response of ion flux in this work.

Yoon et al demonstrated a reduction in ion flux of 8.8 times in an Ar/CH_4 ICP discharge when increasing the pressure from 35 to 240 mTorr[26]. A similar non-linear trend to this work was also observed for intermediary pressures. The decay of ion flux with increasing pressure occurs due to a shortening of the mean free path leading to more collisional losses during transport. This general effect of pressure reducing the mean free path has also been observed in work by Kusano et al, who noted that decreased MFP increased the probability of collisions which decreased the mean energy[27]. While not directly related to ion flux, Kusano's work further strengthens to collisional loss of ion flux during transport. The results from the current work demonstrated the significant impact of pressure on the transport of reactive species to the substrate with a massive drop from 130 to 65 mV when increasing from 10 to 20 mTorr chamber pressure. Pressure is therefore a critical parameter of remote sources for use in PE-ALD processing.

Increasing the flow led to a linear reduction in ion flux. However, compared with power and pressure the overall change in ion flux due to variations in flow was minimal, with a maximum change of approximately 3.5 mV. This suggests that feed-gas flow has a weak link to the transport effects. Previous work by Doh et al demonstrated that the ion current density was found to depend on the gas composition[28]. In a pure Ar ICP discharge, increased flow resulted in increased detected current density or flux. However, a C_4F_8 discharge was shown to have decreased ion flux with increased flow. It was concluded that atomic and molecular discharges differ due to the enhanced electron losses from vibrational and dissociative channels. From this the reduction observed in the presented work can be understood. The introduction of molecular hydrogen into the discharge brings additional low threshold channels which reduce the high-energy tail of the EEDF, resulting in reduced ionisation. To increase the ionisation rate an increased residence time is required, hence a low flow is needed. While variation in flow impacts the ion

generation and therefore reactive species transport, the overall impact is minimal compared to other influential parameters.

Sode et al investigated a H_2/Ar ICP plasma using an energy dispersive mass spectrometer allowing them to calculate the ion densities of the plasma species as a function of Ar content[29]. It was found that there was a dependence on gas composition. In low H_2 content, Ar ionisation dominated, but the H_2 cooled electrons. Further increase in H_2 to roughly 50% composition had the minimal ion density as both Ar and H_2 ionisation was suppressed. Further increased lead to H_2 dominated ionisation through H^{3+} ions. This non-linear relationship was observed in the presented results with a minimal found at 60% H_2 content. The overall flux measurements showed a change of ~6 mV suggesting the gas composition impacts the species generated but has significantly less of an impact on the transport and ion density than other influencing parameters investigated.

In summary, it was observed that pressure dominates the effect on transport of generated reactive species to the substrate due to collisional losses. As such a low-pressure plasma maximised the density of reactive species at the substrate surface. Power was also found to have an influence on the ion flux, but it was concluded that the increase associated with power was due to the generations of species as opposed to their transport. Both feed-gas flow and composition had less of an impact on the ion flux. Their main effect was in the creation of reactive species rather than affecting transport.

4.5 Conclusion

The aim of this chapter was to establish how the controllable operating parameters influence the response of the low pressure ICP H_2/Ar plasma. The systematic parametric study revealed that each parameter produces distinct and quantifiable effects on the plasma, with implications for the design of a process-optimised plasma environment.

The local mean electron energy was found to vary only weakly (< 1 eV) with changes in ICP power, chamber pressure, and feed-gas flow, indicating that these parameters primarily affect plasma density and collisional rates rather than the electron energy distribution. In contrast, gas composition had the dominant influence on the electronic properties. Increasing the H_2 content of the feed-gas transformed the EEDF from a Druyvesteyn-like to a Maxwellian-like distribution through enhanced vibrational cooling and collisional thermalisation, leading to a measurable reduction in the high-energy electron population.

Reactive species generation, quantified through the degree of H_2 dissociation, increased linearly with applied ICP power and exhibited only minor sensitivity to pressure or composition. This identifies power as the key control parameter for regulating the production of atomic hydrogen, which is critical for precursor reduction in PE-ALD. The transport of these species, as approximated by the ion-flux measurements, was governed primarily by chamber pressure. A significant reduction in flux was observed with increasing pressure, consistent with enhanced collisional losses and shortened mean free paths. Power exerted a secondary influence through its effect on overall ion production, while gas flow and composition played relatively minor roles.

Overall, this study provides key insights into the operational window that maximizes the availability of reactive species at the substrate. The next chapter applies the insights

gained to a Cu PE-ALD process. The processing parameters are systematically varied to enable an investigation of film growth behaviour as a function of plasma characteristics. Based on the results of this chapter, correlations between the processing parameters, plasma response, and film properties are established.

4.6 References

(1) Profijt, H.; Potts, S.; Van de Sanden, M.; Kessels, W. Plasma-Assisted Atomic Layer Deposition: Basics, Opportunities, and Challenges. *J. Vac. Sci. Technol. A* **2011**, *29* (5).

(2) Kim, H.; Oh, I.-K. Review of Plasma-Enhanced Atomic Layer Deposition: Technical Enabler of Nanoscale Device Fabrication. *Jpn. J. Appl. Phys.* **2014**, *53* (3S2), 03DA01. https://doi.org/10.7567/JJAP.53.03DA01.

(3) Boris, D. R.; Wheeler, V. D.; Nepal, N.; Qadri, S. B.; Walton, S. G.; Eddy, C. (Chip) R. The Role of Plasma iFn Plasma-Enhanced Atomic Layer Deposition of Crystalline Films. *J. Vac. Sci. Technol. A* **2020**, *38* (4), 040801. https://doi.org/10.1116/6.0000145.

(4) Knoops, H. C. M.; Faraz, T.; Arts, K.; Kessels, W. M. M. (Erwin). Status and Prospects of Plasma-Assisted Atomic Layer Deposition. *J. Vac. Sci. Technol. Vac. Surf. Films* **2019**, *37* (3), 030902. https://doi.org/10.1116/1.5088582.

(5) Kim, K.; Oh, I.-K.; Kim, H.; Lee, Z. Atomic-Scale Characterization of Plasma-Induced Damage in Plasma-Enhanced Atomic Layer Deposition. *Appl. Surf. Sci.* **2017**, *425*, 781–787. https://doi.org/10.1016/j.apsusc.2017.06.241.

(6) Vos, M. F.; van Straaten, G.; Kessels, W. E.; Mackus, A. J. Atomic Layer Deposition of Cobalt Using H2-, N2-, and NH3-Based Plasmas: On the Role of the Co-Reactant. *J. Phys. Chem. C* **2018**, *122* (39), 22519–22529.

(7) Bogaerts, A.; Gijbels, R. Effects of Adding Hydrogen to an Argon Glow Discharge: Overview of Relevant Processes and Some Qualitative Explanations. *J. Anal. At. Spectrom.* **2000**, *15* (4), 441–449. https://doi.org/10.1039/a909779a.

(8) Avtaeva, S. H_2 Dissociation in Ar–H_2 Arc Discharge of Moderate Pressure. *Plasma Res. Express* **2019**, *1* (1), 015018. https://doi.org/10.1088/2516-1067/ab10c0.

(9) Greb, A.; Niemi, K.; O'Connell, D.; Gans, T. Energy Resolved Actinometry for Simultaneous Measurement of Atomic Oxygen Densities and Local Mean Electron Energies in Radio-Frequency Driven Plasmas. *Appl. Phys. Lett.* **2014**, *105* (23).

(10) Godyak, V. A.; Piejak, R. B.; Alexandrovich, B. M. Electron Energy Distribution Function Measurements and Plasma Parameters in Inductively Coupled Argon Plasma. *Plasma Sources Sci. Technol.* **2002**, *11* (4), 525–543. https://doi.org/10.1088/0963-0252/11/4/320.

(11) Jang, S.; Lee, W. Pressure and Input Power Dependence of Ar/N2H2 Inductively Coupled Plasma Systems. *J. Vac. Sci. Technol. Vac. Surf. Films* **2001**, *19* (5), 2335–2343. https://doi.org/10.1116/1.1385904.

(12) Abdel-Rahman, M.; Gathen, V. S. D.; Gans, T. Transition Phenomena in a Radio-Frequency Inductively Coupled Plasma. *J. Phys. Appl. Phys.* **2007**, *40* (6), 1678–1683. https://doi.org/10.1088/0022-3727/40/6/017.

(13) Holm, A.; Wünderlich, D.; Groth, M.; Börner, P. Impact of Vibrationally Resolved H_2 on Particle Balance in Eirene Simulations. *Contrib. Plasma Phys.* **2022**, *62* (5–6), e202100189. https://doi.org/10.1002/ctpp.202100189.

(14) Smith, G. J.; Diomede, P.; Gibson, A. R.; Doyle, S. J.; Guerra, V.; Kushner, M. J.; Gans, T.; Dedrick, J. P. Low-Pressure Inductively Coupled Plasmas in Hydrogen: Impact of Gas Heating on the Spatial Distribution of Atomic Hydrogen and Vibrationally Excited States. *Plasma Sources Sci. Technol.* **2024**, *33* (2), 025002.

(15) Boffard, J. B.; Jung, R. O.; Lin, C. C.; Wendt, A. E. Optical Emission Measurements of Electron Energy Distributions in Low-Pressure Argon Inductively Coupled Plasmas. *Plasma Sources Sci. Technol.* **2010**, *19* (6), 065001. https://doi.org/10.1088/0963-0252/19/6/065001.

(16) Rauner, D.; Briefi, S.; Fantz, U. Influence of the Excitation Frequency on the RF Power Transfer Efficiency of Low Pressure Hydrogen ICPs. *Plasma Sources Sci. Technol.* **2019**, *28* (9), 095011. https://doi.org/10.1088/1361-6595/ab3d6a.

(17) Tong, L. Numerical Study of the Effect of Gas Flow in Low Pressure Inductively Coupled Ar/N2 Plasmas. *Open Phys.* **2012**, *10* (4), 888–897. https://doi.org/10.2478/s11534-012-0034-y.

(18) Hjartarson, A. T.; Thorsteinsson, E. G.; Gudmundsson, J. T. Low Pressure Hydrogen Discharges Diluted with Argon Explored Using a Global Model. *Plasma Sources Sci. Technol.* **2010**, *19* (6), 065008. https://doi.org/10.1088/0963-0252/19/6/065008.

(19) Kimura, T.; Kasugai, H. Properties of Inductively Coupled Rf Ar/H2 Plasmas: Experiment and Global Model. *J. Appl. Phys.* **2010**, *107* (8), 083308. https://doi.org/10.1063/1.3345084.

(20) Jiménez-Redondo, M.; Cueto, M.; Doménech, J. L.; Tanarro, I.; Herrero, V. J. Ion Kinetics in Ar/H_2 Cold Plasmas: The Relevance of ArH^+. *RSC Adv* **2014**, *4* (107), 62030–62041. https://doi.org/10.1039/C4RA13102A.

(21) Abdel-Rahman, M.; Gathen, V. S. D.; Gans, T.; Niemi, K.; Döbele, H. F. Determination of the Degree of Dissociation in an Inductively Coupled Hydrogen

Plasma Using Optical Emission Spectroscopy and Laser Diagnostics. *Plasma Sources Sci. Technol.* **2006**, *15* (4), 620–626. https://doi.org/10.1088/0963-0252/15/4/005.

(22) Iordanova, S.; Koleva, I.; Paunska, T. Hydrogen Degree of Dissociation in a Low Pressure Tandem Plasma Source. *Spectrosc. Lett.* **2011**, *44* (1), 8–16. https://doi.org/10.1080/00387010903386540.

(23) Gordiets, B.; Ferreira, C. M.; Pinheiro, M. J.; Ricard, A. Self-Consistent Kinetic Model of Low-Pressure - Flowing Discharges: II. Surface Processes and Densities of N, H, Species. *Plasma Sources Sci. Technol.* **1998**, *7* (3), 379–388. https://doi.org/10.1088/0963-0252/7/3/016.

(24) Gavrilov, N.; Kamenetskikh, A.; Tretnikov, P.; Krivoshapko, S. Increasing the Oxygen Dissociation Degree in the Plasma of a Pulse-Periodic Ar/O_2 Low-Pressure Arc. *Plasma Sources Sci. Technol.* **2021**, *30* (9), 095008. https://doi.org/10.1088/1361-6595/ac12d8.

(25) Chevolleau, T.; Fukarek, W. Ion Flux, Ion Energy Distribution and Neutral Density in an Inductively Coupled Argon Discharge. *Plasma Sources Sci. Technol.* **2000**, *9* (4), 568–573. https://doi.org/10.1088/0963-0252/9/4/312.

(26) Yoon, M. Y.; Jeong, J.-R.; Lee, H.-C.; Kim, J.-H. Plasma Low-Energy Ion Flux Induced Vertical Graphene Synthesis. *Appl. Surf. Sci.* **2023**, *636*, 157814. https://doi.org/10.1016/j.apsusc.2023.157814.

(27) Kusano, E.; Fukushima, K.; Saitoh, T.; Saiki, S.; Kikuchi, N.; Nanto, H.; Kinbara, A. Effects of Ar Pressure on Ion Flux Energy Distribution and Ion Fraction in r.f.-Plasma-Assisted Magnetron Sputtering. *Surf. Coat. Technol.* **1999**, *120–121*, 189–193. https://doi.org/10.1016/S0257-8972(99)00453-3.

(28) Doh, H.-H.; Horiike, Y. Gas Residence Time Effects on Plasma Parameters: Comparison between Ar and C_4F_8. *Jpn. J. Appl. Phys.* **2001**, *40* (5R), 3419. https://doi.org/10.1143/JJAP.40.3419.

(29) Sode, M.; Schwarz-Selinger, T.; Jacob, W. Quantitative Determination of Mass-Resolved Ion Densities in H2-Ar Inductively Coupled Radio Frequency Plasmas. *J. Appl. Phys.* **2013**, *113* (9), 093304. https://doi.org/10.1063/1.4794165.

5 Plasma monitoring and characterisation and in-situ film characterisation of Cu PE-ALD

5.1 Introduction

This chapter investigates the growth of thin copper (Cu) films via plasma-enhanced atomic layer deposition (PE-ALD). Cu plays a critical role in modern microelectronics with a large range of applications such as interconnect material[1] and flexible electronic devices[2] due to its excellent electrical and thermal conductivity[3]. As device dimensions continue to shrink, there is an increasing demand for highly conformal, uniform, and precise Cu deposition. Atomic layer deposition (ALD) provides a powerful method for achieving these requirements through its self-limiting surface reactions, enabling atomic scale thickness control and step coverage.

Cu ALD has been extensively studied using a range of metal-organic precursors and co-reactants[4–6]. Many thermal processes rely on hydrogen gas as a reducing agent and require high substrate temperatures to achieve metallic Cu[7,8]. Wu et al.[9] investigated thermal ALD of Cu using $Cu(acac)_2$ and H_2 as the co-reactant, but no film growth was observed below 230 °C. When the H_2 co-reactant was replaced by an H_2 plasma, self-limited growth was achieved within an ALD temperature window of 85–135 °C, demonstrating that atomic hydrogen generated in the plasma is essential for reduction in low temperature processes.

Knisley et al have previously discussed the relative ease of reduction of Cu compared to other first row transition metals[10] in ALD processes. Faraz et al.[11] demonstrated that increasing the ion flux enhances the total energy delivered to the substrate, which can promote film densification, crystallisation, and impurity removal for general PE-ALD.

However, there is a lack of knowledge of the influence of plasma conditions over $Cu(acac)_2$ PE-ALD. This chapter focuses on an investigation into $Cu(acac)_2$ and H_2/Ar PE-ALD processing to provide a valuable insight into the plasmas influence on film properties.

The effects of ICP power, chamber pressure, and gas flow on the plasma features and resulting Cu film properties are examined. In-situ plasma diagnostics are employed to monitor plasma behaviour during each ALD cycle, providing features such as the local mean electron energy and degree of H_2 dissociation. These measurements are then correlated with in-situ XPS measurements to establish relationships between plasma behaviour and film properties. Parametric trends established from the previous chapter allows for an improved understanding of the ALD environments impact on the plasma behaviour and ultimately the produced films properties. Previously, the degree of H_2 dissociation was found to vary linearly with ICP power. A reference power of 200 W was selected, with high and low values of 300 W and 100 W, respectively. Chamber pressure displayed the most significant effect on ion flux at the substrate surface following a non-linear trend. 40 mTorr was chosen as the reference condition, with 10 mTorr and 70 mTorr used to investigate both the low- and high-pressure regimes. The feed-gas composition and total flow rate were observed to have smaller effects on both H_2 dissociation and ion flux compared to power and pressure. Consequently, the H_2/Ar ratio was fixed at 50% H_2. This gas composition was selected to increase the total flow available due to limitations of the mass flow controllers (MFC), providing a larger investigated flow range. Reference feed-gas flow was set at 50 sccm, with 20 sccm and 80 sccm as low and high values.

Ultimately, this chapter has three main goals. The first is to provide insight into optimising PE-ALD processing by understanding how controllable plasma parameters

affect film growth and quality. The second is to demonstrate the capability of in-situ PE-ALD monitoring and diagnostics to identify process trends during deposition, enabling a more data-driven approach to process development. The third goal is to explore whether plasma features can be correlated with film properties to establish a foundation for predictive, plasma-informed process control; however, while initial trends are examined, a definitive predictive relationship could not be established within the scope of this work. Nevertheless, the methodology demonstrated here is broadly applicable and can be extended to other plasma chemistries to support more efficient, less trial-and-error-driven optimisation of PE-ALD processes.

5.2 Experimental Details

Copper films were deposited by plasma-enhanced ALD using bis(2,4-pentanedionato)copper ($Cu(acac)_2$, Strem), heated to 138 °C, as the metal precursor and a hydrogen argon plasma as the co-reactant. The plasma feed gas was composed of H_2 and Ar in a fixed ratio of 1:1. Each ALD cycle consisted of a 3 s $Cu(acac)_2$ dose at 40 mTorr, followed by a 5 s Ar purge and a 15 s pump step. The plasma step was applied for 10 s in all cases, after which the chamber was purged with Ar for 5 s and pumped for 5 s before the next cycle. The substrate temperature was maintained at 100 °C.

Films were deposited on Si substrates with native oxide. Prior to deposition, substrates were cleaned in an isopropanol (IPA) sonicated bath for 10 min, dried under N_2 flow, and loaded into the systems load lock. A pretreatment consisting of a 3 min O_2 plasma exposure followed by a 3 min H_2 plasma exposure was performed on all samples, to clean and functionalise the surface. Post-treatment Si 2p XPS measurements indicated a surface oxide thickness of 0.7 nm, determined using the method of Jensen et al[12].

Each experiment comprised of 20 ALD cycles, producing thin copper containing films. Film thickness was calculated via Si 2p signal attenuation in post-deposition XPS, as described in Chapter 2. A uncertainty of 10.2 % was applied to all thicknesses based on element-specific IMFP/EAL error reported by Jablonski et at[13]. After deposition, samples were transferred to the XPS chamber via robotic handling under vacuum. Survey spectra were collected over 1000–0 eV binding energy at 100 eV pass energy. High-resolution spectra of all identified elements were acquired at 50 eV pass energy. All spectra were analysed using CasaXPS software with a Shirley–Sherwood background, where appropriate. Binding energies were referenced to the Si $2p_{3/2}$ peak at 99.4 eV. CasaXPS's built-in Monte Carlo analysis was used to estimate peak-fitting uncertainties by

repeatedly refitting noise-perturbed spectra, providing error estimates that reflect the noise characteristics of the data.

5.3 Results

This chapter presents the experimental results in two main sections. The first section examines the influence of the controlled process parameters on the plasma behaviour. This analysis was performed using in-situ optical OES during the PE-ALD cycles. Plasma stability was assessed using the coefficient of variance of the argon $2p_1$ and the hydrogen Hα Balmer series emission peaks over every ALD cycle. Once the stability was understood, ERA calculations provided a quantitative measure of the two investigated plasma features, local mean electron energy (ε) and degree of H_2 dissociation (r_H). These features were then used to understand the parameters influence on the plasma's behaviour. The second section focuses on film characterisation using in-situ XPS. Variations in film thickness, elemental composition, and chemical bonds are evaluated as a function of the process parameters.

Together, the results build upon the previous chapter to establish a comprehensive understanding of how processing parameters govern both plasma behaviour and film growth during PE-ALD. These findings form the basis for the discussion presented in Section 5.4.

5.3.1 Plasma response to parameter variation

5.3.1.1 Plasma Stability

Throughout each PE-ALD process, OES measurements were recorded every 250 ms. From this data, the emission intensity values of the Hα (656 nm) and Ar $2p_1$ (750 nm) were analysed. The coefficient of variation (CV) was calculated for each process, and the average CV is shown in Figure 5.1 with the standard deviation (σ) represented by the error bars. This metric, as previously stated, provides a normalised measurement of

variability that allows for direct comparison between process conditions. From Chapter 4, it was found that without an ALD environment present, the maximum CV was less than 1 %.

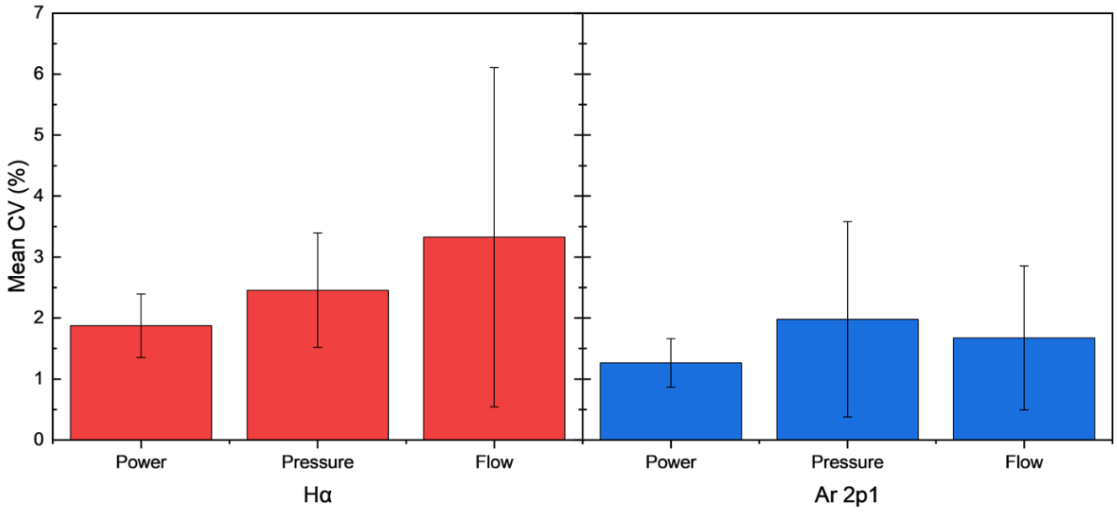


Figure 5.1 - Mean CV of Hα emission (red) and Ar $2p_1$ (blue) emission with error bars representing the standard deviation for process parameters during PE-ALD.

From Figure 5.1, all ALD processes have increased CV values from the pre-ALD investigation discussed in Chapter 4. The stability of the argon emission is impacted less in the ALD environment when compared to the Hα emission. This aligns with the previous chapter's results, where the argon emission had lower CV values. Variations in the ICP power resulted in both the smallest mean CV and standard deviation values for both Hα and Ar emission peaks. Values of 1.9 % ± 0.5 % and 1.3 % ± 0.4 % for Hα and Ar $2p_1$, respectively, in mean CV ± σ were found. Both the pressure and flow variants had significantly increased standard deviations of the same emission peak when compared to power.

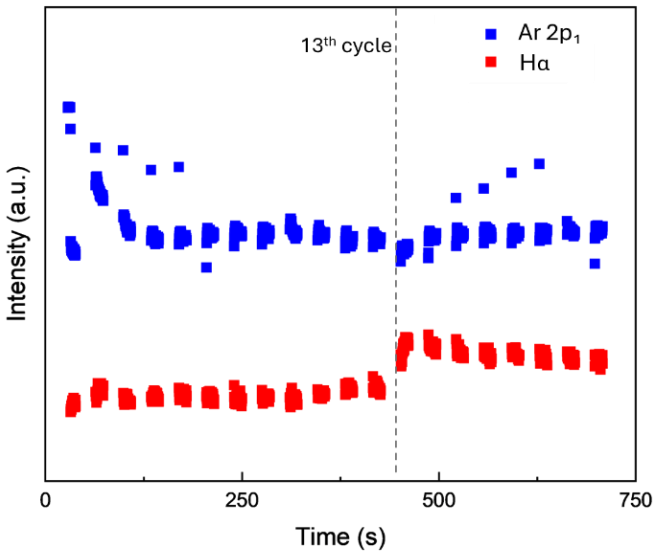


Figure 5.2 - Time resolved OES of low flow PE-ALD process for Hα (red) and Ar $2p_1$ (blue) emission peak.

Further investigation revealed that the standard deviation for flow was disproportionately influenced by the low flow variation with CV values of 7.3 % and 3.3 % for Hα and Ar $2p_1$ emission peaks, respectively. From Figure 5.2 there is a clear increase in the Hα emission from the 13th ALD cycle onwards, suggesting a change in operating conditions. However, no such change was observed in the Ar $2p_1$ emission suggesting it is attributable to the flow of H_2 as opposed to changes in the ICP source. No changes in H_2 flow rate were observable in the process log. From the Ar $2p_1$ emission there is an initial decrease in intensity with increasing cycle number until the process stabilises after approximately 4 cycles. These results could suggest the MFC struggled with low flow rate for H_2. It was also observed that the ALD environment modified the initial plasma's response, as seen by the Ar $2p_1$ emission response.

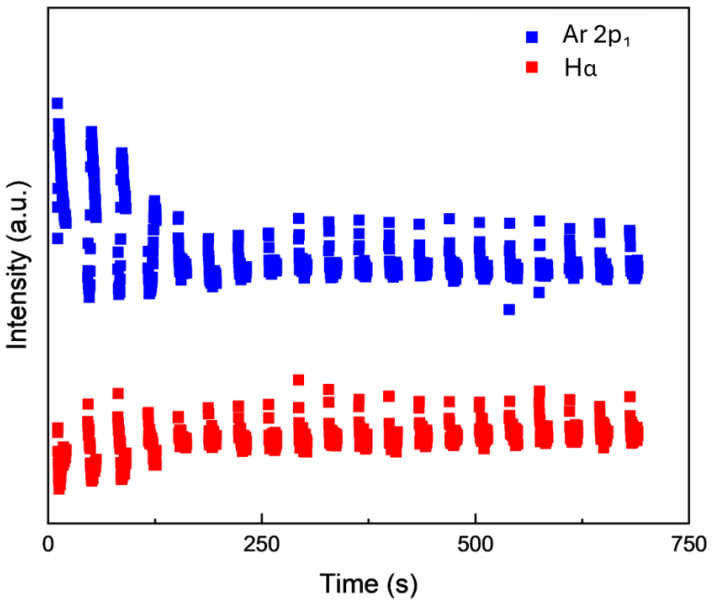


Figure 5.3 - Time resolved OES of low pressure PE-ALD process for Hα (red) and Ar $2p_1$ (blue) emission peak.

The low-pressure variation was also the key influencing process which increased the standard deviation of the CV values seen in Figure 5.1. From Figure 5.3, large variations in both intensities can be seen throughout the process. Isolating cycle 2 and 19 provides further insight into the initial and final stages of the process, which is displayed in Figure 5.4 (a) & (b), respectively. The initial cycles demonstrate an increase in the Ar $2p_1$ intensity around 3 s into the discharge, seen in Figure 5.4 b). This is followed by a slight decrease until the end of the plasma processing time. In the Hα emission, only an initial drop is observed until approximately 5 s into the discharge then a near constant intensity was observed. However, for the later stage cycles, only an initial drop for approximately 1.5 s is observed for both peaks.

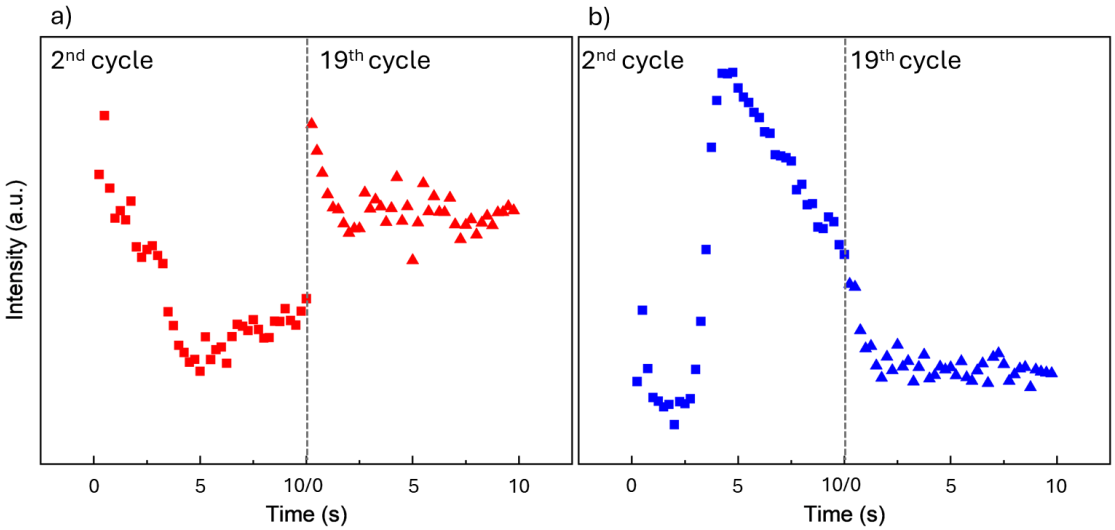


Figure 5.4 - 2nd and 19th ALD cycle time resolved OES spectra for a) Hα (red) and b) Ar $2p_1$ (blue) emission.

Both emission peaks experienced less variation in the later stages of the ALD process, suggesting that early plasma conditions are altered by the ALD environment. Process stabilisation occurs after the first couple of cycles as identified by more consistent emission in the later cycles.

5.3.1.2 Plasma features

The influence of each parameter variation was investigated by systematically changing the condition using the ranges and reference process described above. The local mean electron energy and degree of H_2 dissociation was calculated using the average emission intensities for each process. Due to large systematic errors associated with the excitation cross sections, no error bars from variance in emission are included. This is to avoid misrepresenting the error associated with the ERA calculations. An approximate error of 30 % is associated with all ERA produced values, as discussed in Chapter 2.

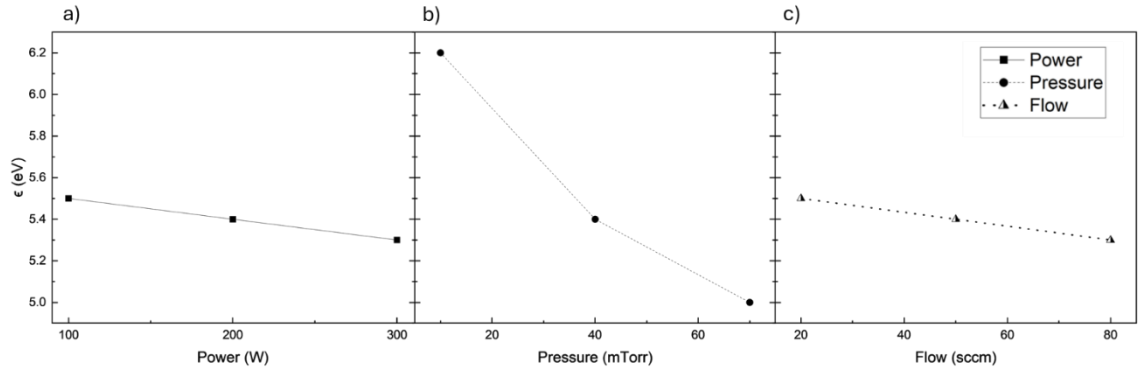


Figure 5.5 - Mean electron energy (eV) as a function of a) ICP Power (W), b) chamber pressure (mTorr) and c) feed-gas flow (sccm) PE-ALD processes.

Figure 5.5 presents the variation in local mean electron energy with changes in ICP power, chamber pressure and feed-gas flow. An increase in power from 100 W to 300 W resulted in a small decrease in the local mean electron energy from approximately 5.5 eV to 5.3 eV, corresponding to a reduction of ~0.1 eV per 100 W increment. A similar trend was observed for changes in feed-gas flow, where an increase from 20 sccm to 80 sccm produced a consistent decrease from 5.5 eV to 5.3 eV in steps of 0.1 eV. These small changes are comparable to the 0.1 eV step size used in the ERA calculation and are not significant relative to the ~30% systematic uncertainty of the method. Variations in the chamber pressure produced a significantly larger change. Increasing the pressure from the low to medium range led to a decrease in the local mean electron energy from 6.2 eV to 5.4 eV, representing a total drop of 0.8 eV. Further increases in pressure resulted in a smaller reduction, with the electron energy reaching approximately 5.0 eV at the highest pressure investigated.

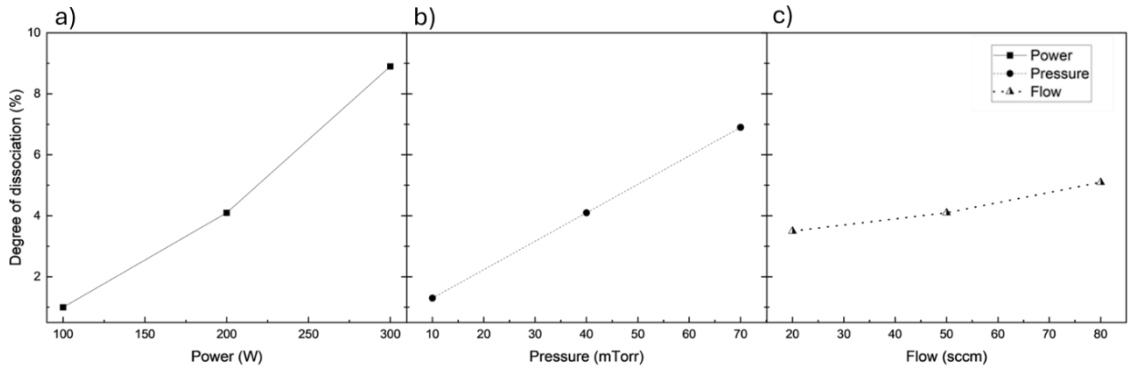


Figure 5.6 - Degree of H_2 dissociation (%) as a function of a) ICP Power (W), b) chamber pressure (mTorr) and c) feed-gas flow (sccm) PE-ALD processes.

From Figure 5.6, all investigated parameters influence the degree of H_2 dissociation. Variations in ICP power had the largest influence on r_H. Increasing power from 100 W to 200 W produced an increase of 3.1 %. Further increasing the power to 300 W resulted in an increase to of 4.8 % to 8.9 %, representing a non-linear relationship between power and r_H. Changes in the flow also produced a non-linear response. 20 sccm to 50 sccm resulted in a 0.6 % increase, while 50 sccm to 80 sccm resulted in an increase of 1 %. The pressure variations produced the only linear response with an increase of 2.8 % for each increase of 30 mTorr. The flow produced the smallest response with only 1.6 % overall change, while pressure produced an overall change of 5.6 % and power resulted in a 7.9 % change in r_H.

In summary, changes in both power and flow had an inverse linear impact on ε, with an overall small change. Increasing the chamber pressure resulted in a larger overall change in ε with a non-linear inverse relationship. A non-linear response occurs in r_H for both changes in flow and power, with a linear response for variations in pressure. r_H appeared to be heavily influenced by power and pressure and only a small change was observed with flow.

5.3.2 Film Characterisation

5.3.2.1 Pre-treatment

After deposition all films were transferred under vacuum to the XPS chamber allowing for quasi in-situ characterisation. Post-O_2 and H_2 plasma pre-treatment XPS measurements, shown in Figure 5.7, reveal that a new peak 531.5 eV appeared in the O 1s measurements after the H_2 plasma pre-treatment.

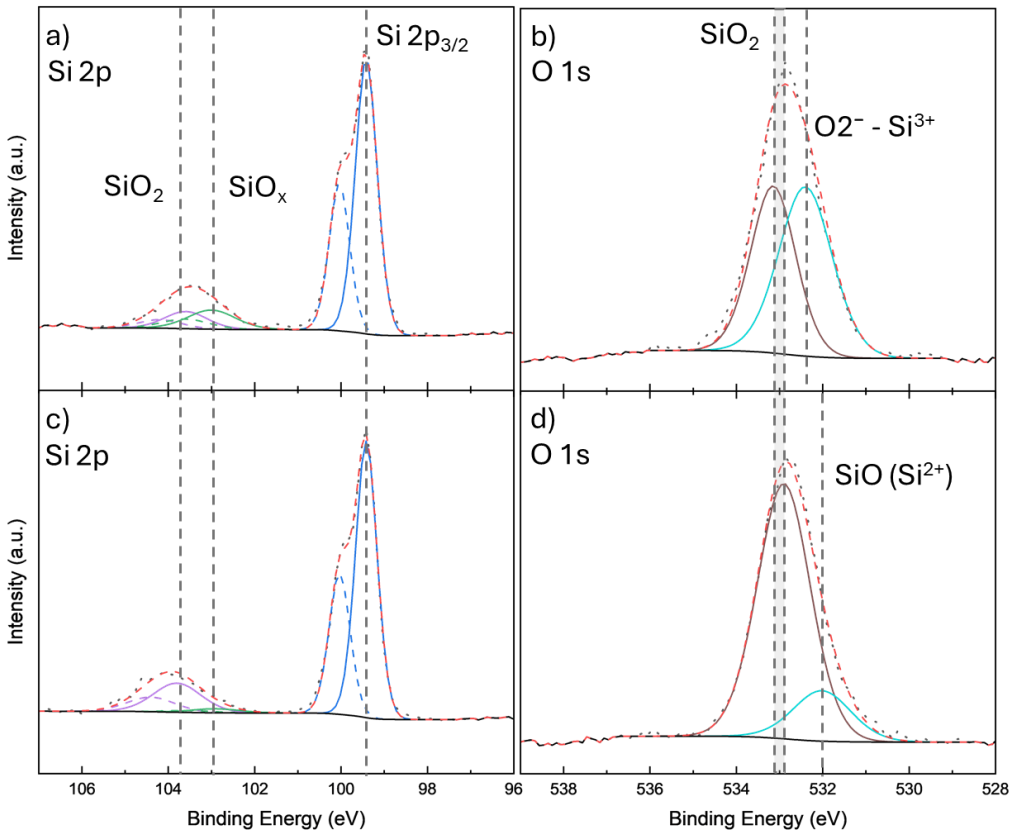


Figure 5.7 - Fitted XPS spectra of the Si 2p a) O_2 and c) H_2 plasma pre-treatment and the O 1s b) O_2 and d) H_2 plasma pre-treatment with $2p_{3/2}$ orbitals represented by solid lines and $2p_{1/2}$ represented by dashed lines.

Figure 5.7 a) shows the Si 2p spectrum following the O_2 plasma pre-treatment. In the high binding energy oxide region, multiple components are present including SiO_2 at 103.6 eV and sub-oxide SiO_x at 103 eV[14], along with their corresponding $2p_{1/2}$ spin orbital components. The overall fit yields 78.7 ± 0.7 % Si^0, 11.1 ± 2.2 % SiO_x and 10.2 ± 1.9 % SiO_2. In Figure 5.7 b), the O 1s region contains two components at 533.1 eV (SiO_2) and 532.3 eV (SiO_x). The oxide contributions are 45.5 ± 0.5 % SiO_2 and 54.5 ± 0.5 % SiO_x, consistent with the sub-oxide fraction obtained in the Si 2p region.

Following the H_2 plasma pre-treatment, Figure 5.7 c) shows a significant change in the Si 2p oxide region. The sub-oxide contribution drops to 2.4 ± 0.5 % and the SiO_2 fraction increases to 18.4 ± 0.6 %. This indicates effective passivation of defect sites. Additionally, the O 1s spectrum becomes dominated by the SiO_2 component (82.7 ± 0.8 %), with only 17.3 ± 0.8 % attributed to the lower binding energy sub-oxide species. A 0.5 eV decrease in the sub-oxide component suggests a lowering in the oxidation state, consistent with a transition from Si^{3+} to Si^{2+}.

Overall, the O_2 plasma aggressively interacts with the ultrathin native oxide and generates substantial Si sub-oxide states. The H_2 plasma passivates local disorder in the Si matrix and oxygen-deficiencies. This effectively eliminates most sub-oxide species leaving a Si^{4+} rich surface. However, a small sub-oxide population remains and such species have been identified as potential reactive surface sites relevant for nucleation in $Cu(acac)_2$ PE-ALD.[15,16]

5.3.2.2 Film overview

Survey scans were utilised for elemental identification, composition and thickness, which was calculated from the attenuated Si 2p signal, as described in Chapter 2. The "Reference" process corresponds to 200 W plasma power, 40 mTorr pressure, and 50

sccm precursor flow. Table 5.1, below, summarises the survey composition measurements.

Table 5.1 - XPS determined film composition and thickness for each investigated 20-cycle PE-ALD process.

Process	Si2p (%)	O1s (%)	C1s (%)	Cu2p (%)	Thickness (Å)
Reference	57.7	31.6	5.1	5.6	5.0 ± 0.5
100 W	61.7	31.3	3.9	3.1	3.1 ± 0.3
300 W	51.5	28.8	8.3	11.4	8.3 ± 0.8
10 mTorr	54.5	30	7.7	7.8	6.7 ± 0.7
70 mTorr	59.8	31.4	4.7	4.1	4.0 ± 0.4
20 sccm	51.18	29.2	8.2	11.4	8.5 ± 0.9
80 sccm	53.6	30.5	6.7	9.2	7.2 ± 0.7

From Table 5.1 it is clear there is a significant change in both film composition and thickness as a direct result of parameter variation. The thickness values have a range of 3.1 ± 0.3 - 8.5 ± 0. Å, corresponding to a GPC range of approximately 0.16 ± to 0.43 Å/cycle. This represents nearly an x3 increase in the film growth between lowest and highest growth, demonstrating the critical nature of the plasma to the growth process. It is important to note that thickness calculations assume a homogenous sample and the presence of non-continuous layers can impact the calculated values.

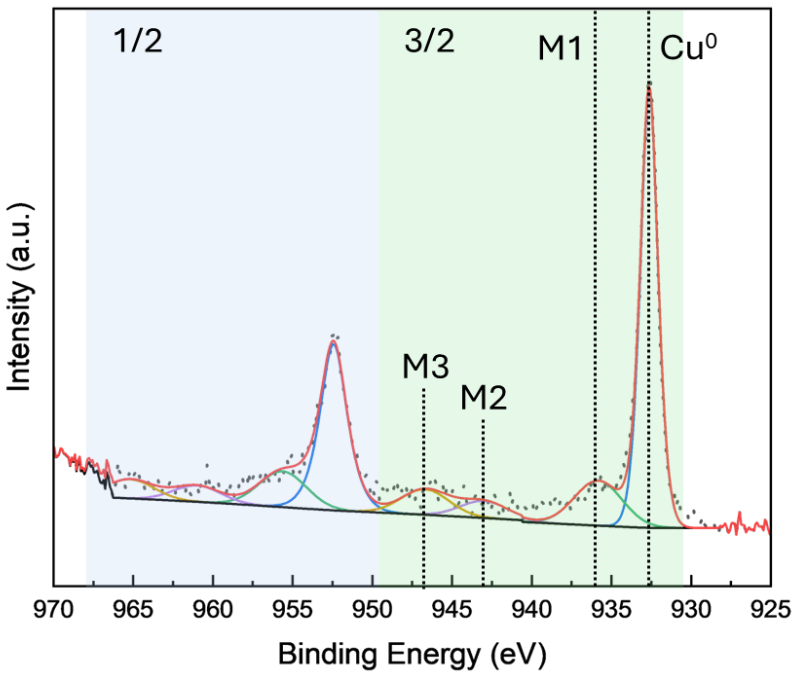


Figure 5.8 - Cu 2p XPS spectra fitted according to Torres-Ochoa et al[17].

A key requirement for Cu PE-ALD processing is the deposition of Cu^0. XPS provides a valuable insight into the chemical state of the film which will be explored in the following section. Figure 5.8 presents the fitted reference process Cu 2p XPS spectra. A clear peak is present at 932.6 eV[18], which is typically assigned to Cu^0. However, the Cu $2p_{3/2}$ peak can also contain Cu^{1+} (Cu_2O) at 932.4 eV[18] and Cu^{2+} (CuO_2) at 933.6 eV[18]. Two additional steps can be undertaken to confirm the presence of Cu^0. Cu^{2+} can easily be identified by characteristic satellite peaks located approximately around 940-945 eV range[19]. As no such feature exists in any of the collected data, represented here by the reference process in Figure 5.8, the deposited Cu is confirmed to either be Cu^0 or Cu^{1+}. To differentiate between these chemical states a Wagner plot can be used[20]. A Wagner plot is interpreted by comparing a sample's core-level binding energy (BE) with its corresponding Auger peak kinetic energy (KE). Each oxidation state produces a distinct BE-Auger KE pair that allows the chemical state to be identified. By utilising the LMM auger peak of Cu located

around 915-920 eV kinetic energy combined with the Cu $2p_{3/2}$ peak in binding energy a Wagner plot can be produced[21].

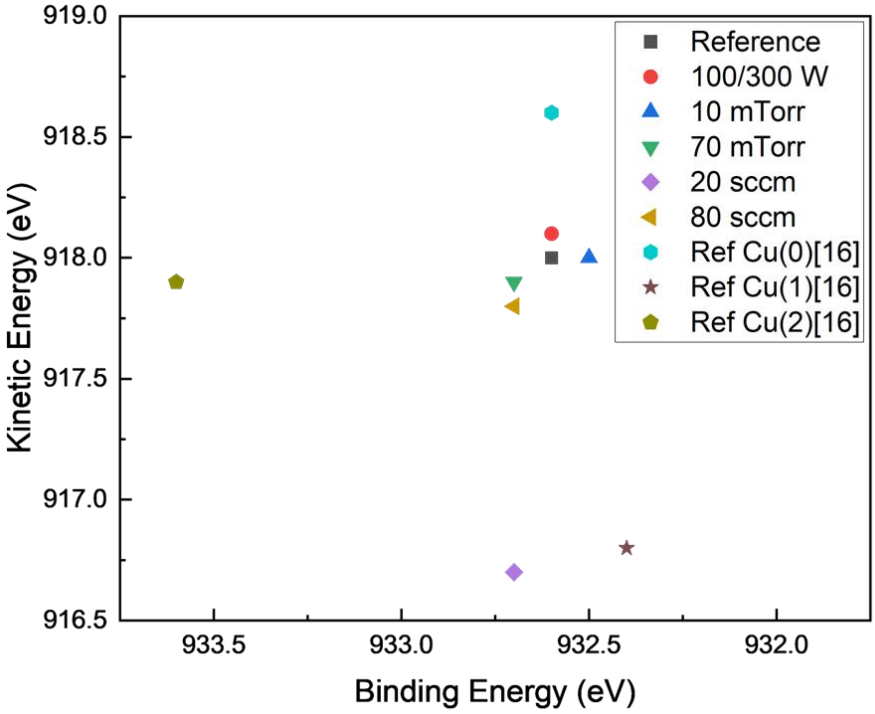


Figure 5.9 - Wagner plot of Cu XPS data for ALD processes and reference $Cu^{0\text{-}2+}$ states gathered from Biesinger et al[19].

From Figure 5.9 it can be seen that, except for the low flow, all films are found to contain primarily Cu^0 with some Cu^{1+} content. However, the low flow is primarily Cu^{1+}. Changes in the power resulted in little overall positional movement for either peak. Increasing the pressure resulted in a general increase in the Cu 2p binding energy suggesting an increased contribution of higher oxidation states. The largest change was observed for variations of the flow. Low flow suggested mostly Cu^{1+} state was present. Increases in flow resulted in a shift to primarily Cu^0.

5.3.2.3 Benchmark XPS analysis

All Cu 2p spectra were fitted following the method described by Torres-Ochoa et al[17]. In this approach, the composition of the Cu 2p peak is determined through simultaneous fitting of the $2p_{3/2}$ and $2p_{1/2}$ components, using a Tougaard background. The Lorentzian contribution to the main 2p ½ peak provides insight into the Cu^0/Cu^{1+} composition of the signal, as described by Torres-Ochoa et al. A linear relationship was previously established between the Lorentzian width and oxidation state, where a 1.3 eV Lorentzian corresponds to Cu^{1+} and 1.0 eV corresponds to Cu^0.

Using this method, the reference process Cu 2p spectra was fitted, and the peak contributions (M1–M3) were identified (Figure 5.8). To determine the dominant chemical state, all peak positions were fixed, and the Lorentzian width of the Cu $2p_{1/2}$ main peak was varied between 1.0 and 1.3 eV. The standard deviation of the residual was recorded for each fit. A linear decrease in the residual was observed as the Lorentzian approached 1.0 eV, indicating that the peak is primarily composed of metallic Cu, consistent with the Wager plot.

However, the Lorentzian-based fitting suggested a fully metallic composition, which is unlikely due to the presence of the M1–M3 peaks and the Wagner plot indicating a mixed Cu^0/Cu^{1+} states. It was therefore concluded that a small amount of Cu^{1+} is present, although its absolute fraction cannot be accurately quantified through the Cu 2p region alone. This uncertainty arises from the low signal intensity (Cu 2p represents <10% of the total film composition) and the broader full width half max (FWHM) associated with the 50 eV pass energy used, compared with the 10 eV used by Torres-Ochoa et al.

Due to low counts, it was not possible to always accurately fit the C 1s region. Survey measurements provide information on the composition of carbon within the film. For the

reference process, there is a clear peak located around 285 eV which is attributed to C-C bonding, representing partially removed or fragmented precursor ligands. Without a higher signal-to-noise ratio, further analysis remains difficult. By comparing variations of the parameters more information can be gathered.

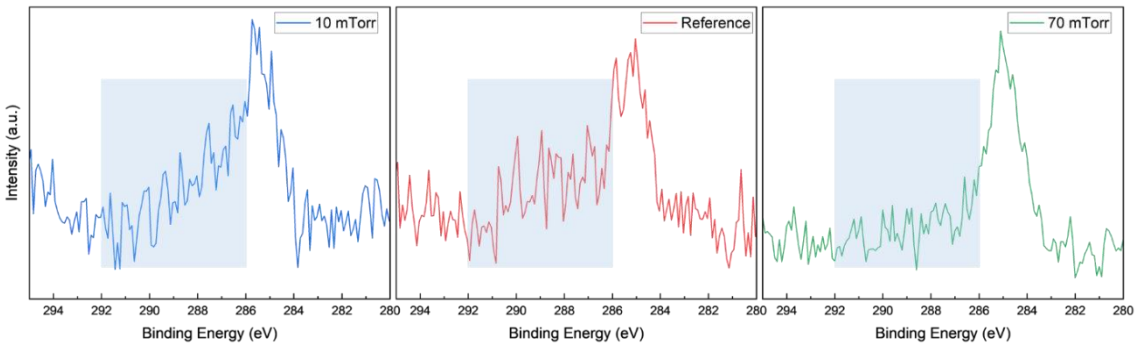


Figure 5.10- Pressure variations (10 mTorr (blue), 40 mTorr (red) and 70 mTorr (green)) influence on C 1s XPS spectra, with high binding energy area highlighted.

Figure 5.10 presents the variation of pressure on the C 1s peak. As pressure increases there is a general increasing in the high binding energy shoulder (blue shaded area) of the main C 1s peak. The higher binding energy region is associated with carbon-oxygen bonding. The relative increase in C–O compared with C–C bonding suggests higher levels of incomplete ligand removal with increasing pressure. While direct measurement and analysis of the C 1s peaks remains difficult, relative trends can be identified between processes.

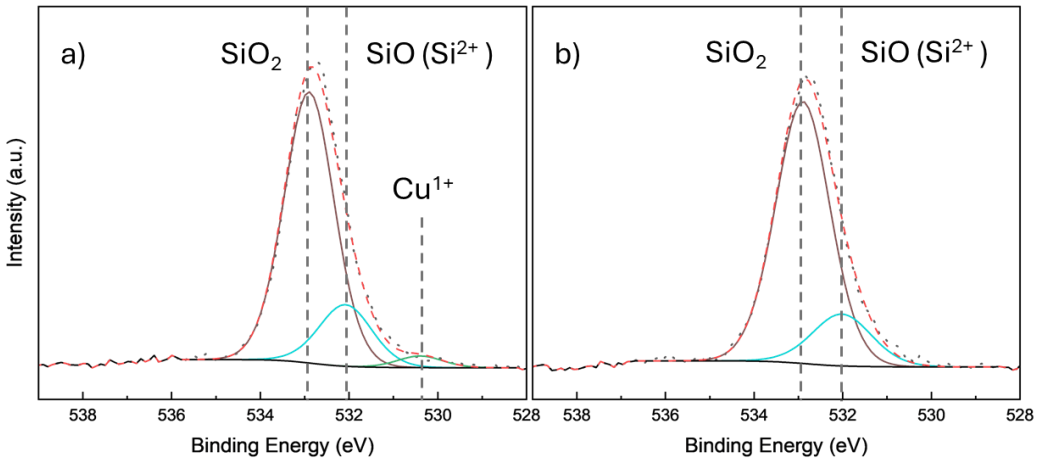


Figure 5.7 - O 1s fit for a) Reference PE-ALD process and b) H_2 plasma pre-treatment.

Figure 5.11 shows the fitted O 1s region of the reference process. A similar SiO_2 and Si^{2+} contribution was identified. However, after the PE-ALD process a low binding energy peak at 530.4 eV was identified. This is associated with Cu^{1+} and its overall contribution to the fit was 2.7 ± 0.7 %. Considering the O 1s content (%) from the survey spectra of 31.6 %, the Cu^{1+} contribution was found to be 0.9 ± 0.2 % of the overall film. The Cu 2p content was calculated to be 5.6 % suggesting a Cu^0 composition of approximately 4.7 ± 0.2 %. These results align with the previously estimated small Cu^{1+} contribution for the earlier Cu 2p work.

The overall elemental composition of the reference process film was 57.7 % Si 2p, 31.6 % O 1s, 5.1 % Cu 2p, and 5.6 % C 1s. From the fitted Cu 2p region, the film was identified to mainly consisted of Cu^0 with minor Cu^{1+} contributions. This was then confirmed by O 1s fittings. The C 1s appeared dominated by C-C bonding with some C-O contributions. The Si 2p remained approximately unchanged except for a minor decrease in Si^0 which is associated with attenuation due to the overlayer growth. The XPS analysis demonstrated that reliable fitting is achievable when count rates are sufficiently high,

whereas lower count rates limit quantitative accuracy but still enable qualitative comparisons. The same fitting and analysis procedure was applied to all process films to ensure consistent evaluation of film chemistry and growth behaviour.

5.3.2.4 Influence of process parameter variation on film properties

Variations in plasma power produced the most significant changes in the resulting film thickness. The lowest power (100 W) generated the thinnest film at 3.1 ± 0.3 Å, while the highest power (300 W) produced one of the thickest films at 8.3 ± 0.8 Å. As shown in Figure 5.12 (a), the relationship between film thickness and plasma power is near linear, with a slight increase in growth between the 200 W and 300 W processes when compared to the 100 W and 200 W process.

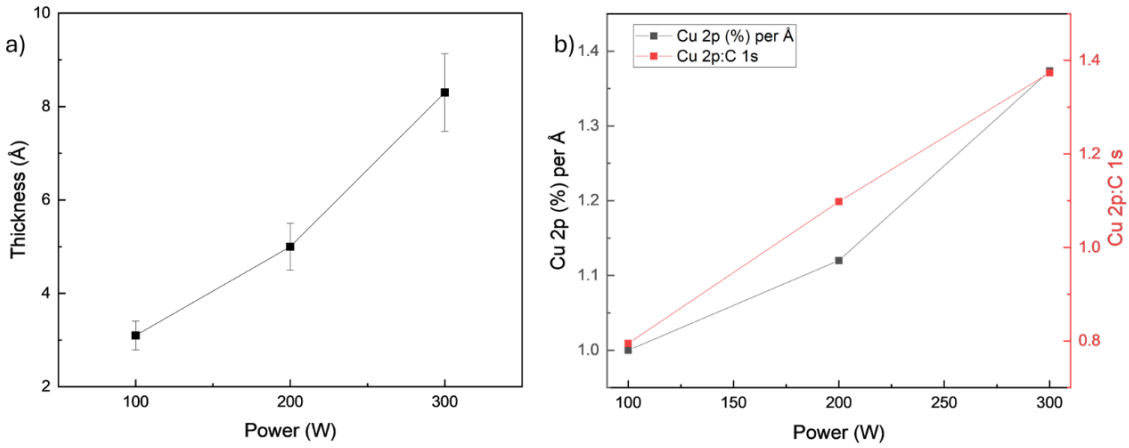


Figure 5.8 - a) Film thickness (Å) with estimated error from EAL calculation[13] and b) Cu 2p (%) per Å (black) and Cu 2p:C 1s ratio (red) vs ICP power (W).

A linear relationship was observed between the Cu 2p:C 1s ratio and power, as seen in Figure 5.12 (b). This ratio provides an insight into the plasmas ability to successfully

remove precursor ligands. Higher power provides an increased probability of ligand removing interactions between plasma species and the substrate surface.

The Cu 2p (%) per Å was found to increase with a near linear trend with power. This provides additional insight into the films growth as it demonstrates that the films thickness correlates with the increased Cu 2p:C 1s ratio. Improved growth per cycle is directly related to additional active surface sites which are available because of more successful ligand removal.

In summary, increasing the plasma power enhances film growth by improving ligand removal efficiency. This results in a higher concentration of active surface sites for subsequent ALD cycles and contributes to improved film purity, both through increased removal of C.

Changes in pressure produced film thicknesses ranging from 4.0 ± 0.4 Å to 6.7 ± 0.7 Å, with lower pressures yielding thicker films. The thickness decreased by approximately 1.7 Å when the pressure increased from 10 to 40 mTorr, followed by an additional reduction of roughly 1 Å between 40 and 70 mTorr, indicating that the most significant plasma-related effects occur in the low to medium pressure regime.

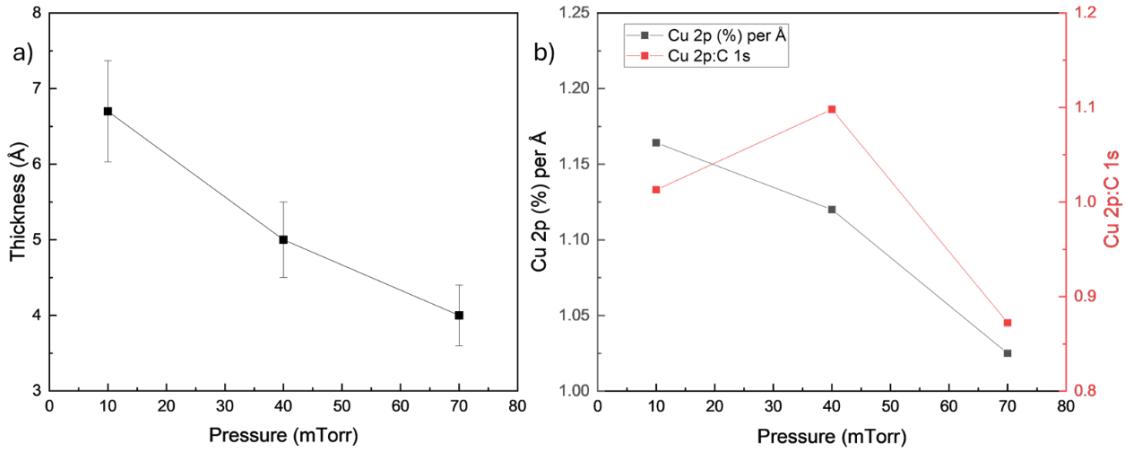


Figure 5.9 - a) Film thickness (Å) with estimated error from EAL calculation[13] and b) Cu 2p (%) per Å (black) and Cu 2p:C 1s ratio (red) vs Pressure (mTorr).

The Cu 2p (%) per Å was examined to assess the Cu incorporation. Increasing the pressure reduced this value. Lower film thickness corresponds to a reduced GPC, which indicates fewer active surface sites during each ALD cycle. With fewer active sites, more precursor ligands remain unreacted within the film, leading to a lower relative Cu content within the same thickness.

To further evaluate film purity, the Cu 2p:C 1s ratio was calculated. At 10 mTorr, the ratio was ~1. Increasing the pressure to 40 mTorr improved the film purity, yielding a ratio of 1.1. However, further increasing the pressure led to a decrease in the Cu 2p:C 1s ratio to just below 0.9, indicating that the highest-pressure condition had the poorest ligand-removal efficiency. The improvement observed at 40 mTorr suggests that this pressure regime generates reactive species that most effectively remove ligands, leading to the lowest impurity levels within the film. However, the process still exhibits a reduced GPC, indicating that additional factors limit the overall efficiency of growth. This explains the lower Cu 2p (%) per Å measured under these conditions. In summary, increasing the pressure resulted in thinner films with higher levels of unremoved ligands. The highest

overall purity was achieved at 40 mTorr. However, this condition also exhibited a reduced GPC and an increased Cu^{1+} content.

The flow displayed some non-linear trends for thickness. The low flow, 20 sccm process, produced the thickest film overall at 8.5 ± 0.9 Å. A significant drop to 5.0 ± 0.5 Å was then found at 50 sccm. The film thickness then increased with a flow of 80 sccm, to 7.2 ± 0.7 Å.

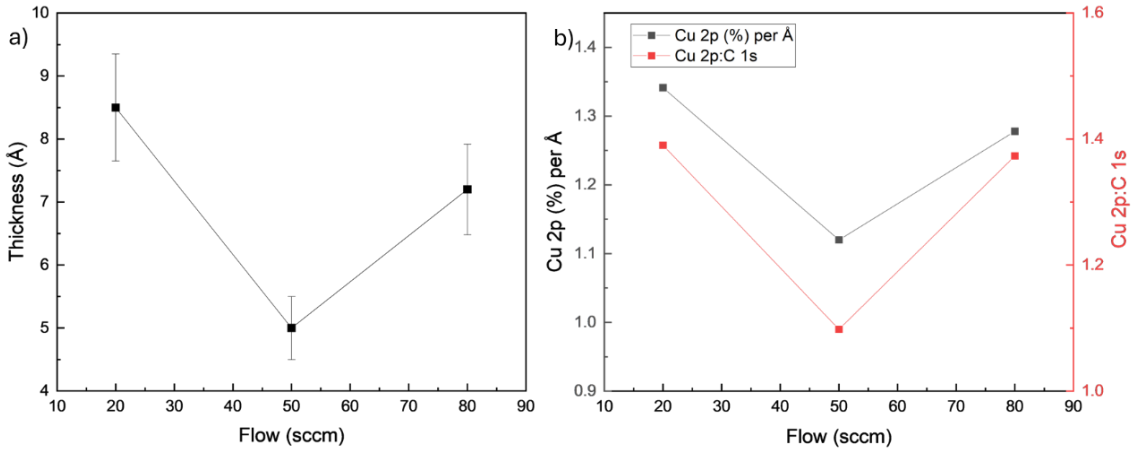


Figure 5.10 - a) Film thickness (Å) with estimated error from EAL calculation[13] and b) Cu 2p (%) per Å (black) and Cu 2p:C 1s ratio (red) vs Flow (sccm).

This trend was also observed in both the Cu 2p (%) per Å and Cu 2p:C 1s values, with the 50 sccm flow resulting in the lowest value. The Cu 2p (%) per Å had approximate values of 1.3, 1.1 and 1.3, while the Cu 2p:C 1s had values of 1.4, 1.1 and 1.4 for 20, 50 and 80 sccm, respectively.

The low flow process produced the only film with most of the Cu in an oxidated state (Cu^{1+}) as identified from the Wagner plot. 50 sccm flow had the most metallic film then the 80 sccm had increased Cu^{1+} contribution but still a majority Cu^{0}.

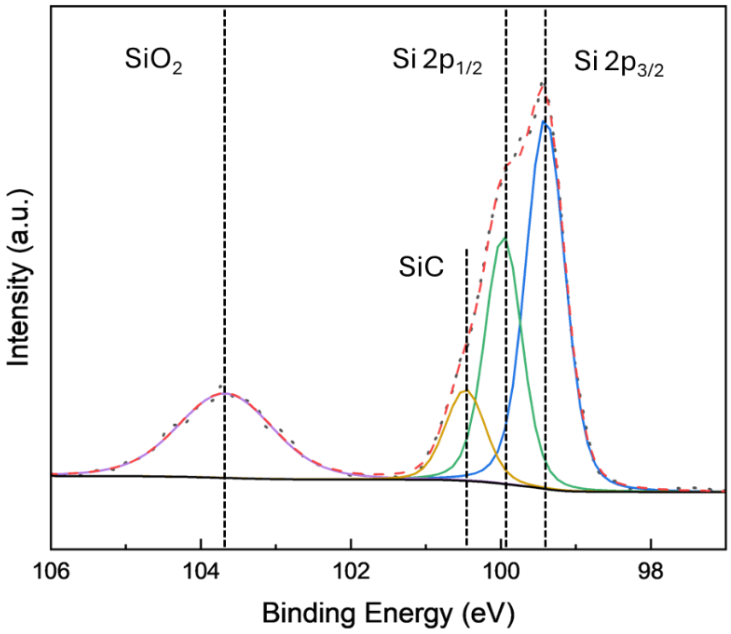


Figure 5.11 - Fitted Si 2p XPS spectra of the 20 sccm PE-ALD process.

Analysis of the Si 2p spectra revealed key differences between the low-flow process and all other processes. The 20 sccm process was found to have an additional peak located around 100.4 eV, which is associated with SiC[18]. This suggests the reduced flow allowed for more radical generation which degraded the surface SiO_2 layer, allowing ligand by-products to react with Si. This explains the increased Cu^{1+} content observed in the Wagner plot as the excess oxygen produced as a by-product can be integrated into the film.

Overall, the low flow was found to impact the surface by producing Si-C bonding. This increased Cu^{1+} incorporation into the film from the oxygen by-products. However, 20 sccm was also found to have the highest thickness, Cu 2p:C 1s and Cu 2p (%) per Å valves suggesting after the initial growth, the low flow produced high quality films with high GPC. This could be attributed to the increased radical energy demonstrated by the initial surface interactions. 50 sccm was shown to have the worse overall properties out

of the investigated flows while the high flow, 80 sccm, improved thickness, Cu 2p (%) per Å and Cu 2p:C 1s ratio.

5.4 Discussion

5.4.1 Impact of ALD environment on plasma behaviour

From the results of Chapter 3 along with previous published work on PE-ALD[23–25], it was shown that the ALD environment can significantly alter the plasma's response. The pre-ALD plasma characterisation performed in Chapter 4 provides insight into the response without the influence of the ALD environment allowing for comparison with the current results.

In the current work, there was a general increase in ε during PE-ALD processing of approximately 1 eV. The feed-gas composition was reduced from 80 % H_2 for pre-ALD processes to 50 % H_2 ALD processes. Jiménez-Redondo et al demonstrated an increase can be directly attributed to this change in gas composition[26]. Results from Chapter 4 showed a change from 50 % to 80 % H_2 gas composition resulted in 1 eV reduction of the mean electron energy.

The previous trend of a non-linear relationship between power and ε are not observed in the ALD environment. Decreased H_2 composition pushes the EEDF into a more Druyvesteyn-like distribution[27]. As discussed in Chapter 4 (Figure 4.9), this distribution is characterised by a relatively depleted high-energy tail. The reduced H_2 content also decreased the number of vibrational states available, limiting vibrational cooling of the electrons[26]. As a result, there is an increase in the general ε, along with a change in the plasma's response to power. A linear relationship between ε and flow was maintained in the ALD processes. Only a change in the general ε was observed, which is attributed to the change in the gas composition. The non-linear relationship between pressure and the mean electron energy was also retained during the ALD processes. An increase in the overall drop from 0.6 eV (pre-ALD) to 1.2 eV (during ALD) was observed. In the more

Druyvesteyn-like distribution, increases in collisions, due to increased pressure, impacts the high energy tail more significantly to its reduced density. As a result, a more significant reduction in ε is observed.

Increasing all parameters results in an increase in the degree of H_2 dissociation in the ALD processes. In general, the observed trends from the pre-ALD investigation remained. A slight deviation from linear is observed with increasing power. The shift to a more Druyvesteyn distribution from the reduced H_2 results in a reduction in the high energy tail density, as typical of this distribution. This is likely to disproportionately impact the low power process where there is lower overall electron densities[28] and as a result H_2 dissociative collisions decrease in probability. There was a noticeable decrease in the overall r_H. Low power produced similar r_H at approximately 1%, while 200 W only produced 4.1 % in-process compared to the previous 7 %. 300 W shows a similar level of reduction, only producing 8.9 % compared to the pre-ALD's 11.5 %. Pre-ALD analysis determined a reduction of approximately 1 % r_H when reducing H_2 content from 80 % to 50 %. This suggests that the ALD environment influences the production of atomic hydrogen. Additional species, because of the new environment, provide additional quenching and collisional partners. This can reduce the overall H_2 dissociation efficiency of the plasma. Previous discussion in Chapter 3 demonstrated that the ALD environment often impacts the production and excitation of species[23–25].

The increased pressure resulted in a linear response in r_H. The maximum pressure remained below the dynamic equilibrium of base H_2 density vs collisional quenching, as previously seen around 60-70 mTorr in Chapter 4. This resulted in no observable drop in r_H with increasing pressure. It was found that there was a more extreme relationship between pressure and r_H in the ALD enviroment. Pre-ALD measurement demonstrated a change from 4.2 to 6 % r_H with pressure change of 10 – 70 mTorr. The current results

show a wider range of 1.3 to 6.9 % r_H for the same pressure change. The highest degree of dissociation remains similar. However, the significant change in the low-pressure processes suggest a more significant impact from the ALD environment at lower chamber pressures. Pressure is maintained via an automated butterfly valve. With the addition of reaction by-products adding to the pressure, the butterfly valve is forced to open more to maintain the requested pressure. This can reduce the overall residence time of feed-gas in the source when compared to pre-ALD processing, reducing the probability of dissociation[29].

The same trends from pre-ALD and in-process diagnostics were found for flow. Similar r_H values were found for the low and medium flow processes, when the 1 % change due to gas composition was accounted for. No pre-ALD high flow diagnostics was achieved due to the limitation of the H_2 MFC.

In summary, the generally trends observed for ε and r_H were preserved between pre-ALD and in-process diagnostics. There was an overall increase in all ε which was attributed to the gas composition change based on the discussion from Chapter 4. Relationship changes with ε for both power and pressure were determined to be a result of EEDF changes and limits in the investigated parameter range. Small changes in r_H, ~ 1 % are attributable to the change in gas composition, but larger changes identified in power and pressure were identified as impacts of the ALD environment.

5.4.2 Influence of plasma parameters on film properties

The variations in controlled parameters produced significant changes in the deposited films. It was found that there was an approximate x3 increase in the film thickness

between the lowest and highest GPC process. Along with thickness, the Cu 2p:C 1s ratio and Cu 2p (%) per Å are discussed as key film properties in the following section.

Zhang et al[30] demonstrated increased power for AlN PE-ALD resulted in improved GPC. Yoon et al[31] also showed the higher power lead to improved density. Further discussion on these works is available in Chapter 3. In the current work, all investigated film properties improved with increased ICP power. A similar trend in enhanced r_H was identified with increased power. As previously discussed in Chapter 4, this plasma response is critical for precursor reduction. Wu et al[9] demonstrated the critical nature of atomic hydrogen in the $Cu(acac)_2 + H_2$ PE-ALD process, when the precursor was exposed to only H_2 gas, no growth was observed. Increasing the plasmas H_2 dissociating efficiency produces more atomic hydrogen, which improved precursor ligand removal. This is demonstrated by the improved GPC, which directly related to the density of active surface sites, along with the improved Cu 2p:C 1s ratio, which suggests more ligand removal.

Increased pressure had the inverse effect of power. There was a reduction in film thickness, Cu 2p content and Cu 2p (%) per Å. Increased pressure lead to higher r_H which follows trends observed by Iordanova et al [32] in a H_2/Ar discharge when increasing pressure from 7.5 – 45 mTorr. However, as previously established using the pre-ALD ion flux measurements, increased pressure significantly reduces the MFP resulting in collisional quenching and ultimately a large reduction of reactive species flux at the substrate surface[33,34]. In the current PE-ALD set up with the remote ICP source, increased pressure ultimately reduces film properties as a result in limited surface reactions from the lowered MFP despite the increased atomic hydrogen density.

Variations in feed-gas flow represented the only non-linear trend for the film's properties. Both pre-ALD and ALD in-situ plasma diagnostics measurements identified linear trends

in both ε and r_H for all variations in flow. Doh et al[35] showed the gas dependence of ion current density. The response from atomic and molecular feed-gas varied with high flow producing high ion current density for atomic species but low for molecular and an inversed response for low flow. The feed-gas composition used in this work was 1:1 for H_2:Ar. The current investigation suggests that the low flow could primarily produce highly reducing reactive species from the molecular H_2 gas, which resulted in surface SiO_2 reordering or damage as demonstrated by the SiC bonding present on in the low flow variation. Increasing the flow to 50 sccm was shown to improve the r_H but competition with increased reactive Ar species results in increased ligand fragmentation. The film thickness along with both decreased Cu 2p:C 1s ratio and Cu 2p (%) per Å shows increased ligand incorporation within the film. Finally, at 80 sccm there is a further increase in r_H which appears to out compete the reactive Ar species in complete ligand removal as suggested by the improved film properties.

In summary, the results show the significant influence of the controlled parameters on the corresponding film properties. The results align with both previously established published work and the results presented in Chapter 3, suggesting a generalisation of plasma influence on PE-ALD process independent of the precursor and plasma combination. Higher power led to improved reactive species densities resulting in improved film properties. Increasing the pressure was shown to improve the atomic hydrogen density, over the investigated range. However, reactive species transport was negatively affected due to increased collisional quenching. The feed-gas investigation procedure showed the only non-linear relationship with the film properties. Both high and low flow improved complete ligand removal.

5.4.3 Correlation of plasma features with film properties

Several functional forms were investigated to determine correlation between the calculated plasmas features, ε and r_H, with measured film properties, film thickness, Cu 2p:C 1s ratio and Cu 2p (%) per Å. The functional forms included linear, logarithmic, exponential and power-law models. No correlation produced an R^2 value above 0.5, which corresponds to an association which explains half the variance and falls into Hair's second category of moderate [36]. Additionally, no R^2 value 0.5 or greater was found for Hα or Ar $2p_1$ emission intensities.

The result contrasts with previous findings from Chapter 3, where a strong correlation was identified when pre-ALD plasma diagnostics were used to determine the process parameters. The difference is likely a result of the parameter selected. In Chapter 3, pre-ALD diagnostics was used to determine the optimal processes and large variations of parameter values were used to investigate the influence of pressure and flow. In the current work, pre-ALD only provided information on the plasma's response and was not used to optimise the process, only used for comparison with the plasma used in ALD processing.

Various process parameter sets produced similar plasma features but produced different film properties. For example, both high power and pressure produced similar ε and the r_H were the highest out of all investigated processes. However, high power produced significantly improved films in both thickness (8.3 ±0.8 Å vs 4 ± 0.4 Å) and quality. Pre-ALD diagnostics allowed for insight into the processing difference with ~ 2.4 times the ion flux for the high power process, suggesting a significant increase in reactive species at the substrate surface which is realised in processing.

The presented results demonstrate that while ε and r_H provide meaningful information about the plasma's response to the parameters and environment, they are not sufficient on their own to predict film properties. Due to the nature of PE-ALD where many factors play significant roles, additional diagnostics must be utilised for a predictive model. This demonstrated the added benefit of pre-ALD diagnostics. Findings can be utilised to guide process optimisation, as shown in Chapter 3, along with providing a critical insight into the plasma's response. This work has demonstrated that, although the ALD environment influences the plasma's behaviour, the trends observed in pre-ALD investigations are maintained. In-situ diagnostics are then used to both confirm trends are maintained along with providing valuable information on plasma stability to ensure reliable processing.

5.5 Conclusion

This chapter investigated the use of optical emission spectroscopy (OES) as an in-situ plasma diagnostics method during PE-ALD processing of copper thin films using $Cu(acac)_2$ and H_2/Ar plasmas. The results showed that the overall trends in plasma behaviour remained consistent with the pre-ALD measurements presented in earlier chapters. Variations in process parameters could be interpreted using both published literature and previous findings.

A key aim of the chapter was to determine whether the calculated plasma features, ε and r_H could be correlated with film properties to enable a predictive model. This objective was not achieved as each individual features produced no correlations using any tested functional form. The complex nature of PE-ALD, involving many reactions and plasma–surface interactions, means that additional diagnostics or a broader dataset would be required for a reliable predictive model. However, the ERA features provided a robust and quantitative method for in-situ plasma analysis and comparison with pre-ALD plasma.

The work demonstrated that a comprehensive pre-ALD plasma diagnostic investigation is importance for guiding process optimisation. When combined with in situ plasma monitoring changes in the plasma behaviour can be identified and understood. The following chapter applies these insights by examining a set of experiments where plasma instability resulted in non-repeatable ALD growth and film properties. The case-study highlights the importance of integrating both pre-ALD and active in-situ monitoring for producing reliable and repeatable PE-ALD processing.

5.6 References

(1) Kim, H.-W. Recent Trends in Copper Metallization. *Electronics* **2022**, *11* (18), 2914. https://doi.org/10.3390/electronics11182914.

(2) Gao, Z.; Zhang, C.; Gao, J.; Wang, Q.; Xu, G.; Cao, H.; Zhang, H. Nucleation and Growth of Low Resistivity Copper Thin Films on Polyimide Substrates by Low-Temperature Atomic Layer Deposition. *Appl. Surf. Sci.* **2023**, *638*, 158072. https://doi.org/10.1016/j.apsusc.2023.158072.

(3) Raab, S. J.; Guschlbauer, R.; Lodes, M. A.; Körner, C. Thermal and Electrical Conductivity of 99.9% Pure Copper Processed via Selective Electron Beam Melting. *Adv. Eng. Mater.* **2016**, *18* (9), 1661–1666. https://doi.org/10.1002/adem.201600078.

(4) Guo, Z.; Li, H.; Chen, Q.; Sang, L.; Yang, L.; Liu, Z.; Wang, X. Low-Temperature Atomic Layer Deposition of High Purity, Smooth, Low Resistivity Copper Films by Using Amidinate Precursor and Hydrogen Plasma. *Chem. Mater.* **2015**, *27* (17), 5988–5996. https://doi.org/10.1021/acs.chemmater.5b02137.

(5) Moon, D.-Y.; Han, D.-S.; Shin, S.-Y.; Park, J.-W.; Kim, B. M.; Kim, J. H. Effects of the Substrate Temperature on the Cu Seed Layer Formed Using Atomic Layer Deposition. *Thin Solid Films* **2011**, *519* (11), 3636–3640. https://doi.org/10.1016/j.tsf.2011.01.346.

(6) Jezewski, C.; Lanford, W. A.; Wiegand, C. J.; Singh, J. P.; Wang, P.-I.; Senkevich, J. J.; Lu, T.-M. Inductively Coupled Hydrogen Plasma-Assisted Cu ALD on Metallic and Dielectric Surfaces. *J. Electrochem. Soc.* **2005**, *152* (2), C60. https://doi.org/10.1149/1.1850340.

(7) Gordon, P. G.; Kurek, A.; Barry, S. T. Trends in Copper Precursor Development for CVD and ALD Applications. *ECS J. Solid State Sci. Technol.* **2015**, *4* (1), N3188–N3197. https://doi.org/10.1149/2.0261501jss.

(8) Utriainen, M.; Kroger-Laukkanen, M.; Johansson, L.-S.; Niinisto, L. Studies of Metallic Thin Film Growth in an Atomic Layer Epitaxy Reactor Using Mžacac/ 2 žM s Ni, Cu, Pt/ Precursors. **2000**.

(9) Wu, L.; Eisenbraun, E. Hydrogen Plasma-Enhanced Atomic Layer Deposition of Copper Thin Films. *J. Vac. Sci. Technol. B Microelectron. Nanometer Struct. Process. Meas. Phenom.* **2007**, *25* (6), 2581–2585. https://doi.org/10.1116/1.2779050.

(10) Knisley, T. J.; Kalutarage, L. C.; Winter, C. H. Precursors and Chemistry for the Atomic Layer Deposition of Metallic First Row Transition Metal Films. *Coord. Chem. Rev.* **2013**, *257* (23–24), 3222–3231. https://doi.org/10.1016/j.ccr.2013.03.019.

(11) Faraz, T.; Arts, K.; Karwal, S.; Knoops, H. C. M.; Kessels, W. M. M. Energetic Ions during Plasma-Enhanced Atomic Layer Deposition and Their Role in Tailoring Material Properties. *Plasma Sources Sci. Technol.* **2019**, *28* (2), 024002. https://doi.org/10.1088/1361-6595/aaf2c7.

(12) Jansen, H.; Gardeniers, H.; de Boer, M.; Elwenspoek, M.; Fluitman, J. A Survey on the Reactive Ion Etching of Silicon in Microtechnology. *J. Micromechanics Microengineering* **1996**, *6* (1), 14.

(13) Powell, C. J.; Jablonski, A. The NIST Electron Effective-Attenuation-Length Database. *J. Surf. Anal.* **2002**, *9* (3), 322–325.

(14) Wada, S.; Murata, Y.; Tokunaga, A. T.; Watanabe, J. Experimental Study of Amorphous Silicate Formation. *Astron. Astrophys.* **2003**, *406* (3), 783–788. https://doi.org/10.1051/0004-6361:20030750.

(15) Li, Z.; Rahtu, A.; Gordon, R. G. Atomic Layer Deposition of Ultrathin Copper Metal Films from a Liquid Copper(I) Amidinate Precursor. *J. Electrochem. Soc.* **2006**, *153* (11), C787. https://doi.org/10.1149/1.2338632.

(16) Avval, T. G.; Průša, S.; Cushman, C. V.; Hodges, G. T.; Fearn, S.; Kim, S. H.; Čechal, J.; Vaníčková, E.; Bábík, P.; Šikola, T.; Brongersma, H. H.; Linford, M. R. A Tag-and-Count Approach for Quantifying Surface Silanol Densities on Fused Silica Based on Atomic Layer Deposition and High-Sensitivity Low-Energy Ion Scattering. *Appl. Surf. Sci.* **2023**, *607*, 154551. https://doi.org/10.1016/j.apsusc.2022.154551.

(17) Torres-Ochoa, J. A.; Cabrera-German, D.; Cortazar-Martinez, O.; Bravo-Sanchez, M.; Gomez-Sosa, G.; Herrera-Gomez, A. Peak-Fitting of Cu 2p Photoemission Spectra in Cu0, Cu1+, and Cu2+ Oxides: A Method for Discriminating Cu0 from Cu1+. *Appl. Surf. Sci.* **2023**, *622*, 156960. https://doi.org/10.1016/j.apsusc.2023.156960.

(18) Wagner, C.; Naumkin, A.; Kraut-Vass, A.; Allison, J.; Powell, C.; Rumble Jr, J. NIST Standard Reference Database 20, Version 3.4 (Web Version). *Natl. Inst. Stand. Technol. Gaithersburg MD* **2003**, *20899*.

(19) Biesinger, M. C.; Payne, B. P.; Grosvenor, A. P.; Lau, L. W. M.; Gerson, A. R.; Smart, R. St. C. Resolving Surface Chemical States in XPS Analysis of First Row Transition Metals, Oxides and Hydroxides: Cr, Mn, Fe, Co and Ni. *Appl. Surf. Sci.* **2011**, *257* (7), 2717–2730. https://doi.org/10.1016/j.apsusc.2010.10.051.

(20) Bourque, J. L.; Biesinger, M. C.; Baines, K. M. Chemical State Determination of Molecular Gallium Compounds Using XPS. *Dalton Trans.* **2016**, *45* (18), 7678–7696. https://doi.org/10.1039/C6DT00771F.

(21) Biesinger, M. C. Advanced Analysis of Copper X-ray Photoelectron Spectra. *Surf. Interface Anal.* **2017**, *49* (13), 1325–1334. https://doi.org/10.1002/sia.6239.

(22) Beamson, G. High Relution Xps of Organic Polymers. the Scienta Esca 300 Database. *ICIplc* **1992**.

(23) Heil, S. B. S.; Van Hemmen, J. L.; Van De Sanden, M. C. M.; Kessels, W. M. M. Reaction Mechanisms during Plasma-Assisted Atomic Layer Deposition of Metal Oxides: A Case Study for Al2O3. *J. Appl. Phys.* **2008**, *103* (10), 103302. https://doi.org/10.1063/1.2924406.

(24) Mione, M. A.; Engeln, R.; Vandalon, V.; Kessels, W. M. M.; Roozeboom, F. Infrared and Optical Emission Spectroscopy Study of Atmospheric Pressure Plasma-Enhanced Spatial ALD of Al2O3. *Appl. Phys. Lett.* **2019**, *115* (8), 083101. https://doi.org/10.1063/1.5113753.

(25) Boris, D. R.; Johnson, M. J.; Woodward, J. M.; Wheeler, V. D.; Walton, S. G. Remote Inductively Coupled Plasmas in Ar/N2 Mixtures and Implications for Plasma Enhanced ALD. *J. Vac. Sci. Technol. A* **2024**, *42* (3), 033008. https://doi.org/10.1116/6.0003538.

(26) Jiménez-Redondo, M.; Cueto, M.; Doménech, J. L.; Tanarro, I.; Herrero, V. J. Ion Kinetics in Ar/H_2 Cold Plasmas: The Relevance of ArH^+. *RSC Adv* **2014**, *4* (107), 62030–62041. https://doi.org/10.1039/C4RA13102A.

(27) Kimura, T.; Kasugai, H. Properties of Inductively Coupled Rf Ar/H2 Plasmas: Experiment and Global Model. *J. Appl. Phys.* **2010**, *107* (8), 083308. https://doi.org/10.1063/1.3345084.

(28) Abdel-Rahman, M.; Gathen, V. S. D.; Gans, T.; Niemi, K.; Döbele, H. F. Determination of the Degree of Dissociation in an Inductively Coupled Hydrogen Plasma Using Optical Emission Spectroscopy and Laser Diagnostics. *Plasma Sources Sci. Technol.* **2006**, *15* (4), 620–626. https://doi.org/10.1088/0963-0252/15/4/005.

(29) Gordiets, B.; Ferreira, C. M.; Pinheiro, M. J.; Ricard, A. Self-Consistent Kinetic Model of Low-Pressure - Flowing Discharges: II. Surface Processes and Densities of N, H, Species. *Plasma Sources Sci. Technol.* **1998**, *7* (3), 379–388. https://doi.org/10.1088/0963-0252/7/3/016.

(30) Zhang, X.-Y.; Peng, D.-C.; Yan, J.-H.; Zhang, Z.-X.; Ruan, Y.-J.; Zuo, J.; Xie, A.; Wu, W.-Y.; Wuu, D.-S.; Huang, C.-J.; Lai, F.-M.; Lien, S.-Y.; Zhu, W.-Z. Plasma Power Effect on Crystallinity and Density of AlN Films Deposited by Plasma Enhanced Atomic Layer Deposition. *J. Mater. Res. Technol.* **2023**, *27*, 4213–4223. https://doi.org/10.1016/j.jmrt.2023.10.302.

(31) Yoon, H. J.; Jeon, H. Impact of Plasma Power on Plasma Enhanced Atomic Layer Deposited TiO2 as a Spacer. *Thin Solid Films* **2024**, *807*, 140551. https://doi.org/10.1016/j.tsf.2024.140551.

(32) Iordanova, S.; Koleva, I.; Paunska, T. Hydrogen Degree of Dissociation in a Low Pressure Tandem Plasma Source. *Spectrosc. Lett.* **2011**, *44* (1), 8–16. https://doi.org/10.1080/00387010903386540.

(33) Yoon, M. Y.; Jeong, J.-R.; Lee, H.-C.; Kim, J.-H. Plasma Low-Energy Ion Flux Induced Vertical Graphene Synthesis. *Appl. Surf. Sci.* **2023**, *636*, 157814. https://doi.org/10.1016/j.apsusc.2023.157814.

(34) Kusano, E.; Fukushima, K.; Saitoh, T.; Saiki, S.; Kikuchi, N.; Nanto, H.; Kinbara, A. Effects of Ar Pressure on Ion Flux Energy Distribution and Ion Fraction in r.f.-Plasma-Assisted Magnetron Sputtering. *Surf. Coat. Technol.* **1999**, *120–121*, 189–193. https://doi.org/10.1016/S0257-8972(99)00453-3.

(35) Doh, H.-H.; Horiike, Y. Gas Residence Time Effects on Plasma Parameters: Comparison between Ar and C_4F_8. *Jpn. J. Appl. Phys.* **2001**, *40* (5R), 3419. https://doi.org/10.1143/JJAP.40.3419.

(36) Hair, J. F. Multivariate Data Analysis. **2009**.

6 Impact study of unstable processing plasma of ZrN PE-ALD process with in-situ monitoring

6.1 Introduction

This chapter examines the plasma-enhanced atomic layer deposition (PE-ALD) of zirconium nitride (ZrN). ZrN is a material of interest due to its high thermal stability[1], high hardness[2] and low electrical resistivity, with stoichiometric ZrN exhibiting values of 20μΩ·cm[3]. These properties have made ZrN an appealing candidate for applications such as diffusion barriers[4,5]. The ability of ALD to produce extremely thin, uniform, and conformal films over complex structures further motivates the investigation of ZrN using ALD-based methods.

Several zirconium precursors have been successfully employed for ZrN ALD using hydrogen and nitrogen based plasmas as co-reactants, including TDEAZr[6], and TDMAZr[7,8]. Among these, TDMAZr has been demonstrated using a combined H_2/N_2 plasma, providing a foundation for the present study. Previous work by Muneshwar et al.[9] showed that surface –OH functional groups act as active sites for initial-stage growth, also showing that thicker films exhibited incorporation of oxygen and carbon impurities. However, no optimisation of the plasma process conditions was conducted. The current work aims to address this gap by systematically varying the ICP power and chamber pressure and investigating their effect on the resulting film properties.

In this chapter, ZrN deposition using TDMAZr and H_2/N_2/Ar plasma is examined with in-situ optical emission spectroscopy (OES) for plasma monitoring. A reference process was performed throughout the experimental work to investigate the reproducibility of the

process. Following deposition, in-situ XPS enabled detailed characterisation of the films, including thickness, elemental composition, and chemical bonding.

The initial objective of this study was to systematically optimise the PE-ALD process parameters for ZrN and to demonstrate the reproducibility of the deposition process. However, no pre-ALD plasma investigation was performed and as a result, instabilities in the plasma were not identified prior to processing. This led to the unintended uses of unstable plasma conditions during the experimental work. These instabilities were captured in the in-situ OES data but only investigated after the experimental work had concluded. Consequently, rather than taking the form of an optimisation study, this chapter presents a case study on the impact of plasma instability during PE-ALD, and the consequences of not optimising plasma parameters. Inconsistent film properties from repeated reference process along with deviations from previously established process parameters trends were observed. This work highlights the critical nature of plasma stability in PE-ALD processing.

6.2 Experimental Details

Zirconium nitride (ZrN) thin films were deposited by plasma-enhanced ALD using tetrakis(dimethylamido)zirconium(IV) (TDMAZr, Strem), heated to 75 °C, as the metal precursor, and an H_2/N_2/Ar plasma as the co-reactant. The plasma feed gases (N_2, H_2, Ar) were supplied in a 2:6:1 ratio, corresponding to a plasma composition approximately equivalent to 80% NH_3 and 20% Ar. Previous studies using TDMAZr employed forming gas (5% H_2, 95% N_2), the present work uses a significantly higher H_2 fraction along with Ar, motivated primarily by the requirements of the optical diagnostics. Similar TDMA-based precursors have been shown to successfully make use of an NH_3 plasma as the co-reactant[10,11]. Each ALD cycle consisted of a 0.2 s TDMAZr dose at 40 mTorr, followed by a 3 s Ar purge and a 10 s pump step. The plasma step was applied for 10 s in all cases, after which the chamber was purged with Ar for 3s and pumped for 3 s before the next cycle. The substrate temperature was maintained at 150 °C.

Films were deposited on Si substrates with native oxide. Prior to deposition, substrates were cleaned in an isopropanol (IPA) sonicated bath for 10 min, dried under N_2 flow, and loaded into the system's load lock. A pretreatment consisting of a 3 min O_2 plasma exposure followed by a 3 min NH_3 plasma exposure was performed on all samples, to clean and functionalise the surface. Post-treatment Si 2p XPS measurements indicated a surface oxide thickness of 0.8 nm, determined using the method of Jensen et al[12].

Each experiment comprised of 15 ALD cycles, producing thin zirconium-containing films. Film thickness was calculated via Si 2p signal attenuation in post-deposition XPS, as described in Chapter 2. After deposition, samples were transferred to the XPS chamber via robotic handling under vacuum. Survey spectra were collected over 900–0 eV binding energy at 100 eV pass energy. High-resolution spectra of all identified elements were

acquired at 50 eV pass energy. All spectra were analysed using CasaXPS software with a Shirley–Sherwood background. Binding energies were referenced to the Si $2p_{3/2}$ peak at 99.4 eV.

In this chapter, the influence of key plasma parameters was investigated, namely ICP power and the chamber pressure. Each parameter was examined at three setpoints which ranged: 100, 200, and 300 W for the power and 10, 30, and 60 mTorr for the pressure. A reference process (200 W, 10 mTorr) was performed three times as the first, fourth and last process to assess the repeatability. For each parameter variation, the remaining parameters were held at their reference values. A chamber cleaning process was performed between all depositions which included a plasma cleaning process and chamber pump/purge steps.

6.3 Results

This chapter presents the experimental results in two sections. The first section examines the plasma response to variations in controlled process parameters using time-resolved OES acquired during the ALD cycles. Plasma stability for each process is quantified using the coefficient of variance of the Ar $2p_1$ and Hα Balmer emission peaks. The second section provides the results of the film characterisation using in-situ XPS measurements.

6.3.1 Plasma Stability

In-situ OES measurements were recorded every 250 ms throughout each PE-ALD process. The Hα (656 nm) and Ar $2p_1$ (750 nm) emission peaks were extracted from the time-resolved spectra. Each ALD cycle lasted 10 s and a total of 15 cycles were performed for each parameter set. The coefficient of variation (CV), defined as the ratio of the standard deviation to the mean emission intensity ($CV = \sigma/\mu$), was first calculated for each individual ALD cycle using the intensity values recorded during that cycle. The reported CV values correspond to the mean of the cycle-by-cycle CV values for a given parameter set. The error bars represent the standard deviation of these CV values across the 15 cycles. The average CV values and associated standard deviations for both emission lines are presented in Figure 6.1.

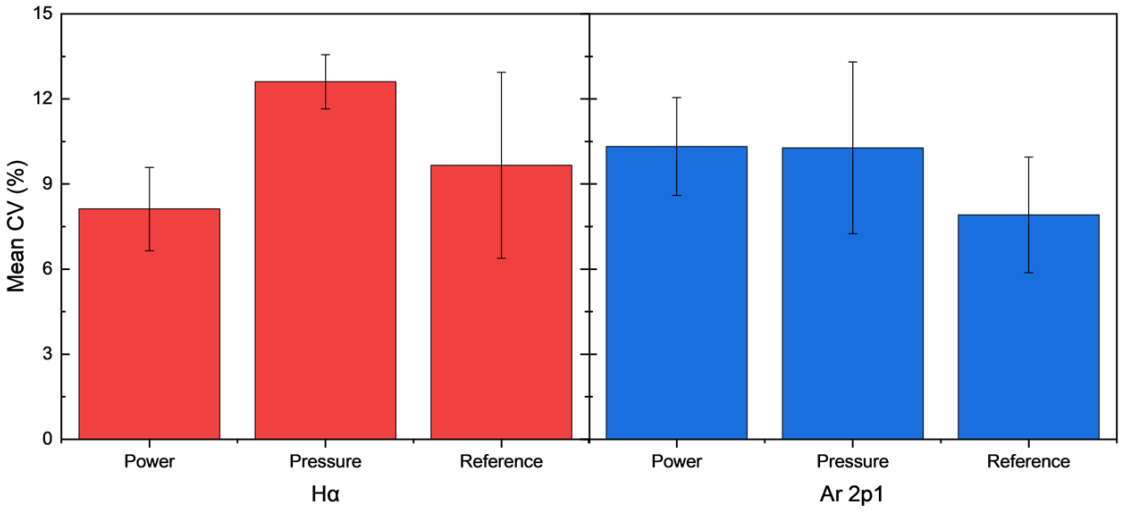


Figure 6.1 - Mean CV of Hα emission (red) and Ar $2p_1$ (blue) emission with error bars representing the standard deviation for process parameters and reference process during PE-ALD.

Among the parameter variations, the ICP power series produced the lowest CV for the Hα emission (8.1% ± 1.5%). The pressure variation yielded the highest Hα CV (12.6% ± 1.0%). For the Ar $2p_1$ emission, both power and pressure variations produced similar mean CV values of approximately 10.3% with different standard deviations (1.7% for power and 3.0% for pressure). The parameter variation experiments involved changes to the operating conditions, whereas the reference processes were run at fixed parameters (200 W, 10 mTorr). Despite this, the reference processes still exhibited substantial CV values for both Hα (9.7% ± 3.3%) and Ar $2p_1$ (7.9% ± 2.2%).

A more detailed investigation of the three reference runs revealed progressive changes in stability. The first reference run (Ref 1) exhibited the lowest CV values, 6.0% for Hα and 5.4% for Ar $2p_1$. After completing the ICP power variations, the second reference run (Ref 2) showed increased CV values of 9.0% for Hα and 10.4% for Ar $2p_1$. The final reference run (Ref 3), performed after the pressure variations, displayed a further increase

in Hα CV (13.9%) while the Ar $2p_1$ CV returned to 7.9%. Figure 6.2 displays the time-resolved OES of the ALD cycles of each reference process.

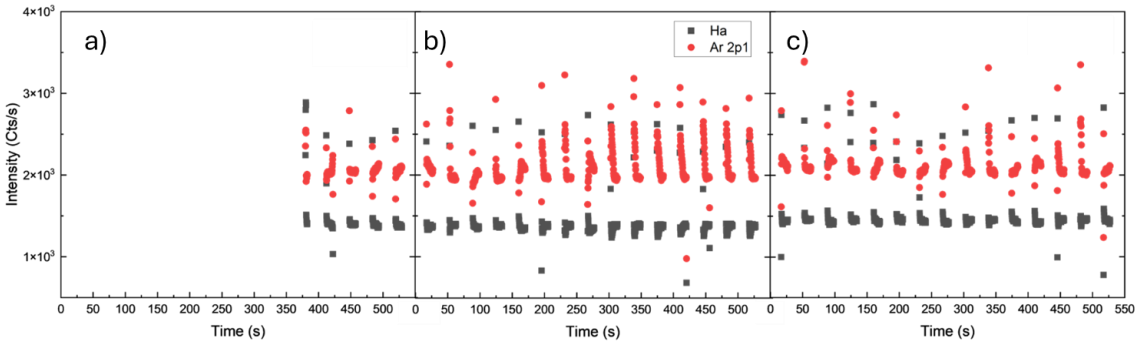


Figure 6.2 - Time resolved OES of a) Ref 1, b) Ref 2 and c) Ref 3 Hα and Ar $2p_1$ emission peaks.

An error in the recording of the initial cycles for Ref 1 left only the last 5 cycles of the process recorded. The Hα emission intensity appears relatively stable across all reference runs, apart from initial outliers occurring during plasma ignition. These spikes quickly decrease, with the emission stabilising within ~0.5 s. The Ar $2p_1$ emission generally shows similar behaviour, with a spike at ignition followed by stabilisation. In general, the stabilisation of the Ar $2p_1$ emission takes longer than the Hα. In Ref 2 there is a systematic change in observed Ar $2p_1$ intensity for approximately half of the 10 s discharge. Overall, the effect of the initial emission is less pronounced in the CV values for Ar $2p_1$ because the magnitude of the outliers represents a smaller fraction of the total emission intensity.

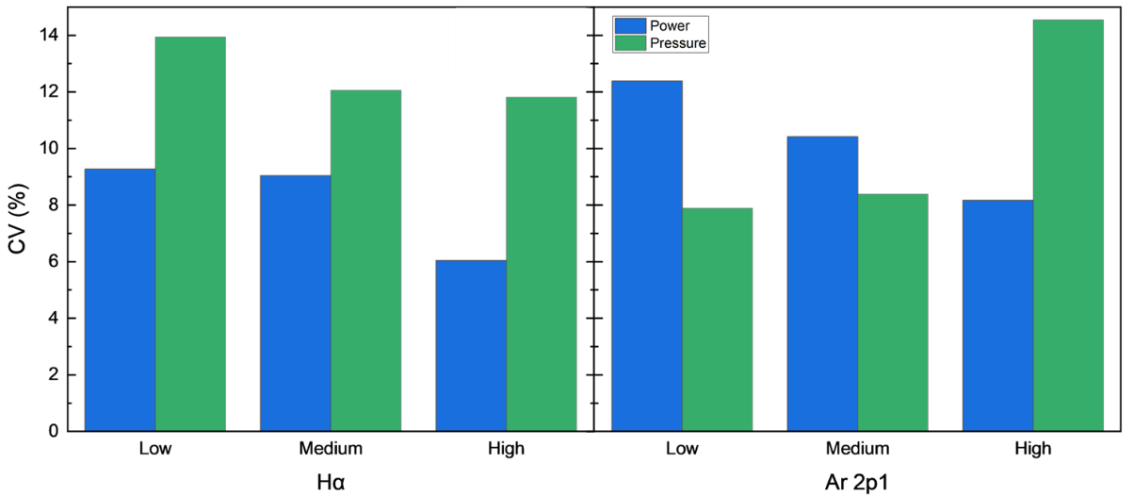


Figure 6.3 - CV of Hα (left) and Ar $2p_1$ (right) emission peaks for variations in the power (blue) and pressure (green) process parameters. Low, medium and high are representing the parameter values of 100 W, 200 W and 300 W, respectively, for power and 10 mTorr, 30 mTorr and 60 mTorr, respectively, for pressure.

Figure 6.3 shows that increasing ICP power reduces the CV for both emission peaks, which could indicate improved plasma stability at higher powers. Pressure shows a similar trend for the Hα emission with higher pressure produces lower CV values. The Ar $2p_1$ emission shows the opposite behaviour. Increasing pressure from 10 to 30 mTorr results in a slight increase in CV, while a further increase to 60 mTorr leads to the largest rise in CV observed across all conditions. This trend difference could indicate a change in processing conditions occurring with parameter variation.

Overall, the investigation into the time-resolved OES using the coefficient of variation has shown that the plasma has instabilities under the examined conditions, with significant fluctuations present in both the parameter variation and under fixed conditions.

6.3.2 Film Characterisation

6.3.2.1 Reference process

The reference process (200 W, 10 mTorr) was carried out at three stages of the experimental work. The initial process (Ref 1), after the ICP power investigation (Ref 2), and at the end of the study (Ref 3). Process logs were examined to confirm that no parameters were varying between these runs, ensuring that all reference processes were identical on logs. Table 6.1 summarises the elemental composition of each film as measured by in-situ XPS immediately after deposition.

Table 6.1 - XPS survey elemental composition for repeated reference processes (1-3).

Process	Si 2p (%)	O 1s (%)	C 1s (%)	N 1s (%)	Zr 3d (%)
Ref 1	27.4	29.3	11.1	16.7	15.7
Ref 2	27.6	17.2	15.5	25.8	13.9
Ref 3	48.3	36.8	0.0	5.8	9.0

Significant variation was observed across all reference films. Although film thickness was not directly calculated, the Si 2p intensity provides an approximate indication of overlayer thickness through substrate signal attenuation. Prior to deposition, the Si 2p signal measured 68.4%. Ref 1 and Ref 2 showed similar attenuated values (~27.5%), suggesting comparable overlayer thicknesses. In contrast, Ref 3 exhibited a higher Si 2p signal (48.3%), indicating a substantially thinner film.

However, despite the similar Si 2p values for Ref 1 and Ref 2, their oxygen compositions reveal further inconsistency. The O 1s signal varied by approximately 20 % across the three reference processes, with the spread roughly evenly distributed. This lack of repeatability is further demonstrated by the N 1s composition. Another ~20 % range was

observed, with values spanning from 5.8 % to 26.8 %, while the intermediary film measured 16.7 %. These results clearly indicate that nitrogen incorporation was not consistent across the reference runs.

No reproducibility was observed in the Zr 3d:N 1s or Zr 3d:C 1s ratios either. The Zr 3d:N 1s ratios were 0.94, 0.54, and 1.55 for Ref 1, Ref 2, and Ref 3, respectively, while the corresponding Zr 3d:C 1s ratios were 1.41, 0.89, and the final film showed no carbon. The magnitude of these variations confirms that the reference processes did not produce films with consistent compositions, despite identical processing conditions.

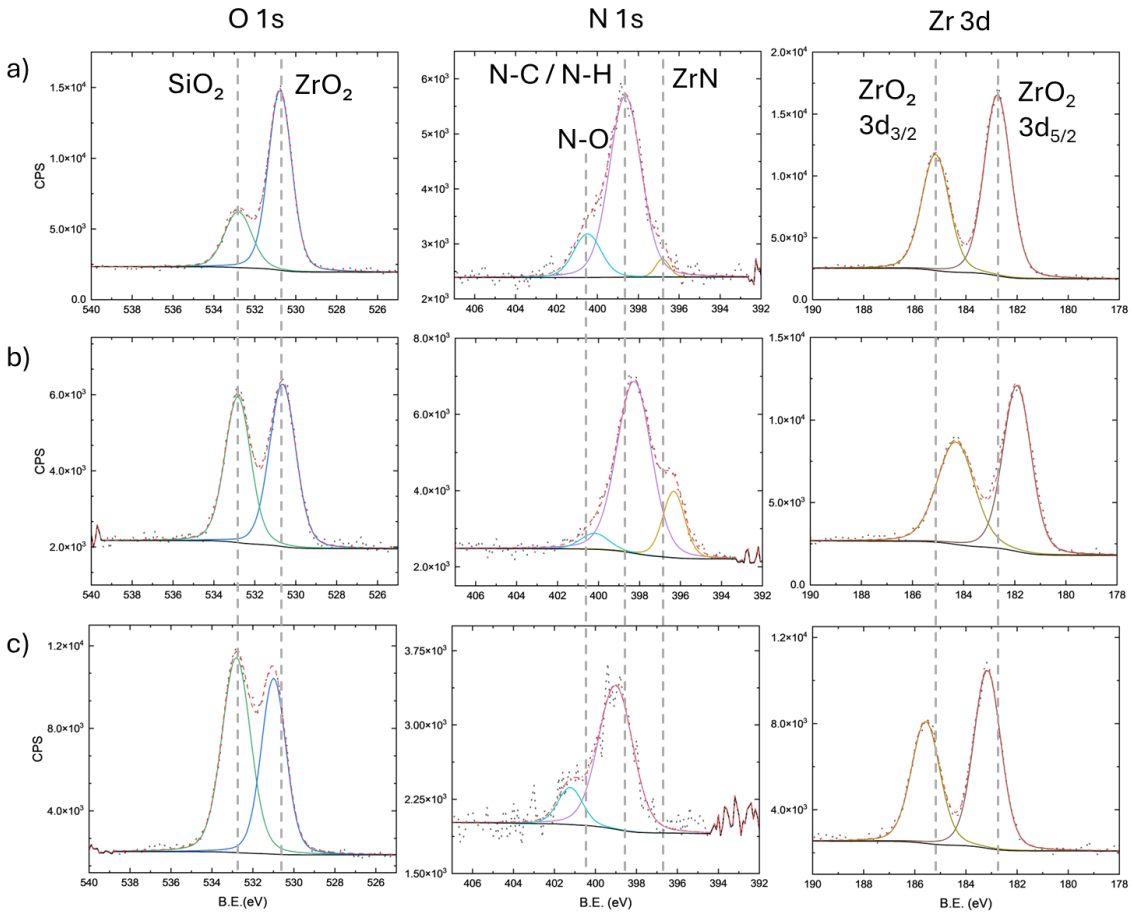


Figure 6.4 - Fitted O 1s (left), N 1s (middle) and Zr 3d (right) XPS spectra of a) Ref 1, b) Ref 2 and c) Ref 3 PE-ALD films.

To further investigate the higher resolution XPS spectra were fitted and analysed. Figure 6.4 displays the fitted O 1s, N 1s and Zr 3d spectra for a) Ref 1, b) Ref 2 and c) Ref 3. The Ref 1 process produced a film mostly comprised of ZrO_2 and precursor fragmentation. Both the ZrO_2 peaks in the O 1s and Zr 3d align with literature values[13]. A small fraction of the N 1s suggests the presence of ZrN[14], while the majority is attributed to a combination of NH_x[15,16] and N-C[13] with the higher binding energy attributed to N-O[17] bonding.

A notable change is observed in Ref 2. While the O 1s positions remain constant, the peak ratios change suggesting less ZrO_2 present. All peaks shift down in binding energy in the N 1s, suggesting an improved removal of oxides from the local matrix. The ZrN peak ratio also improves from ~4% to over 18 %. Additionally, a significant shift is also present in the Zr 3d spectra. However, the binding energy suggests the presence of ZrO_xN_y[14] not ZrN which is present around 179 eV[14].

The Ref 3 film displays a drop in signal intensity for all spectra suggesting poor growth which is confirmed by the Si 2p attenuation. No ZrN peak was present in the N 1s. An increasing binding energy in the Zr 3d was also present suggesting the removal of any ZrN contribution, leaving only ZrO_2 Increased binding energy was also present for the N 1s. It must be noted that this process displayed no C 1s in the survey or high-resolution windowed scan. As a result, most of the N 1s is attributable to the presence of NH_x.

From the results, is it clear that variations in film properties go beyond the deposition's elemental composition, but also significantly impact the bonding within the film. All processes suggest significant ZrO_2 presence, with several nitrogen bonding states.

6.3.2.2 Parameter investigation

To investigate the influence of both power and pressure variations on the produced films, the Si 2p (Figure 6.5 & 6.7 (a)) and Zr 3d (Figure 6.5 & 6.7 (b)) compositions are compared to estimate the GPC of the overlayer along with the Zr content in the overlayer. Two ratios, Zr 3d:C 1s (Figure 6.5 & 6.7 (c)) and Zr 3d:N 1s (Figure 6.5 & 6.7 (d)) are also investigated to identify the ligand incorporation and stoichiometry of the film.

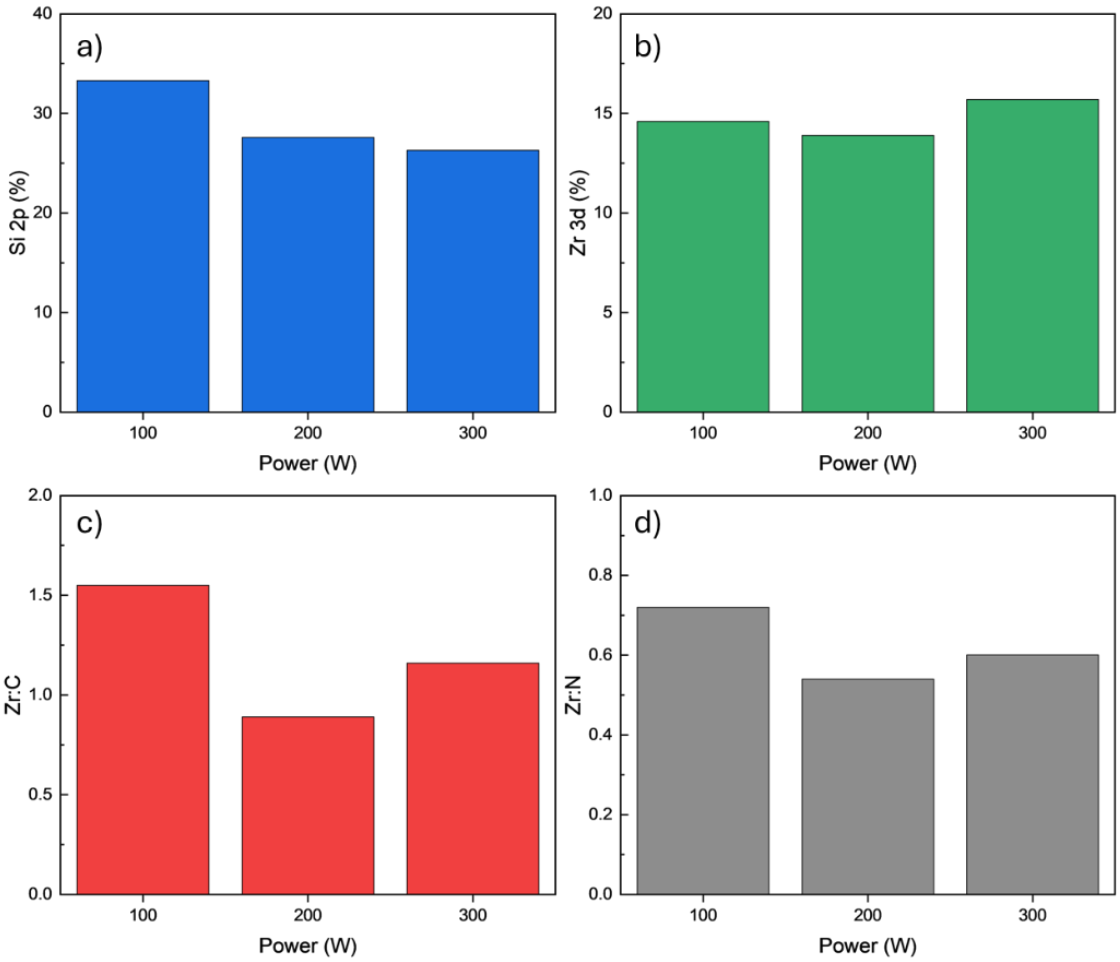


Figure 6.5 - Bar chart of a) Si 2p (%), b) Zr 3d (%), c) Zr 3d:C 1s ratio and d) Zr 3d:N 1s ratio for power variation processes.

From Figure 6.5 (a) it is seen that increasing the power resulted in the Si 2p signal to attenuate from 33.3 % at 100W to 27.6 at 200 W finally to 26.3 at 300 W. However, the Zr 3d content (Figure 6.5 (b)) was non-linear with 200 W producing the lowest amount of 13.9 % followed by 100 W (14.6 %) and then 300 W (15.7 %). The same non-linear trend was identified for both investigated ratios. In Figure 6.5 (c), 200W produced the lowest Zr 3d:C 1s (0.89) followed by 300 W (1.16) then 100 W (1.55). The same order was observed in the Zr 3d:N 1s stoichiometry, seen in Figure 6.5 (d) with values ranging from 0.54 – 0.72. All variations in power resulted in higher nitrogen content than zirconium resulting in a stoichiometry of Zr_1N_x where x > 1.

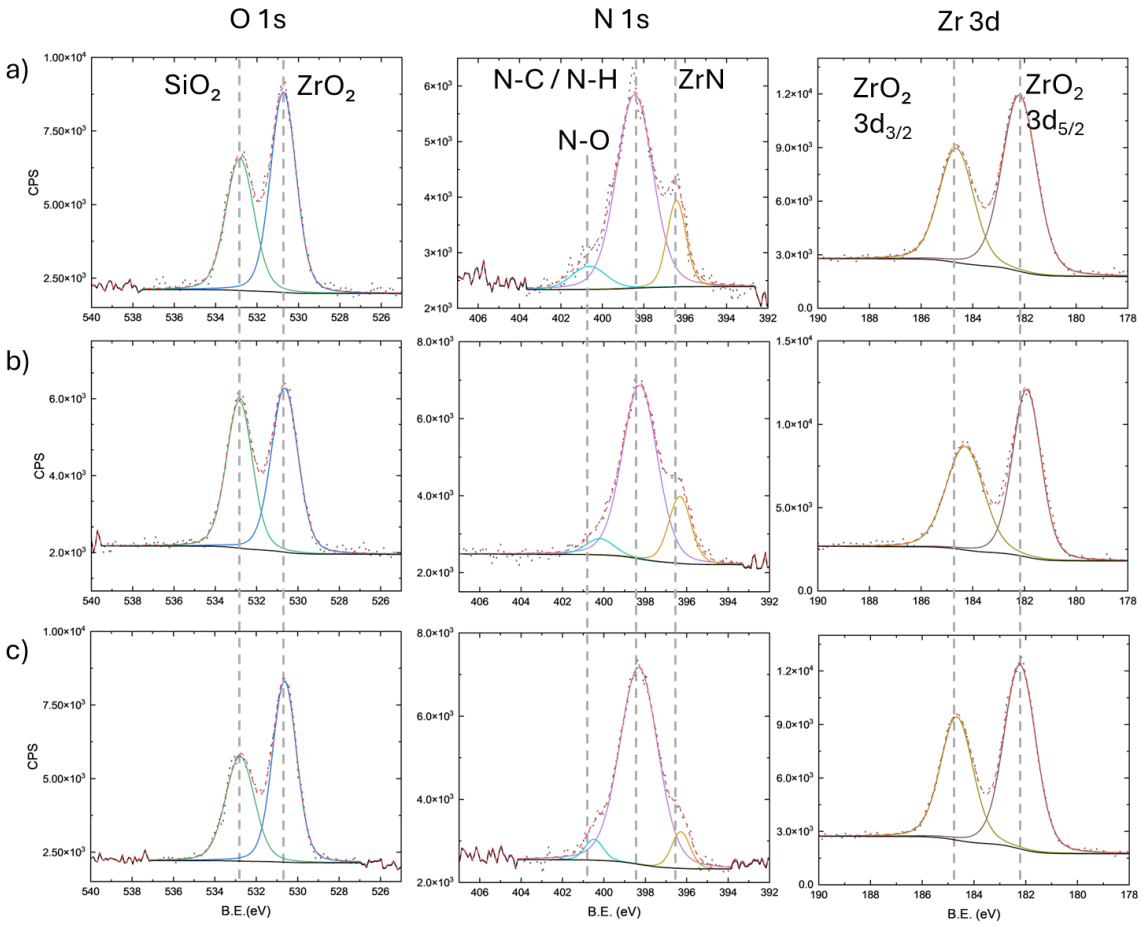


Figure 6.6 - Fitted O 1s (left), N 1s (middle) and Zr 3d (right) XPS spectra of a) 100 W, b) 200W and c) 300 W PE-ALD films.

There is a decrease in the ZrO_2 contribution for the 200 W process which contributes to the overall decrease in the oxygen composition of the film. The decreased oxygen content for the 300 W film, compared to the 100 W film (26.3 vs 33.3) is identified to be a result of the reduction in the both the SiO_2 and ZrO_2 peaks. The N 1s shows a reduction in the ZrN peak with increasing power. There is also a reduction in the N-O contribution, suggesting increasing power results in NH_x and N-C bonding. All produced films display prominent ZrO_2 peaks in the Zr 3d, with the only variation occurring in the 200 W. A downshift in the binding energy suggests a primarily ZrO_xN_y contribution as previously discussed in the Ref 2 process.

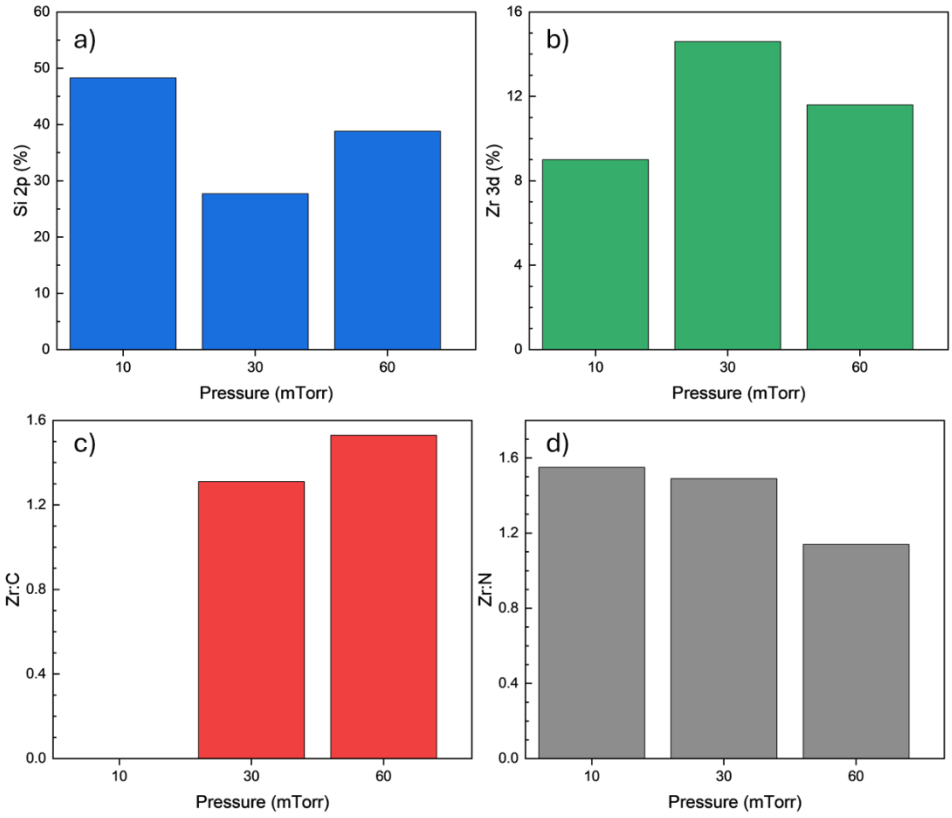


Figure 6.712 - Bar chart of a) Si 2p (%), b) Zr 3d (%), c) Zr 3d:C 1s ratio and d) Zr 3d:N 1s ratio for pressure variation processes.

Increasing the chamber pressure resulted in a decrease in the Si 2p signal from 48.3 % for 10 mTorr suggesting thicker films which was a previously established trend, as seen in Figure 6.7 (a). However, it was found that 30 mTorr produced the smallest signal of 27.7 % with a significant increase to 38.8 % for 60 mTorr. The Zr 3d composition, seen in Figure 6.7 (b) aligns with the Si 2p results in which lower Si 2p results in more Zr 3d content. In Figure 6.7 (c), the 10 mTorr process produced no detectable C 1s peak and so no Zr 3d:C 1s calculation was possible, but it clearly suggests no precursor ligand incorporation. The 30 mTorr process had the most ligand incorporation for the investigated range while an improvement was observed with increased pressure. From Figure 6.7 (d), all pressure variations displayed a positive Zr 3d:N 1s ratio suggesting more zirconium incorporation than nitrogen (Zr_1N_x where $x < 1$), which is the opposite of what was observed in the power variations processes. The 60 mTorr produced the closest ZrN stoichiometry of 1.14:1.

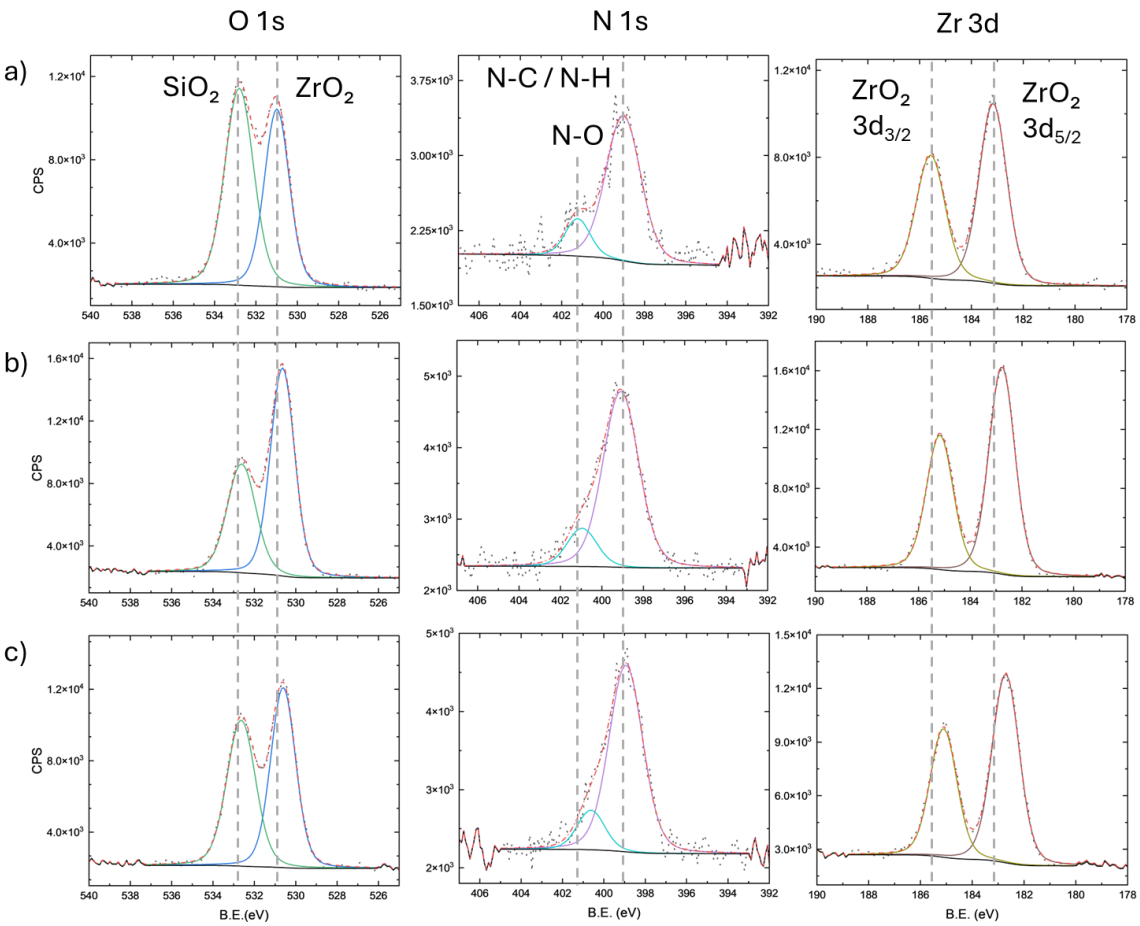


Figure 6.8 - Fitted O 1s (left), N 1s (middle) and Zr 3d (right) XPS spectra of a) 10 mTorr, b) 30 mTorr and c) 60 mTorr PE-ALD films.

Increasing the pressure resulted in a decrease in the SiO_2 peak contribution in the O 1s, suggesting increased overlayer thickness, as seen in Figure 6.8 (a). Both 10 mTorr and 60 mTorr had similar ZrO_2 peaks while 30 mTorr displayed a significant increase. Similar N 1s was observed for all processes with a slight decrease of the N-C/N-H peak observed in the 10 mTorr process. Increasing the pressure produced a down shift in the binding energy of Zr 3d peaks suggesting a shift from ZrO_2 to ZrO_xN_y contribution.

In summary, the three reference processes produced large variations in film thickness, composition and bonding, despite fixed parameters displaying poor reproducibility. Ref 1 and Ref 2 showed comparable Si 2p attenuation, but Ref 3 produced a much thinner

overlayer. All three processes produced a broad range of O 1s and N 1s compositions and the ZrN stoichiometry also varied significantly from 0.54 to 1.55. High resolution XPS confirmed ZrO_2 dominated with some ZrO_xN_γ presence. The only variation identified in the process was instabilities within the plasma response, identified by in-situ OES, suggesting the plasma instability is driving the film variation. The parameter studies reinforced this conclusion. Zirconium and nitrogen incorporation, impurities and bonding states all fluctuated irregularly with both power and pressure. When paired with the reference process investigation, the results show that plasm instability dominated the film properties. This forms the basis for the following discussion on the plasma stability and its impact on the films.

6.4 Discussion

In-situ OES measurements demonstrated that the plasma in this study was significantly more unstable than in the previous chapters. The coefficient of variation increased from approximately 1% in the pre-ALD work from Chapter 4 to ~ 2.5 % mean during the ALD processes of the $Cu(acac)_2$ and H_2/Ar plasma in Chapter 5. A mean CV values across the investigated emission lines of approximately 10 % was identified in the present work, representing an order of magnitude increase. This indicates that the H_2/N_2/Ar plasma used in the current work is much more sensitive to environmental changes then the previous work. Carrasco et al [18] utilised time resolved OES measurements for H_2/N_2 plasma discharge and noted ignition spikes and slow recovery to equilibrium. It was also seen that small changes in the H_2 or N_2 produced large shifts in the corresponding atomic densities, suggesting a sensitive to the processing parameters.

The previous work utilised a pre-ALD investigation to identify stable plasma processing parameters, which was not performed in the current work. As a result, the importance of the pre-ALD investigation is clearly shown from the instabilities displayed. Despite running three identical processes with identical pre-ALD cleaning processes and sample pre-treatments, significant changes in film properties were identified. The overlayer thickness varied, indicated by an Si 2p signal ranging from 27 % to 48 % along with the N 1s and O 1s signals varying by 20 %. Bonding within the Zr 3d peak shifted suggesting differing concentrations of ZrO_2 and ZrO_xN_γ present in the overlayers. These results confirm that the film properties were directly determined by the state of the plasma for each run. The importance of the plasma in PE-ALD processes has been the subject of several invesigations[19–22]. Changes in processing parameters impact ion and reactive species flux, ion energy, reactive species generation, ultraviolet photons etc, which are all features that influence film growth and quality. Inconsistent plasma can result in

changes in the resulting features impacting both the films properties and the reproducibility of the process.

Previous work on TDMA- based precursors has demonstrated increasing power resulted in increased GPC and decreased resistivity for nitride films[23]. Similar trends have also been seen in other PE-ALD work with reports of improved GPC[24] and density[25] with increased power. In the current work, increasing power from 100 W to 200 W improved the overlayer thickness. However, the zirconium content dropped with the increased power while carbon increased. The increased power was established to improve the GPC by increasing the active sites available for subsequent ALD cycles through enhanced ligand removal. The observed results suggest the improved GPC is a result of ligand fragmentation providing active site resulting in a significant drop in the Zr 3d:C 1s ratio.

Previous chapters have investigated the influence of pressure on film properties in detail, revealing that increased pressure results in reduced ion flux at the substrate along with increased quenching of reactive species. Similar reports have been published[22,26,27]. The 10 mTorr pressure process produced the thinnest overall film, suggesting that increased ion flux and reducing quenching reduces the corresponding film GPC. This contradicts with all previous and published work. It was found that both low power and pressure processes had significant CV values for the emission lines, suggesting inconsistent plasma. The lack of consistency with both published results and previously investigated work within this thesis reinforces the inconsistency of the plasma processing controlled the film properties, as opposed to the process parameters.

The general inconsistency found within the film as a response to the instabilities explain the significant variation in the overlayer growth and properties. Despite the intended ZrN chemistry, all films were found to consist primarily of ZrO_2. Rehman et al[28] suggested

that exposure of ZrN to hydrogen radicals can lead to de-nitridation via the formation of nitrogen–hydrogen species. However, given the significantly higher bond enthalpy of Zr–N compared with typical hydrogen–nitrogen interactions, it is unlikely that hydrogen alone would fully remove nitrogen from a stable ZrN lattice under the low-temperature PE-ALD conditions used here. Instead, the observed NH contribution in the N 1s spectra is more likely associated with surface NH_x species generated during the plasma step, and any partial de-nitridation may be facilitated primarily by the instability of the plasma and the thin nature of the films, rather than direct hydrogen attack on bulk Zr–N bonds. Additionally, Elam et al[29] reported that in TDMATi and NH_3 PE-ALD processing, the plasma generates surface NH species, and that NH_3 produces highly porous (>40 %) TiN films which facilitate oxidation. In the present work, the source of oxygen is likely a combination of factors. First, the native SiO_2 on the substrate provides an immediate source of oxygen at the surface, which can react with the zirconium precursor during the initial ALD cycles. Second, the films are extremely thin (15 cycles), so even small amounts of oxygen can dominate the film composition. Third, the unstable plasma leads to fluctuations in reactive species, reducing the efficiency of nitridation and promoting oxidation. Finally, the plasma chemistry produces NH_x radicals, which when combined with the high porosity of the films, increases susceptibility to oxidation. Together, the combination of substrate oxide, thin-film thickness, plasma instability, and plasma-induced porosity explains why the resulting porous films are dominated by ZrO_2 despite the intended ZrN deposition chemistry.

As already mentioned, the lack of a pre-ALD plasma investigation resulted in the selection of processing parameters and gas composition which provided an unstable, inconsistent discharge which significantly alter the resulting film. This case study highlights the benefits of such a pre-processing step. However, a major result identified

in this work is the importance of integrating in-situ OES monitoring in PE-ALD. In this study, OES was essential for identifying the true cause of the film variation, which would not be understood by film characterization alone.

6.5 Conclusion

This case study demonstrates that plasma stability was the dominant factor governing film growth and composition during the ZrN PE-ALD process. In contrast to previous stable discharges in earlier chapters, the $H_2/N_2/Ar$ plasma used exhibited significant fluctuations. Time resolved OES measurements showed ignition instability and slow recovery behaviour consistent with previously report work on H_2/N_2 discharges. The lack of a pre-ALD plasma investigation resulted in the selection of parameters and gas composition that allowed instabilities to occur during deposition.

Three reference processes, with identical fixed parameter conditions, produced significantly different film properties, including thickness, composition and bonding, confirming that the growth mechanisms what controlled by the plasma. Parameter variations in both power and pressure failed to reproduce trends expected from both literature and previous chapters, reinforcing the influence of the plasma instability. The films were dominated by zirconium oxygen bonded states. These were attributed to high porosity due to incomplete reactivity with plasma species, along with de-nitridation processes due to hydrogen species. This resulted in significant NH species within the N 1s spectra.

Overall, this study highlights two key requirements for improved PE-ALD processing. The first requirement is to employ a pre-ALD plasma investigation to identify stable plasma operating conditions. The second requirement is the use of in-situ OES monitoring during deposition to identify stable plasma operation. In-situ OES can provide additional benefits by utilising diagnostics methods to get quantitative feedback information. Without the proposed requirements, plasma variability can compromise process integrity and reproducibility.

6.6 References

(1) Lide, D. R. (2010). *Lide CRC Handb. Chem. Phys. 90th Ed. Boca Raton FL Editor. Advis. Board CRC Press. Francis* **2009**.

(2) Egeland, G.; Valdez, J.; Maloy, S.; McClellan, K.; Sickafus, K.; Bond, G. Heavy-Ion Irradiation Defect Accumulation in ZrN Characterized by TEM, GIXRD, Nanoindentation, and Helium Desorption. *J. Nucl. Mater.* **2013**, *435* (1–3), 77–87.

(3) Krusin-Elbaum, L.; Brodsky, S.; Ahn, K. Electrical Characterization of ZrN. *MRS Proc.* **1986**, *71*, 351. https://doi.org/10.1557/PROC-71-351.

(4) Leenaers, A.; Ye, B.; Van Eyken, J.; Van Den Berghe, S. ZrN Coating as Diffusion Barrier in U(Mo) Dispersion Fuel Systems. *J. Nucl. Mater.* **2021**, *552*, 153000. https://doi.org/10.1016/j.jnucmat.2021.153000.

(5) Leu, L. C.; Sadik, P.; Norton, D. P.; McElwee-White, L.; Anderson, T. J. Comparative Study of ZrN and Zr–Ge–N Thin Films as Diffusion Barriers for Cu Metallization on Si. *J. Vac. Sci. Technol. B Microelectron. Nanometer Struct. Process. Meas. Phenom.* **2008**, *26* (5), 1723–1727. https://doi.org/10.1116/1.2976571.

(6) Cho, S.; Lee, K.; Song, P.; Jeon, H.; Kim, Y. Barrier Characteristics of ZrN Films Deposited by Remote Plasma-Enhanced Atomic Layer Deposition Using Tetrakis (Diethylamino) Zirconium Precursor. *Jpn. J. Appl. Phys.* **2007**, *46* (7R), 4085.

(7) Wang, X.-Z.; Muneshwar, T. P.; Fan, H.-Q.; Cadien, K.; Luo, J.-L. Achieving Ultrahigh Corrosion Resistance and Conductive Zirconium Oxynitride Coating on Metal Bipolar Plates by Plasma Enhanced Atomic Layer Deposition. *J. Power Sources* **2018**, *397*, 32–36.

(8) Muneshwar, T.; Cadien, K. Influence of Atomic Layer Deposition Valve Temperature on ZrN Plasma Enhanced Atomic Layer Deposition Growth. *J. Vac. Sci. Technol. A* **2015**, *33* (6).

(9) Muneshwar, T.; Cadien, K. Probing Initial-Stages of ALD Growth with Dynamic in Situ Spectroscopic Ellipsometry. *Appl. Surf. Sci.* **2015**, *328*, 344–348.

(10) Longrie, D.; Deduytsche, D.; Haemers, J.; Smet, P. F.; Driesen, K.; Detavernier, C. Thermal and Plasma-Enhanced Atomic Layer Deposition of TiN Using TDMAT and NH_3 on Particles Agitated in a Rotary Reactor. *ACS Appl. Mater. Interfaces* **2014**, *6* (10), 7316–7324. https://doi.org/10.1021/am5007222.

(11) Ding, Z.-J.; Zhu, B.; Liu, W.-J.; Wu, X.-H.; Ding, S.-J. The Effect of NH_3 Plasma Pulse Time on Atomic Layer-Deposited TiN Films Using Tetrakis-(Dimethylamino) Titanium as a Metal Precursor. *Jpn. J. Appl. Phys.* **2019**, *58* (SH), SHHA02. https://doi.org/10.7567/1347-4065/ab1bcf.

(12) Jansen, H.; Gardeniers, H.; de Boer, M.; Elwenspoek, M.; Fluitman, J. A Survey on the Reactive Ion Etching of Silicon in Microtechnology. *J. Micromechanics Microengineering* **1996**, *6* (1), 14.

(13) Wagner, C.; Naumkin, A.; Kraut-Vass, A.; Allison, J.; Powell, C.; Rumble Jr, J. NIST Standard Reference Database 20, Version 3.4 (Web Version). *Natl. Inst. Stand. Technol. Gaithersburg MD* **2003**, *20899*.

(14) Muneshwar, T.; Cadien, K. Comparing XPS on Bare and Capped ZrN Films Grown by Plasma Enhanced ALD: Effect of Ambient Oxidation. *Appl. Surf. Sci.* **2018**, *435*, 367–376. https://doi.org/10.1016/j.apsusc.2017.11.104.

(15) Fang, X.; Wu, S.; Wu, Y.; Yang, W.; Li, Y.; He, J.; Hong, P.; Nie, M.; Xie, C.; Wu, Z.; others. High-Efficiency Adsorption of Norfloxacin Using Octahedral UIO-66-NH2 Nanomaterials: Dynamics, Thermodynamics, and Mechanisms. *Appl. Surf. Sci.* **2020**, *518*, 146226.

(16) Chen, Q.; He, Q.; Lv, M.; Xu, Y.; Yang, H.; Liu, X.; Wei, F. Selective Adsorption of Cationic Dyes by UiO-66-NH2. *Appl. Surf. Sci.* **2015**, *327*, 77–85.

(17) Jaeger, D.; Patscheider, J. A Complete and Self-Consistent Evaluation of XPS Spectra of TiN. *J. Electron Spectrosc. Relat. Phenom.* **2012**, *185* (11), 523–534.

(18) Carrasco, E.; Herrero, V. J.; Tanarro, I. Time-Resolved Diagnostics and Kinetic Modelling of the Ignition Transient of a H_2 + 10% N_2 Square Wave Modulated Hollow Cathode Discharge. *J. Phys. Appl. Phys.* **2012**, *45* (30), 305201. https://doi.org/10.1088/0022-3727/45/30/305201.

(19) Boris, D. R.; Wheeler, V. D.; Nepal, N.; Qadri, S. B.; Walton, S. G.; Eddy, C. (Chip) R. The Role of Plasma in Plasma-Enhanced Atomic Layer Deposition of Crystalline Films. *J. Vac. Sci. Technol. A* **2020**, *38* (4), 040801. https://doi.org/10.1116/6.0000145.

(20) Vallée, C.; Bonvalot, M.; Belahcen, S.; Yeghoyan, T.; Jaffal, M.; Vallat, R.; Chaker, A.; Lefèvre, G.; David, S.; Bsiesy, A.; Possémé, N.; Gassilloud, R.; Granier, A. Plasma Deposition—Impact of Ions in Plasma Enhanced Chemical Vapor Deposition, Plasma Enhanced Atomic Layer Deposition, and Applications to Area

Selective Deposition. *J. Vac. Sci. Technol. Vac. Surf. Films* **2020**, *38* (3), 033007. https://doi.org/10.1116/1.5140841.

(21) Profijt, H.; Potts, S.; Van de Sanden, M.; Kessels, W. Plasma-Assisted Atomic Layer Deposition: Basics, Opportunities, and Challenges. *J. Vac. Sci. Technol. A* **2011**, *29* (5).

(22) Faraz, T.; Arts, K.; Karwal, S.; Knoops, H. C. M.; Kessels, W. M. M. Energetic Ions during Plasma-Enhanced Atomic Layer Deposition and Their Role in Tailoring Material Properties. *Plasma Sources Sci. Technol.* **2019**, *28* (2), 024002. https://doi.org/10.1088/1361-6595/aaf2c7.

(23) Samal, N.; Du, H.; Luberoff, R.; Chetry, K.; Bubber, R.; Hayes, A.; Devasahayam, A. Low-Temperature (≤200 ° C) Plasma Enhanced Atomic Layer Deposition of Dense Titanium Nitride Thin Films. *J. Vac. Sci. Technol. Vac. Surf. Films* **2013**, *31* (1), 01A137. https://doi.org/10.1116/1.4769204.

(24) Zhang, X.-Y.; Peng, D.-C.; Yan, J.-H.; Zhang, Z.-X.; Ruan, Y.-J.; Zuo, J.; Xie, A.; Wu, W.-Y.; Wuu, D.-S.; Huang, C.-J.; Lai, F.-M.; Lien, S.-Y.; Zhu, W.-Z. Plasma Power Effect on Crystallinity and Density of AlN Films Deposited by Plasma Enhanced Atomic Layer Deposition. *J. Mater. Res. Technol.* **2023**, *27*, 4213–4223. https://doi.org/10.1016/j.jmrt.2023.10.302.

(25) Yoon, H. J.; Jeon, H. Impact of Plasma Power on Plasma Enhanced Atomic Layer Deposited TiO2 as a Spacer. *Thin Solid Films* **2024**, *807*, 140551. https://doi.org/10.1016/j.tsf.2024.140551.

(26) Yoon, M. Y.; Jeong, J.-R.; Lee, H.-C.; Kim, J.-H. Plasma Low-Energy Ion Flux Induced Vertical Graphene Synthesis. *Appl. Surf. Sci.* **2023**, *636*, 157814. https://doi.org/10.1016/j.apsusc.2023.157814.

(27) Kusano, E.; Fukushima, K.; Saitoh, T.; Saiki, S.; Kikuchi, N.; Nanto, H.; Kinbara, A. Effects of Ar Pressure on Ion Flux Energy Distribution and Ion Fraction in r.f.-Plasma-Assisted Magnetron Sputtering. *Surf. Coat. Technol.* **1999**, *120–121*, 189–193. https://doi.org/10.1016/S0257-8972(99)00453-3.

(28) Rehman, A.; Van De Kruijs, R. W. E.; Van Den Beld, W. T. E.; Sturm, J. M.; Ackermann, M. Chemical Interaction of Hydrogen Radicals (H*) with Transition Metal Nitrides. *J. Phys. Chem. C* **2023**, *127* (36), 17770–17780. https://doi.org/10.1021/acs.jpcc.3c04490.

(29) Elam, J. W.; Schuisky, M.; Ferguson, J. D.; George, S. M. Surface Chemistry and Film Growth during TiN Atomic Layer Deposition Using TDMAT and NH3. *Thin*

Solid Films **2003**, *436* (2), 145–156. https://doi.org/10.1016/S0040-6090(03)00533-9.

7 Conclusion and Future work

7.1 Conclusion

The main conclusions drawn from Chapters 3 - 6 provide a deeper understanding of plasma behaviour in plasma-enhanced atomic layer deposition (PE-ALD) and demonstrate the benefits of combining pre-ALD plasma characterisation with in-situ plasma diagnostics. Together, these studies address the challenge of plasma control within the ALD environment which ultimately determines the process success and key film properties such as growth per cycle, composition, and chemical bonding. This work establishes new insights into how plasma conditions evolve both outside and inside an ALD environment, highlights the importance of monitoring plasma stability during processing, and introduces a novel quantitative diagnostic approach for hydrogen containing plasmas.

Chapter 3 demonstrated that a pre-ALD plasma parametric study via optical emission spectroscopy (OES) can guide process selection for optimised CoN PE-ALD. By understanding the PE-ALD mechanisms and maximising the identified key spectral emission line, NH, improved ligand removal and cobalt incorporation was achieved. Additionally, the emission line ratio of NH:Hα was identified to correlate strongly with growth mechanisms such as film thickness and cobalt incorporation. Despite limitations of this method, namely a lack of quantitative plasma insights, it provided a meaningful insight and showed pre-ALD characterisation can guide optimisation of the PE-ALD process.

Chapter 4 established a quantitative parametric characterisation of H_2/Ar plasma using a combination of invasive and non-invasive plasma diagnostic techniques, including

energy resolved actinometry (ERA) adapted for hydrogen containing plasma. This approach enabled determination of key plasma parameters, including the degree of H_2 dissociation, mean electron energy, and ion flux at the substrate level. The study provided a quantitative baseline of the plasma response across a broad operational window. Although this chapter focused solely on plasma behaviour rather than PE-ALD processing, the dataset offers a foundational reference for interpreting plasma response in later work. An in-depth review was performed, and the results were validated against established published work.

Chapter 5 built on the understanding developed in the previous chapter to investigate how the ALD environment influences plasma behaviour during $Cu(acac)_2$ + H_2/Ar PE-ALD, along with the film properties response to changes in ICP power, chamber pressure and feed gas flow. Using a combination of OES and ERA, quantitative and measurable shifts in the plasma response were identified and analysed. The corresponding films were examined but no correlation was found between plasma features, such as the degree of H_2 dissociation, mean electron energy, or key emission line intensities and the resulting film properties. Unlike Chapter 3, where the pre-ALD characterisation guided process condition selection, the work in this chapter consisted of a parametric study in which single-parameter variations of a reference process were investigated for a range of values. As a result, diagnosed plasma features overlapped with differing film properties, preventing clear correlation. This chapter therefore highlights that due to the complexity of plasma surface interactions, additional diagnostic tools or more advanced modelling approaches are required to enable a predictive film property diagnostic method. While only single feature correlations were explored due to the limited dataset, the study provided valuable insight into how the ALD environment influences plasma behaviour and demonstrated the successful implementation of ERA within a PE-ALD process.

Finally, Chapter 6 served as a case study demonstrating potential faults in the PE-ALD process. In this chapter TDMAZr + $H_2/N_2/Ar$ PE-ALD was investigated without a pre-ALD plasma study. In-situ OES monitoring detected significant variations in the plasma during processing, while system logging showed no indication of any issue. The instabilities within the plasma resulted in non-reproducible film growth across multiple reference processes. Additionally, the growth response to the investigated parameters deviated from trends previously established from both work within this thesis and published work. The results demonstrated that plasma monitoring is essential for diagnosing processing faults linked to the plasma behaviour. It also reinforces the use case for a pre-ALD parametric study to identify stable processing conditions for reproducible PE-ALD processing.

Throughout the plasma diagnostics studies in Chapters 4 and 5, a novel modification to ERA was implemented. This method enabled quantitative interpretation of H_2/Ar plasma behaviour, providing access to key parameters such as the degree of H_2 dissociation and the mean electron energy. The results were evaluated through comprehensive comparison with established literature on similar plasma compositions and reactor configurations. Overall, the identified trends were consistent with published data, validating the applicability of the modified ERA approach for quantitative analysis of H_2/Ar plasmas before and in PE-ALD processing.

Overall, this thesis demonstrates that robust PE-ALD processing cannot rely solely on equipment setpoints and ex-situ characterisation but must incorporate an understanding of the plasma as an evolving physical system. It shows that plasma behaviour can change substantially under ALD-relevant conditions and that undetected instabilities can result in irreproducible film growth. By combining pre-ALD characterisation, in-situ

diagnostics and quantitative analysis, this work provides a practical framework for developing more controllable and reproducible PE-ALD processes.

7.2 Future Work

Based on the results and conclusions of this work, there are several interesting areas for potential future research that could further improve the understanding and control of plasma behaviour during PE-ALD. The first of these opportunities lies in the continued development of the ERA method. In this thesis, ERA calculations were performed through a sequence of manual steps, limiting the analysis to time averaged measurements. Automating this calculation procedure would enable a higher throughput of processed data and significantly increase the quantity of information extracted from each experiment. Building on this, an automated workflow could support real time ERA diagnostics during PE-ALD. A live feed of quantitative plasma response data could open the possibility of implementing a closed-loop control system in which deviations from the expected plasma behaviour are identified and corrected during processing. The current work utilised Ocean View and BOLSIG+ software to obtain OES measurements and electron-impact rate coefficients, respectively. Existing Python packages such as Seabreeze already allow automated OES data acquisition. BOLSIG- can be operated through a terminal with input files rather than graphical interfaces, which could be generated automatically to provide the required rate co-efficient. Together, this could provide a pathway toward an integrated real-time plasma monitoring and feature extraction system. The development of such a control system would represent a significant advancement in plasma-driven ALD process stability. A natural extension of this work would be to adapt the ERA methodology to a wider range of gas compositions. While this thesis focused on H_2/Ar plasmas, and previous studies have demonstrated its applicability to O_2/Ar mixtures, extending ERA to N_2 containing and mixed-gas discharges would broaden its relevance to a wider set of PE-ALD processes.

Another promising research direction involves expanding the pre-ALD plasma characterisation approach through additional diagnostic techniques combined with a modelling framework. While the present work used OES, ERA, and ion flux measurements to characterise plasma behaviour, integrating further diagnostics such as mass spectrometry could enable the construction of multi-parameter models capable of forecasting plasma response under varied conditions. Such models could utilise the preservation of plasma trends observed in this work when adapted into the ALD environment. This could provide a deeper insight into the plasma–surface interactions governing PE-ALD. Additionally, other non-invasive in-situ diagnostics methods could be incorporated into the model during PE-ALD processing, such as ellipsometry. A predictive model of this nature could guide process optimisation and reduce the reliance on empirical trial-and-error approaches. Together, these potential research directions offer a pathway toward a more data-driven, controllable and reproducible PE-ALD process.